Technical Physics Letters, Vol. 27, No. 12, 2001, pp. 1003–1005. Translated from Pis'ma v Zhurnal Tekhnicheskoĭ Fiziki, Vol. 27, No. 23, 2001, pp. 49–52.

Crystallization and Physical Properties of $SbTiTaO_6$ Single Crystals

V. I. Popolitov

Shubnikov Institute of Crystallography, Russian Academy of Sciences, Moscow, 117333 Russia

Received June 26, 2001

Abstract—Optimum physicochemical conditions for a hydrothermal crystallization of antimony titanium tantalate $SbTiTaO_6$ (STT) at 190–225°C in the $SbTiTaO_6$–H_2SO_4–HCl–H_2O_2–H_2O system with various concentrations of acids and hydrogen peroxide. The dielectric and pyroelectric properties of synthesized STT single crystals were studied. © *2001 MAIK "Nauka/Interperiodica".*

The possibility of obtaining ferroelectric antimony titanium tantalate $SbTiTaO_6$ (STT) single crystals by hydrothermal synthesis was demonstrated in [1]. A disadvantage of the known procedure is a high temperature of the process, low yield, and insufficient purity of STT single crystals. Below, we report for the first time experimental data on the hydrothermal growth of STT single crystals from $SbTiTaO_6$ powder in the $SbTiTaO_6$–H_2SO_4–HCl–H_2O_2–H_2O system.[1]

The crystallization process was conducted using various concentrations of acids and hydrogen peroxide in the system ($C_{H_2SO_4}$ = 5–8 wt %; C_{HCl} = 6–9 wt %; $C_{H_2O_2}$ = 5–7 wt %), at the volume ratio of these components 2 : 1 : 0.6, respectively. The experiments were performed in a temperature interval from 190 to 225°C at a temperature gradient of 0.5–0.8 K/cm using an optical quartz reactor with a volume of 1 dm^3; the coefficient of filling with the liquid phase was 0.4–0.5. Recrystallization of the initial $SbTiTaO_6$ powder in acid solutions in a stationary regime proceeds by the following scheme: (i) congruent dissolution of the initial material; (ii) convective mass transport driven by the temperature gradient toward the supersaturation zone, and (iii) growth of STT single crystals. During the experiments, it was established that optimum technological parameters, ensuring the crystallization of STT with a yield of 70–80 wt % (of the initially charged powder), are as follows: $C_{H_2SO_4}$ = 8 wt %; C_{HCl} = 9 wt %; $C_{H_2O_2}$ = 8 wt %; process temperature, 225°C; temperature gradient, 0.8 K/cm.

[1] $SbTiTaO_6$ powder was synthesized by method of precipitation from aqueous methanol solutions of components.

The composition of as-grown STT single crystals was studied by X-ray spectroscopy on a Cameca electron-probe microanalyzer (France). The percentage content of antimony, titanium, and tantalum in the sample well is in good agreement with the values calculated by the formula $SbTiTaO_6$. The STT single crystal structure represents a combination of monohedrons (001) and $(00\bar{1})$ with rhombic prism faces (011) and rhombic pyramid faces (111). The dimensions of single crystals were on the order of 4 × 1–4 × 2.3 mm. The samples appeared as transparent crystals of a light yellow color depending on the partial oxygen pressure ($H_2O_2 \rightleftharpoons H_2O + O$), the reactor cleanness, and the crystallization medium purity. X-ray diffraction measurements using the Laue technique showed that STT single crystals possess an orthorhombic structure with the lattice parameters $a = 7.6 \pm 0.003$ Å, $b = 5.11 \pm 0.003$ Å, $c = 10.89 \pm 0.004$ Å. The results of indexing of the X-ray diffraction patterns from powdered STT single crystals measured using CuK_α radiation are presented in the table.

The dielectric properties of STT singe crystals were measured at a frequency of 1 kHz using an E8-2 bridge. The samples were prepared in the form of ground monohedral plates with a thickness of 300 μm cut in the direction of the [001] polar axis. Electrodes were formed on the opposite faces by fusing a silver paste at a temperature of 550–600°C. The measurements were performed as described elsewhere [2]. The temperature dependences of the permittivity (ε) and loss tangent ($\tan\delta$) of STT single crystals measured in the polar axis direction exhibit clearly pronounced maxima at 290 ± 5°C, which correspond to a transition from ferro-

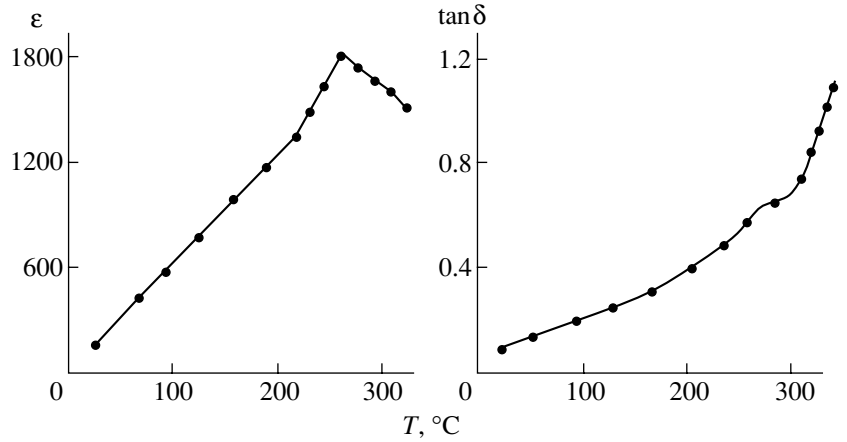

Fig. 1. Temperature dependences of the permittivity (ε) and loss tangent ($\tan\delta$) of $SbTiTaO_6$ single crystals.

to antiferroelectric state (Fig. 1). The spontaneous polarization of STT single crystals estimated from dielectric hysteresis loops measured at 20°C was 16 μC/cm^2.

The data of the differential thermal analysis of STT single crystals in the temperature interval from 25 to 750°C showed an endothermal effect at 270–290°C, which was not accompanied by the sample weight loss. Taking into account that $SbTiTaO_6$ crystals did not melt in the temperature rage studied, it was concluded that the aforementioned endothermicity corresponds to the phase transition in STT single crystals revealed by the $\varepsilon(T)$ and $\tan\delta(T)$ measurements. We have also studied the laser second harmonic generation in STT single crystals in the above temperature interval. The $J_2W(T)$ curve also exhibited a distinct maximum in the region of 290°C. A sharp drop in the J_2W signal intensity above 290°C is indicative of a transition into the antiferroelectric phase.

Prior to pyroelectric measurements, the STT single crystals were polarized. For this purpose, the samples were placed into a vacuum thermostat and heated up to a phase transition temperature determined by a maximum in the $\varepsilon(T)$ anomaly. Then, an electric field with a strength of 25–30 kV/cm was applied. The samples were exposed in this field for 3 h at the indicated temperature and slowly cooled down to room temperature, after which the field was switched off. The pyroelectric measurements were performed by a dynamic technique at a thermal flux modulation frequency of 1 kHz. The pyroelectric effect was observed only in the STT single crystals cut in the direction perpendicular to the (001) axis. As can be seen from Fig. 2, a maximum pyroelectric coefficient γ is observed at 290°C. The STT single crystals possess a sufficiently high pyroelectric coeffi-

Parameters of the X-ray diffractogram of powdered $SbTiTaO_6$ single crystals

hkl	d_1, Å	d_2, Å	J/J_1, %	*hkl*	d_1, Å	d_2, Å	J/J_1, %
011	4.59	4.49	6	206	1.61	1.59	19
201	3.51	3.48	21	125	1.59	1.44	24
210	2.98	2.90	100	026	1.41	1.36	16
113	2.71	2.68	31	316	1.39	1.31	9
014	2.39	2.31	14	325	1.36	1.28	14
302	2.30	2.24	11	028	1.18	1.11	6
400	1.89	1.78	9	417	1.12	1.04	8
320	1.78	1.7	26	605	1.06	0.98	5
412	1.69	1.58	19	232	1.47	1.4	13
130	1.61	1.56	8	143	1.16	1.10	6

Note: Interplanar spacings d_1 and d_2 refer to the measured and calculated data, respectively.

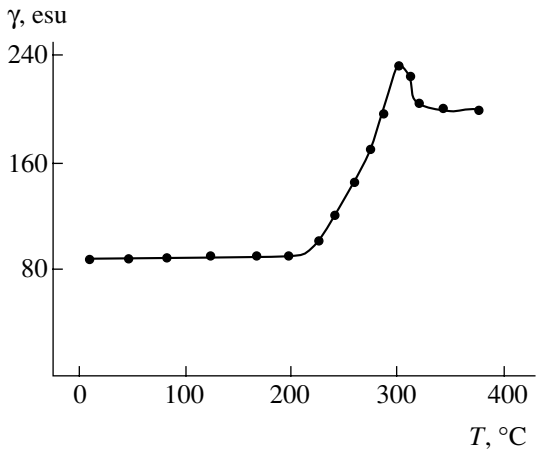

Fig. 2. Temperature dependence of the pyroelectric coefficient (γ) of $SbTiTaO_6$ single crystals.

cient (γ = 85 esu) at room temperature, which remains virtually constant as the temperature increases to about 290°C.

Conclusion. Possessing a low permittivity (ε = 75 at 20°C) and a relatively high pyroelectric coefficient weakly dependent on the temperature, the single crystals of antimony titanium tantalate $SbTiTaO_6$ are a promising material for the working elements of the pyroelectric transducers capable of operating in a temperature range from 20 to 290°C.

REFERENCES

1. V. I. Popolitov, Zh. Prikl. Khim. **65** (11), 2441 (1992).
2. V. I. Popolitov, Pis'ma Zh. Tekh. Fiz. **20** (1), 62 (1994).

Translated by P. Pozdeev

Technical Physics Letters, Vol. 27, No. 12, 2001, pp. 1006–1007. Translated from Pis'ma v Zhurnal Tekhnicheskoĭ Fiziki, Vol. 27, No. 23, 2001, pp. 53–55.

Synthesis and Ferroelectric Properties of $K_2SbTa_5O_{15}$ Single Crystals

V. I. Popolitov

Shubnikov Institute of Crystallography, Russian Academy of Sciences, Moscow, 117333 Russia

Received June 26, 2001

Abstract—The conditions of a hydrothermal synthesis of monodomain ferroelectric potassium antimony tantalate $K_2SbTa_5O_{15}$ (KST) single crystals in the Sb_2O_3–Ta_2O_5–KF–H_2O_2–H_2O system were studied. The structural, dielectric, and pyroelectric properties of the synthesized KST single crystals were determined. The results show KST to be a promising material for new technologies. *© 2001 MAIK "Nauka/Interperiodica".*

The discovery of ferroelectric properties in potassium antimony niobate $K_2SbNb_5O_{15}$ [1] inspired the attempt to crystallize an analogous isostructural compound—potassium antimony tantalate $K_2SbTa_5O_{15}$ (KST).

The KST single crystals were obtained by hydrothermal synthesis in the Sb_2O_3–Ta_2O_5–KF–H_2O_2–H_2O system, where crystallization medium was represented by a mixed aqueous solution of potassium fluoride (KF) and hydrogen peroxide (H_2O_2) with the concentrations of 56–62 and 4–6 wt %, respectively. The process of the KST single crystal synthesis was performed in a periodic reactor [2] at a temperature of 427°C, a liquid phase pressure of 10^9 Pa, and a temperature gradient of 0.3–0.7 K/cm. The crystallization proceeded by the following physicochemical scheme: (i) dissolution of the initial oxides (Sb_2O_3 and Ta_2O_5) in aqueous KF and H_2O_2 solutions; (ii) transport of the dissolved components to the growth zone; and (iii) synthesis of KST single crystals.

According to the results of elemental chemical analysis and spectroscopic measurements, the composition of the as-grown KST single crystals corresponded to the empirical formula $K_2SbTa_5O_{15}$. It was found that the single crystal yield (g/day) and size depend on several parameters including the concentration of aqueous KF and H_2O_2 solutions, the volume ratio of components, and the temperature gradient. The optimum yield of KST single crystals was observed at a temperature of 427°C, a temperature gradient of 0.7 K/cm, a KF con-

Parameters of the X-ray diffractogram of powdered $K_2SbTa_5O_{15}$ single crystals

hKil	d_1, Å	d_2, Å	J/J_{01}	*hKil*	d_1, Å	d_2, Å	J/J_{01}
$10\bar{1}1$	7.2	7.185	4	$04\bar{4}2$	2.12	2.1	3
$11\bar{2}0$	5.3	5.25	5	$20\bar{2}5$	2.1	2.08	3
$01\bar{1}2$	4.935	4.924	7	$32\bar{5}1$	2.07	2.04	3
$02\bar{2}1$	4.23	4.21	6	$41\bar{5}0$	2.03	2.0	2
0003	3.92	3.87	100	0006	1.934	1.931	50
$11\bar{2}3$	3.12	3.11	31	$11\bar{2}6$	1.812	1.81	9
3030	3.02	2.98	32	$41\bar{5}3$	1.81	1.8	11
$10\bar{1}4$	2.7	2.67	4	$33\bar{6}0$	1.76	1.75	12
3142	2.4	2.36	4	3036	1.64	1.635	19
$30\bar{3}3$	2.36	2.3	4	$04\bar{4}5$	1.62	1.59	7
$22\bar{4}3$	2.14	2.1	9	$60\bar{6}0$	1.52	1.51	5

Note: Subscripts "1" and "2" refer to the measured and calculated values, respectively.

1063-7850/01/2712-1006$21.00 © 2001 MAIK "Nauka/Interperiodica"

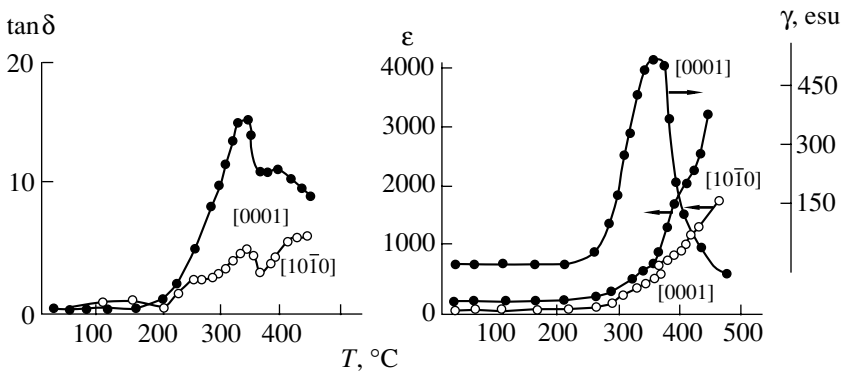

Temperature dependences of the permittivity (ε), loss tangent (tanδ), and pyroelectric coefficient (γ) of $K_2SbTa_5O_{15}$ single crystals.

centration of 56 wt %, an H_2O_2 concentration of 6 wt %, and a KF/H_2O_2 volume ratio of 4 : 1.

The KST single crystal structure was studied by X-ray diffraction (CuK_α radiation) using the Laue, Weissenberg, and powder techniques. It was established that the grown single crystals belong to a bitrigonal-pyramidal class with the lattice parameters a = 10.653 ± 0.04 Å, c = 11.597 ± 0.005 Å (hexagonal setting). Based on an analysis of the system of extinctions in the Weissenberg patterns and the symmetry of Laue diffractograms, with an allowance of the results of pyroelectric measurements, the KST single crystals were assigned the space group $R3m$. The as-grown single crystals had a size of 3–4 mm^3 and were faceted according to the simple forms: {0001}, {000$\bar{1}$}, {11$\bar{2}$0}. The results of indexing of the X-ray diffraction patterns from powdered KST single crystals measured using CuK_α radiation are presented in the table.

The dielectric properties of KST singe crystals were studied using an E8-2 bridge operated at a frequency of 1 kHz. The pyroelectric measurements were performed by a dynamic technique at a thermal flux modulation frequency of 1 kHz. The single crystal samples for these measurements were prepared in the form of ground plates with a thickness of 300 μm cut in the directions [0001], [10$\bar{1}$0], and [01$\bar{1}$0]. Electrodes were formed on the plate surfaces by fusing a silver paste at a temperature of 500–600°C. The KST single crystals were monodomain and required no additional polarization prior to the pyroelectric measurements.

The pyroelectric effect was observed only in the KST single crystals cut in the direction perpendicular to the [0001] axis (see figure). As can be seen from the pyroelectric curve presented in the figure, a maximum in the pyroelectric coefficient (γ) is observed at 340°C. The figure also shows the temperature dependences of the permittivity (ε) and loss tangent (tanδ) of the same samples measured in two directions, which reveal a clearly pronounced peak due to a phase transition at 340°C. A combination of the dielectric and pyroelectric data indicates that the synthesized KST single crystals represent a ferroelectric compound with a Curie point at 340°C.

The proposed method offers an effective means of the KST synthesis, ensuring the obtaining of monodomain ferroelectric single crystals of $K_2SbTa_5O_{15}$ with a high yield and good quality. The latter circumstance is important for the application of KST single crystals in piezoelectric sensors and pyroelectric transducers.

Conclusion. New monodomain ferroelectric potassium antimony tantalate $K_2SbTa_5O_{15}$ (KST) single crystals were synthesized by hydrothermal method in the Sb_2O_3–Ta_2O_5–KF–H_2O_2–H_2O system. The structural, dielectric, and pyroelectric properties of the synthesized samples were studied, showing these single crystals to be a promising material for new technologies.

REFERENCES

1. V. I. Popolitov, A. N. Lobachev, L. I. Ivanova, *et al.*, Kristallografiya **20** (4), 783 (1975).
2. V. I. Popolitov and B. N. Litvin, in *Growing Single Crystals under Hydrothermal Conditions* (Nauka, Moscow, 1986), p. 31.

Translated by P. Pozdeev

Technical Physics Letters, Vol. 27, No. 12, 2001, pp. 1008–1009. Translated from Pis'ma v Zhurnal Tekhnicheskoĭ Fiziki, Vol. 27, No. 23, 2001, pp. 56–59.

On the Properties of a Radiation-Induced Defect Responsible for the 1.0-eV IR Absorption Band in Gallium Arsenide

Z. V. Dzhibuti and N. D. Dolidze

Tbilisi State University, Tbilisi, Georgia

Received March 29, 2001

Abstract—The IR absorption spectra were measured at 77 K for Te-doped *n*-GaAs samples irradiated by electrons with an energy of $E = 3$ MeV. It was found that the samples exhibit two absorption bands in the IR range, corresponding to 1.0 and 0.8 eV. © *2001 MAIK "Nauka/Interperiodica".*

As is known [1–5], irradiation with accelerated electrons (2–6 MeV) at 300 K leads to the formation of defects in gallium arsenide, which are manifested by a broad absorption band in the region of 0.96–1 eV in the IR spectrum of irradiated samples. Our study of the samples of *n*- and *p*-GaAs irradiated at 77 K showed that exposure to a total fluence of $\Phi = 1.5 \times 10^{18}$ cm^{-2} (as well as the irradiation at $T = 300$ K) gives rise to the formation of defects responsible for the absorption band peaked at 1.0 eV [6–8].

An increase in the total fluence of fast electrons for the GaAs samples irradiated at 77 K leads to the appearance and rapid growth in intensity of an additional absorption signal with a maximum at 0.80–0.82 eV. When the electron irradiation dose amounts to 3×10^{18} cm^{-2}, the absorption signal in this region becomes so intense that it overlaps with the 1.0-eV band to form the new broad band with a maximum in the region of 0.8 eV [6, 7]. The IR spectra measured after repeated isochronous anneals showed that the intensity of this band decreases with increasing temperature of the thermal treatment, while the peak position shifts toward higher energies (from 0.8 to 1.0 eV after the anneal at $T = 425$ K [6]).

Brudnyĭ *et al.* [3] pointed out that, as the temperature of spectral measurements was gradually decreased down to 6 K, the 1.0-eV absorption band in the IR spectra of GaAs irradiated at 300 K exhibited splitting into two bands peaked at $h\nu = 0.82$ and 0.96 eV. Both bands increased in intensity proportionally to the irradiation dose and also simultaneously decreased in the course of isochronous anneals. It was suggested that both absorption bands belong to the same radiation defect. Thus, we may believe that the 1.0-eV absorption peak and the new band [6] with a maximum at 0.80–0.82 eV, obtained upon the electron irradiation at 77 K, also belong to the same defect.

If this assumption is valid, the GaAs samples irradiated at room temperature must exhibit the IR absorption band at 0.80–0.82 eV (together with the 1.0-eV band related to the intracenter transitions between levels) under certain conditions at 77 K, although no one previous experiment revealed this band. However, this experimental possibility is offered by the method of measuring the IR absorption spectra of the samples continuously illuminated with white light. In this case, the light-induced generation of the nonequilibrium charge carriers leads to a shift of the Fermi level [10] and makes it possible that some electron states above the Fermi level would become free.

The experiments were performed on *n*-GaAs doped with tellurium to $n = 10^{16}$ cm^{-3}. The samples were irradiated at $T = 300$ K with accelerated electrons ($E = 3$ MeV) to a total fluence of $\Phi = 3 \times 10^{18}$ cm^{-2}. The IR absorption spectra were measured at 77 K, either with or without additional illumination with white light from an incandescent lamp. The spectra of unirradiated (control) samples were measured under identical conditions and a change in the absorption coefficient was determined as $\Delta\alpha = \alpha_{rad} - \alpha_{contr}$, where α_{rad} and α_{contr} are the absorption coefficients of irradiated and control samples.

The spectral dependences of the $\Delta\alpha$ value for the GaAs samples measured in the dark (curve *1*) and under continuous illumination with white light (curve *2*) are presented in the figure. As can be seen from these data, the spectrum measured with the additional illumination exhibits increased absorption manifested by a bending point about 0.80 eV. This feature indicates that an additional absorption band appeared in this region, while the 1.0-eV band intensity remained unchanged. The spectrum measured upon switching off the additional illumination coincided with curve *1*. The isochronous anneals were accompanied by simultaneous decrease in the intensity of both bends, which was analogous to the behavior observed in [3].

Thus, the results of our experiments confirmed the existence of an absorption band at 0.80 eV in the GaAs samples irradiated with electrons at 300 K. This fact indicates that a defect responsible for the IR absorption band at 1.0 eV (probably, a mixed divacancy of the $V_{Ga} + V_{As}$ type [9]) also exhibits, irrespective of the irra-

1063-7850/01/2712-1008$21.00

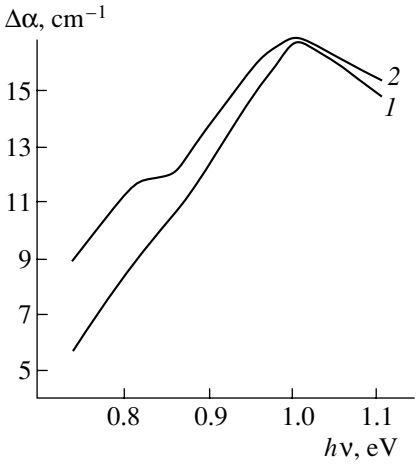

Spectral dependence of the differential absorption coefficient of GaAs irradiated at $T = 300$ K with accelerated electrons and measured at 77 K (*1*) in the dark and (*2*) under additional constant illumination with white light.

diation temperature, a second absorption band with a maximum at about 0.80 eV.

REFERENCES

1. E. Yu. Brailovskiĭ, V. N. Brudnyĭ, M. A. Krivov, and V. B. Red'ko, Fiz. Tekh. Poluprovodn. (Leningrad) **6** (10), 2075 (1972) [Sov. Phys. Semicond. **6**, 1768 (1972)].
2. V. N. Brudnyĭ, E. Yu. Brailovskiĭ, M. A. Krivov, and V. B. Red'ko, Izv. Vyssh. Uchebn. Zaved., Fiz., No. 10, 118 (1974).
3. V. N. Brudnyĭ, A. A. Groza, and M. A. Krivov, Izv. Vyssh. Uchebn. Zaved., Fiz. **4**, 101 (1982).
4. K. P. Aref'ev, V. N. Brudnyĭ, D. L. Budnitskiĭ, *et al.*, Fiz. Tekh. Poluprovodn. (Leningrad) **13** (6), 1142 (1979) [Sov. Phys. Semicond. **13**, 669 (1979)].
5. N. Kh. Pambukhchyan, Candidate's Dissertation (Kiev, Yerevan, 1983).
6. Z. V. Dzhibuti, N. D. Dolidze, G. L. Ofengeĭm, *et al.*, Fiz. Tekh. Poluprovodn. (Leningrad) **21** (5), 930 (1987) [Sov. Phys. Semicond. **21**, 567 (1987)].
7. Z. V. Dzhibuti, Candidate's Dissertation (Tbilisi, 1989).
8. Z. V. Dzhibuti and N. D. Dolidze, Pis'ma Zh. Tekh. Fiz. **17** (5), 41 (1991) [Sov. Tech. Phys. Lett. **17**, 172 (1991)].
9. Z. V. Dzhibuti and N. D. Dolidze, Pis'ma Zh. Tekh. Fiz. **26** (17), 76 (2000) [Tech. Phys. Lett. **26**, 789 (2000)].
10. S. M. Ryvkin, *Photoelectric Effects in Semiconductors* (Fizmatgiz, Leningrad, 1963; Consultants Bureau, New York, 1964).

Translated by P. Pozdeev

Technical Physics Letters, Vol. 27, No. 12, 2001, pp. 1010–1012. Translated from Pis'ma v Zhurnal Tekhnicheskoĭ Fiziki, Vol. 27, No. 23, 2001, pp. 60–66.

Initial Stages of the GaN Growth on Oxidized Silicon

V. N. Bessolov[a], Yu. V. Zhilyaev[a], E. V. Konenkova[a], S. A. Kukushkin[b], A. V. Luk'yanov[c], S. D. Raevskiĭ[a], and V. A. Fedirko[d]

[a] *Ioffe Physicotechnical Institute, Russian Academy of Sciences, St. Petersburg, 194021 Russia*
[b] *Institute of Machine Science, Russian Academy of Sciences, St. Petersburg, Russia*
[c] *Foundation for Support of Science and Education, St. Petersburg, Russia*
[d] *Moscow State Technological University "Stankin," Moscow, Russia*

Received July 25, 2001

Abstract—Initial stages of the GaN layer growth during an HVPE process at 520°C on an oxidized silicon substrate were studied by atomic force microscopy. It was established that (i) the growth of GaN islands is controlled by the surface diffusion and (ii) the nucleus size distribution on the surface significantly changes when the growth time increases from 10 to 200 min: during this period of time, the average nucleus size increases from 15 to 400 nm and their size scatter becomes 20 times as large as the initial size distribution width. The experimentally determined growth rate of the GaN nuclei and the nucleus size distribution are in good agreement with theoretical calculations. *© 2001 MAIK "Nauka/Interperiodica".*

The heteroepitaxial growth of gallium nitride layers during vapor phase epitaxy (HVPE) has been studied for more than three decades [1], but it was not until very recently that the interest in HVPE GaN layers has greatly increased due to achievements in obtaining high-quality layers by method of metalorganic chemical vapor deposition (MOCVD) [2]. This is related to the fact that HVPE is virtually the only process providing for the deposition of sufficiently thick layers of Group III nitride semiconductors [3] and low-temperature buffer layers (e.g., of GaN) [4].

The process of layer nucleation during the low-temperature epitaxy is of considerable importance, first, as a means of increasing the quality of heteroepitaxial structures already in the nucleation stage [5] and, second, as a method of obtaining nanosize GaN clusters on SiO_2 substrates—the objects of interest in polycrystal photonics—a new direction in the physics of semiconductors [6].

There were attempts at growing the layers of Group III nitride semiconductors on Si substrates by HVPE at high temperatures: 1150°C [7] and 800°C [8]. The results showed that the grows of single-crystal Group III nitride semiconductors on silicon at $T > 800$°C is hindered by the Si–NH_3 interaction leading to the formation of an amorphous Si_3N_4 layer [9]. A decrease in the growth temperature must reduce the rate of the substrate interaction with ammonia and hydrogen chloride.

Below, we report on the results of investigation of the nucleation mechanism and the kinetics of a GaN(0001) layer growth by HVPE on an oxidized Si(111) substrate at low ($T = 520$°C) temperatures. The experimental results are compared to predictions of the corresponding theoretical model [10].

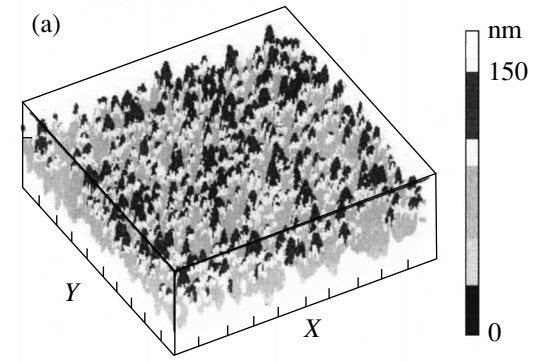

scale: $Y = 1000$ nm, $X = 1000$ nm, $Z = 100$ nm

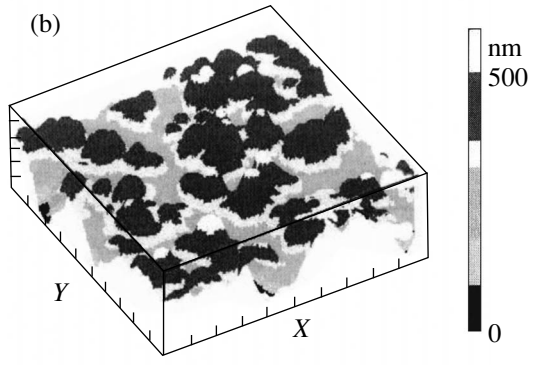

scale: $Y = 1000$ nm, $X = 1000$ nm, $Z = 100$ nm

Fig. 1. AFM profiles of GaN/SiO_2 surfaces for various times of heteroepitaxial growth: (a) 100 min; (b) 200 min.

1063-7850/01/2712-1010$21.00

The heteroepitaxial growth of GaN was effected on a preliminarily oxidized silicon wafers with a diameter of 50 mm rotating in a flow of hydrogen at a rate of 1 Hz. The ratio of the component flow rates H_2/NH_3 was 2 : 1, and the epitaxy proceeded at a temperature of T = 520°C. The time of a substrate exposure in the growth zone was varied from 10 to 25, 50, 100, or 200 min. After the heteroepitaxy stage, the pattern of the initial GaN growth on the samples was studied by atomic force microscopy (AFM) at room temperature and atmospheric pressure. The AFM investigations were performed on an NT–MDT instrument using standard silicon nitride cantilevers.

A comparative analysis of the AFM images showed that, under the HVPE conditions studied, GaN is nucleated according to the island mechanism (Fig. 1). The nuclei had the shape of disks. We believe that the island height h at the instant of nucleation is comparable with the disk base radius R. The number of nuclei per unit surface area decreases with time (Fig. 2). The distribution of the GaN nucleus size on the substrate surface varies as well. As the growth time increases from 10 to 200 min, the average height h grows from 15 to 400 nm (Fig. 3) and the nucleus size scatter Δh (determined as a halfwidth of the size distribution curve) becomes 20 times as large as the initial value (Fig. 3). The nucleus growth rate V is on the order of 3×10^{-2} nm/s. It should be noted that the average substrate roughness after the preliminary heat treatment at 520°C was about 10 nm. The shape of the nucleus size distribution function determined for various growth times at this temperature (Fig. 2) agrees with the results of theoretical calculations [10].

This pattern of events observed during the low-temperature nucleation and growth of GaN islands on the Si surface can be interpreted as follows. According to the existing concepts [11], the islands grow as a result of the surface diffusion of atoms provided that the mean free path λ_s of these atoms (molecules) is significantly greater than the average island base radius R. Therefore, as long as $\lambda_s \ll R$, the islands may grow both by means of the surface diffusion and by a mechanism of atom (molecule) incorporation into the island (the growth limited by the rate of a chemical reaction on the periphery of the island). Estimates of the mean free paths of Ga and N atoms [10] show that, at T = 520°C, the value of λ_{Ga} is on the order of 100 nm and, hence, the nucleation and growth of GaN must proceed by the surface diffusion mechanism. In this case, the island growth rate expressed by the number of GaN molecules added per second is [10]

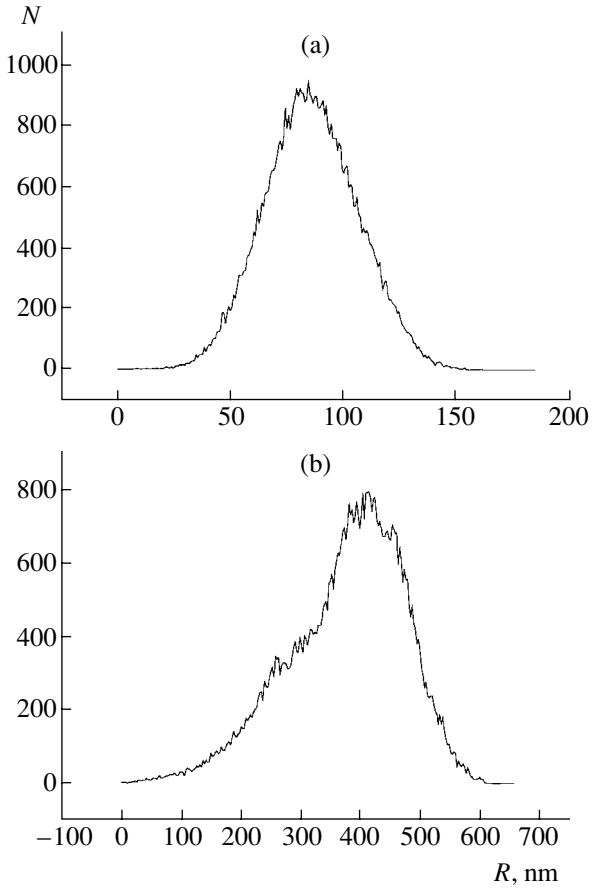

Fig. 2. GaN nucleus size distribution functions determined from AFM data for various times of heteroepitaxial growth: (a) 100 min; (b) 200 min.

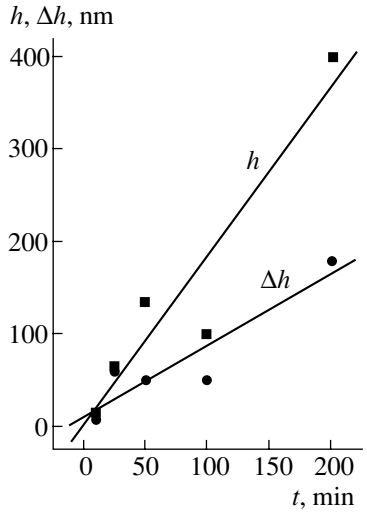

Fig. 3. Plots of the average GaN nucleus (island) height h and average nucleus size scatter Δh versus epitaxial growth time t.

$$V_i = \frac{\xi_{GaN}}{t_0}, \quad (1)$$

where

$$t_0 = \frac{1}{D_s^0 \pi N_0}, \quad (2)$$

$$D_s^0 = \frac{D_{a\mathrm{Ga}} D_{a\mathrm{N}} C_{0\mathrm{Ga}} C_{0\mathrm{N}}}{4(D_{a\mathrm{Ga}} C_{0\mathrm{Ga}} \lambda_{0\mathrm{N}} + D_{a\mathrm{N}} C_{0\mathrm{N}} \lambda_{0\mathrm{Ga}})}, \quad (3)$$

$$\xi_0 = \frac{J_{\mathrm{Ga}} J_{\mathrm{N}} \tau_{\mathrm{Ga}} \tau_{\mathrm{N}}}{N_{sa}} - 1. \quad (4)$$

Here, ξ_{GaN} is the oversaturation with respect to GaN (in a multicomponent system); t_0 is the characteristic GaN island growth time; D_s^0 is the generalized surface diffusion coefficient (characterizing the GaN island boundary propagation velocity); N_0 is the number density of adsorption sites on the substrate surface ($N_0 \sim 1/B^2$, where B is the lattice parameter of the SiO_2/Si substrate); J_i is the flux of atoms incident onto the substrate surface; τ_i is the lifetime of the ith component on the substrate surface; $N_{sa} = C_{0\mathrm{Ga}} C_{0\mathrm{N}} N_0$, $C_{0\mathrm{Ga}}$ and $C_{0\mathrm{N}}$ being the equilibrium concentrations of Ga and N, respectively, and N_0, the equilibrium number density of GaN molecules on the substrate surface; D_{ai} is the diffusion coefficient of the ith component; and λ_{si} is the mean free path of the corresponding atoms on the substrate surface.

Estimates obtained using Eqs. (1)–(4) for $T = 520°C$ showed that the time τ_0 is sufficiently large ($\sim 2 \times 10^4$ s) and the oversaturation is $\xi_0 \sim 1$. The island growth rate V_i is on the order of 5×10^{-5} mol/s, or $V \sim 1 \times 10^{-2}$ nm/s (for $h = R$), which is in good agreement with the experimental data.

Thus, the initial growth stage of GaN layers during HVPE on the oxidized silicon surface involves the nucleation of GaN islands with the initial dimensions on the order of 10 nm. The experimentally determined growth rate of GaN nuclei and their size distribution function determined by from the AFM data are in good agreement with the values calculated using the theory of the initial GaN growth stage developed in [10].

Acknowledgments. This study was partly supported by the Federal program "Surface Atomic Structures," project no. 5-4-99. The authors also gratefully acknowledge the support from the St. Petersburg Scientific Center of the Russian Academy of Sciences and the St. Petersburg Foundation for Support of Science and Education.

REFERENCES

1. H. P. Maruska and J. J. Tietjen, Appl. Phys. Lett. **15**, 327 (1969).
2. H. Amano, N. Sawaki, I. Akasaki, and Y. Toyoda, Appl. Phys. Lett. **48**, 353 (1986).
3. S. Nakamura, M. Senoh, S. Nagahama, *et al.*, Appl. Phys. Lett. **73**, 832 (1998).
4. P. R. Tavernier, E. V. Etzkon, Y. Wang, and D. R. Clarke, Appl. Phys. Lett. **77**, 1804 (2000).
5. S. H. Cheung, L. X. Zheng, M. H. Xie, and S. Y. Tong, Phys. Rev. B **64**, 033304 (2001).
6. K. Yamada, H. Asahi, H. Tampo, *et al.*, Appl. Phys. Lett. **78**, 2849 (2001).
7. A. J. Norejka and D. W. Ing, J. Appl. Phys. **39**, 5578 (1968).
8. I. Bauer, L. Biste, and D. Bolze, Phys. Status Solidi A **39**, 173 (1977).
9. A. N. Efimov, A. O. Lebedev, and A. M. Tsaregorodtsev, Pis'ma Zh. Tekh. Fiz. **24** (20), 52 (1998) [Tech. Phys. Lett. **24**, 810 (1998)].
10. S. A. Kukushkin, V. N. Bessolov, A. V. Osipov, and A. V. Luk'yanov, Fiz. Tverd. Tela (St. Petersburg) **43** (12), 2135 (2001) [Phys. Solid State **43**, 2229 (2001)].
11. S. A. Kukushkin and V. V. Slezov, *Disperse Systems on Solid Surfaces* (Nauka, St. Petersburg, 1996).

Translated by P. Pozdeev

Technical Physics Letters, Vol. 27, No. 12, 2001, pp. 1013–1015. Translated from Pis'ma v Zhurnal Tekhnicheskoĭ Fiziki, Vol. 27, No. 23, 2001, pp. 67–72.

Depth Profiles of the Majority Carrier Concentration and the Minority Carrier Effective Lifetime in Gettered GaAs

V. F. Andrievskii[a], A. T. Gorelenok[a], N. A. Zagorel'skaya[b], A. V. Kamanin[a,*], and N. M. Shmidt[a]

[a] *Ioffe Physicotechnical Institute, Russian Academy of Sciences, St. Petersburg, 194021 Russia*
[b] *Institute of Electronics, National Academy of Sciences of Belarus, Minsk, Belarus*
* *e-mail: kamanin@ffm.ioffe.rssi.ru*

Received July 4, 2001

Abstract—The first results are reported on the concentration profiles of majority carriers and the effective lifetime profiles of minority carriers in thick (1.6 mm) GaAs plates subjected to surface gettering. It was established that the one- and two-sided coating of the GaAs plates with Y films, followed by heat treatment at 700–800°C, allows a high-resistivity material to be obtained with homogeneous distributions of the electron concentration and the hole lifetime in depth of the semiconductor. © *2001 MAIK "Nauka/Interperiodica".*

1. Previously [1], we reported on the surface gettering of high-resistivity ($\rho = 10^8\ \Omega$ cm) chromium-doped GaAs with (111) and (100) orientations. The 0.3-mm-thick GaAs plates were coated with SiO_2, Si–(W, Cr), or Si–Cr getter films with a thickness of ~1000 Å and heat treated at 826–926°C for 15–45 h. As a result of this treatment, the dislocation density and mechanical stresses in GaAs decreased, while the resistivity and carrier mobility somewhat increased. Recently [2–4], we studied the process of surface gettering in thick (1.6 mm) (111)-oriented undoped GaAs plates grown by the Czochralski method from a Ga–As melt. The initial material of the 7N purity grade [5] had a carrier concentration of $(1–3) \times 10^{15}$ cm^{-3} and a mobility of 1500–2000 cm^2 V^{-1} s^{-1} at 300 K. The carrier concentration in this material was determined by the density of intrinsic defects (of the V_{Ga}, V_{As}, I_{Ga}, I_{As}, As_{Ga}, and Ga_{As} types and various complexes) rather than by the background concentration of residual impurities. The gettering was effected by coating the GaAs plates with ~1000-Å-thick yttrium films from both sides, followed by heat treatment at 800°C for 0.5–5 h. Using this gettering treatment, it was possible to obtain GaAs with $N_d - N_a = 10^8–10^{14}$ cm^{-3} and a maximum mobility of up to 7000 cm^2/(V^{-1} s^{-1}) at 300 K depending on the thermal treatment regime.

2. The purpose of this study was to determine the concentration profiles of majority carriers and the effective lifetime profiles of minority carriers in thick high-resistivity GaAs plates gettered by one- or two-sided coating with Y films according to [2–4]. The majority carrier concentration and minority carrier lifetime distributions were determined by photoelectrochemical *C–V* profiling techniques.

3. The experiments were performed on thick (1.6 mm) GaAs plates gettered as described in [2–4] by one- or two-side coating with ~1000-Å-thick Y films and sequential annealing in a pure hydrogen atmosphere for 0.25 h at 700°C and 0.5 h at 800°C. After this treatment, the Y getter films were removed by plasma etching in a RIBES Rokappa setup.

The concentration profiles of majority carriers and the effective lifetime profiles of minority carriers were determined by electrochemical [6] and photoelectrochemical [7] methods. These techniques are based on measuring the capacitance–voltage (*C–V*) characteristics and photoinduced current in the Schottky barrier between GaAs and electrolyte. The electrolyte simultaneously serves as an etchant for GaAs, which provides for a continuous etching of the semiconductor plate. The depth–concentration profile of the majority carriers is described by the formula [6]

$$N(x) = -\frac{C^3}{e\varepsilon\varepsilon_0 A^2}\left(\frac{\Delta C}{\Delta V}\right)^{-1}, \qquad (1)$$

where C is the capacitance of the space charge region in GaAs; e is the electron charge; ε and ε_0 are the permittivity and dielectric constant, respectively; A is the Schottky contact area, and $\Delta C/\Delta V$ is the ratio of the capacitance and voltage increments.

The electrolyte was an H_2SO_4–H_2O_2–H_2O (1 : 8 : 1) mixture—a polishing etchant specially developed for the *C–V* profiling of high-resistivity GaAs [8]. This solution ensures the etching of GaAs at a constant rate over several days. The GaAs plate was in contact with the etching electrolyte in a chemical cell; the circular contact area had a diameter of 3 mm. When the carrier concentration profile is measured to a large depth, the propagation of the sample–electrolyte interface in

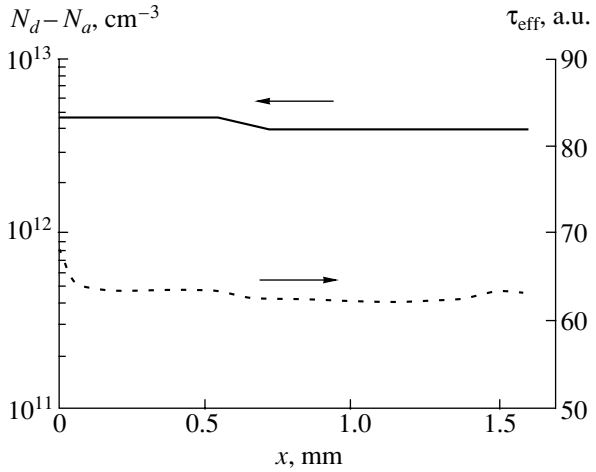

Fig. 1. Depth profiles of $N_d - N_a$ and τ_{eff} in a GaAs plate Y-gettered from both sides (800°C, 0.5 h).

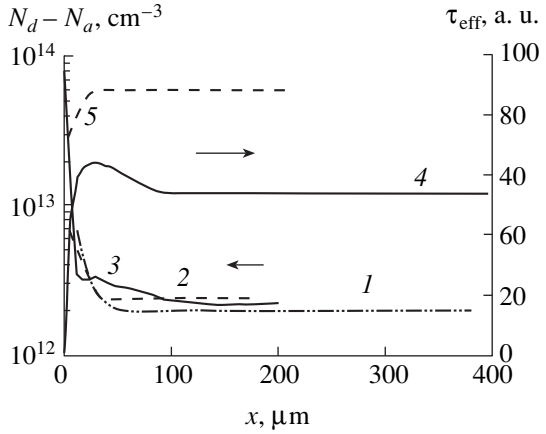

Fig. 2. Depth profiles of $N_d - N_a$ and τ_{eff} in the surface layers of GaAs plates Y-gettered from one side: (*1*, *4*) coated side (800°C, 0.5 h); (*2*, *5*) coated side (700°C, 0.25 h); (*3*) uncoated side (800°C, 0.5 h).

depth of the plate leads to an increase in the contact area due to the formation of a cylindrical local etching region. The side surface of this etching cylinder also contributes to the measured capacitance. Thus, the measured signal includes two components related to the capacitance of the side surface and bottom of the etching cylinder. The side surface contribution to the capacitance C_I can be calculated as an arithmetic mean by the formula

$$C_I = \frac{2}{r}\int_0^h C dh, \qquad (2)$$

where r is the contact radius and h is the cylinder height. The charge carrier concentration was calculated using the capacitance determined as a difference between capacitances of the space charge region and the etching cylinder side surface (C_I) [8].

The effective lifetime of minority carriers (τ_{eff}) was determined as proportional to the photocurrent passing through a Schottky barrier in the system irradiated by light with a quantum energy of $h\nu > E_g$ [9]. Thus, the photocurrent measurements in the electrolyte–semiconductor system in the course of chemical etching of a high-resistivity GaAs allowed simultaneous determination of the qualitative distribution of the hole lifetime and the electron concentration in depth of the sample plate.

4. Preliminary investigation of the carrier depth–concentration profile in a Hg–GaAs Schottky barrier in the course of layer removal in the H_2SO_4–H_2O_2–H_2O (1 : 8 : 50) etchant (etching rate, 1000 Å/min) showed that the sample surface upon gettering in the one-sided Y–GaAs structures for 0.25 h at 800°C and plasma etching of the Y film is characterized by conductivity of the hole type with $p \simeq 10^{16}$ cm^{-3} to a depth of ~0.5 μm. After this treatment (800°C, 0.25 h), the sample surface not coated with Y also exhibited the hole type conductivity with $p \simeq 10^{17}$ cm^{-3}, but the p-layer thickness reached several microns. At a greater depth, the material on both sides of the sample exhibited inversion of the conductivity type, with an electron concentration of ~10^{13} cm^{-3} or below.

Figure 1 shows the depth profiles of the majority carrier concentration $N_d - N_a$ and the minority carrier effective lifetime τ_{eff} in GaAs plates Y-gettered by annealing at 800°C for 0.5 h. As can be seen, the profiles are virtually homogeneous. A weak decrease in $N_d - N_a$ at a depth greater than 600 μm is related to a large uncertainty of the capacitance measurements caused by nonuniform etching in various crystallographic directions.

In the case of gettering at 700°C for 0.25 h with one- and two-sided Y coating, a surface layer of the samples upon the Y film removal by plasma etching exhibits electron conductivity with $n \simeq 10^{13}$–10^{14} cm^{-3}. The thickness of this layer reached several microns. At a greater depth, the carrier concentration decreased to 10^{12} cm^{-3} and below, depending on the annealing regime (Fig. 2).

An analysis of the data in Figs. 1 and 2 leads to a conclusion that the gettering process exhibits a volume character even when only one side of a GaAs plate is coated with yttrium. However, the uncoated surface seems to contribute to the gettering effect as well. Figure 2 shows that the τ_{eff} profile is homogeneous in depth of the samples gettered both at 700 and 800°C, while the τ_{eff} value in the former case is 30% higher than that in the latter. The shape of the $N_d - N_a$ profiles suggests that the gettering process is accompanied by generation of the opposite defects such as As_{Ga} and Ga_{As} and, probably, of the intrinsic defects of various types (V_{Ga}, V_{As}, I_{Ga}, I_{As}). The major role in the gettering process apparently belongs to spatial separation of the opposite defects and the formation of complexes involving these

defects rather than to the direct annihilation of such pairs. This accounts for a decrease in the carrier concentration down to 10^8 cm^{-3} [2].

5. We have demonstrated that the surface gettering in GaAs yttrium-coated from one or two sides possesses a volume character and can be performed at relatively low temperatures (700°C). Using this method, it is possible to obtain high-resistivity GaAs palates with homogeneous distributions of $N_d - N_a$ and τ_{eff} in depth of the semiconductor plates with a thickness of up to 1.5 mm. The electron mobility in the gettered GaAs may reach up to 7000 cm^2 V^{-1} s^{-1} at 300 K [3]. The gettered GaAs is a promising material for high-voltage and high-power semiconductor devices, X-ray and nuclear radiation and particle detectors (including neutrinos), and ultrahigh-speed optoelectronic VLSIs. The gettering procedure is very simple and can be readily implemented into a traditional wafer technology, requiring only three additional stages (getter application, heat treatment, and getter removal).

Acknowledgments. The authors are grateful to M. Mezdrogina for depositing Y coatings and to Yu. Zadiranov for the plasma-etching removal of these films.

This study was supported by the Russian Foundation for Basic Research, project no. 00-02-17026.

REFERENCES

1. A. T. Gorelenok, V. L. Kryukov, and G. P. Furmanov, Pis'ma Zh. Tekh. Fiz. **20** (13), 60 (1994) [Tech. Phys. Lett. **20**, 546 (1994)].
2. N. Shmidt, A. Gorelenok, V. Emtsev, *et al.*, Solid State Phenom. **69**–**70**, 279 (1999).
3. L. S. Vlasenko, A. T. Gorelenok, V. V. Emtsev, *et al.*, Fiz. Tekh. Poluprovodn. (St. Petersburg) **35** (2), 184 (2001) [Semiconductors **35**, 177 (2001)].
4. L. S. Vlasenko, A. T. Gorelenok, V. V. Emtsev, *et al.*, Pis'ma Zh. Tekh. Fiz. **27** (1), 19 (2001) [Tech. Phys. Lett. **27**, 9 (2001)].
5. A. V. Markov, A. Y. Polyakov, N. B. Smirnov, *et al.*, Nucl. Instrum. Methods Phys. Res. A **439**, 651 (2000).
6. J. Reichman, Appl. Phys. Lett. **36** (7), 574 (1980).
7. V. F. Andrievskii, in *Theory, Methods and Instrumentation for the Measurement and Control of the Parameters of Magnetic, Semiconducting and Dielectric Materials: A Collection of Papers* (Novocherkassk, 2000), Part 4, p. 24.
8. V. F. Andrievskii, E. V. Yakimenko, and O. K. Muravitskiĭ, USSR Inventor's Certificate No. 1611075, G01 NL 27/22 (1989).
9. S. Sze, *Physics of Semiconductor Devices* (Wiley, New York, 1981; Mir, Moscow, 1984), Vol. 1.

Translated by P. Pozdeev

Technical Physics Letters, Vol. 27, No. 12, 2001, pp. 1016–1017. Translated from Pis'ma v Zhurnal Tekhnicheskoĭ Fiziki, Vol. 27, No. 23, 2001, pp. 73–76.

On the Possibility of Decreasing Spherical and Chromatic Aberrations in Flat Combined Axisymmetric Magnetoelectrostatic Lenses

V. A. Zhukov, Yu. V. Vorob'ev, and M. M. Nesterov

Institute of Informatics and Automation, Russian Academy of Sciences, St. Petersburg, Russia

e-mail: v-zhukov@cards.lanck.net

Received May 11, 2001; in final form, July 17, 2001

Abstract—It is shown that the coefficients of both spherical and chromatic aberrations in flat combined axisymmetric magnetoelectrostatic lenses can be decreased by a factor of six as compared to the analogous coefficients for pure magnetic lenses, provided appropriate values are selected for the ratio of dimensions of the electrodes and pole tips of the combined lens, electric potentials on the electrodes, and ampere-turns of the field-exciting coil. © *2001 MAIK "Nauka/Interperiodica".*

The task of decreasing spherical and chromatic axial aberrations is currently important in the development of electron and ion optics of axisymmetric electron-optical systems (EOSs) [1, 2]. There were numerous attempts, more or less successful, at decreasing these aberrations both in purely electrostatic or magnetic EOSs and in combined systems [3–5] through the optimization of the spatial arrangement of the field sources. For EOSs of the first two types, some general principles for reducing aberrations were formulated [2]. Unfortunately, no such general principles were established for the more complicated combined systems.

Various researchers [3–5] considered the use of combined axisymmetric lenses in low-voltage electron microscopy. In these systems, the axial aberration coefficients were reduced by decelerating electrons in front of an object positioned outside the field of the objective lens. As a result, the axial aberration coefficients were decreased by a factor of 1.4 [3] and about 3 [4, 5].

Below, we will consider a flat combined electromagnetic lens (see figure) described recently [6]. In this system, an object irradiated by electrons is placed (in contrast to the cases described in the papers cited above [3–5]) into a combined electromagnetic field of the flat objective lens. This arrangement (immersion) is expected, by analogy with the case of a pure magnetic lens [7], to allow an additional reduction in the axial aberrations in comparison with that achieved in [3–5].

In the proposed system, the magnetoelectrostatic lens comprises a combination of two lenses with a common axis. The first is a flat three-electrode electrostatic lens made of a nonmagnetic material. In the figure, r_1 and r_2 are the inner radii of concentric insulating ring gaps, R_1 and R_2 being the corresponding outer radii; ϕ_1, ϕ_2, and ϕ_3 are the potentials of these electrodes, from central to peripheral. The electrostatic potential on the EOS axis is described as a function of the axial coordinate z by the following formula [6]:

$$\Phi_E(z) = \frac{\phi_2 - \phi_1}{\ln(r_1/R_1)} \ln\left(\frac{z + \sqrt{z^2 + R_1^2}}{z + \sqrt{z^2 + r_1^2}}\right) + \frac{\phi_3 - \phi_2}{\ln(r_2/R_2)} \ln\left(\frac{z + \sqrt{z^2 + R_2^2}}{z + \sqrt{z^2 + r_2^2}}\right) + \phi_3. \quad (1)$$

The second lens is a flat magnetic lens with a ring-shaped nonmagnetic gap (ρ_1 and ρ_2 being the inner and outer radii), the magnetic field of which $B_z(0, 0, z)$ along the z axis varies as described by the formula [8, 9]

$$B_z(0, 0, z) = D[(\rho_1^2 + (z + \Delta)^2)^{-1/2} - (\rho_2^2 + (z + \Delta)^2)^{-1/2}], \quad (2)$$

where $D = \mu_0(NI)[\ln(\rho_1/\rho_2)]^{-1}$, $\mu_0 = 4\pi \times 10^{-7}$ H/m is the magnetic constant of vacuum (in SI units), NI is the number of ampere-turns in the field-exciting coil, and Δ is the distance between the centers of electrostatic (1) and magnetic (2) lenses along the z axis.

We have calculated the paraxial trajectories of charged particles in the focusing field, representing a sum of the fields described by formulas (1) and (2). Based on the results of these calculations, taking into account higher orders of expansions of the field strengths into series in powers of the radial coordinate perpendicular to the z axis, and using integral formulas for the aberration coefficients [2], we calculated coefficients (related to the EOS focal distance) of the aforementioned axial aberrations under "zero magnification" conditions (i.e., for the infinitely distant electron source).

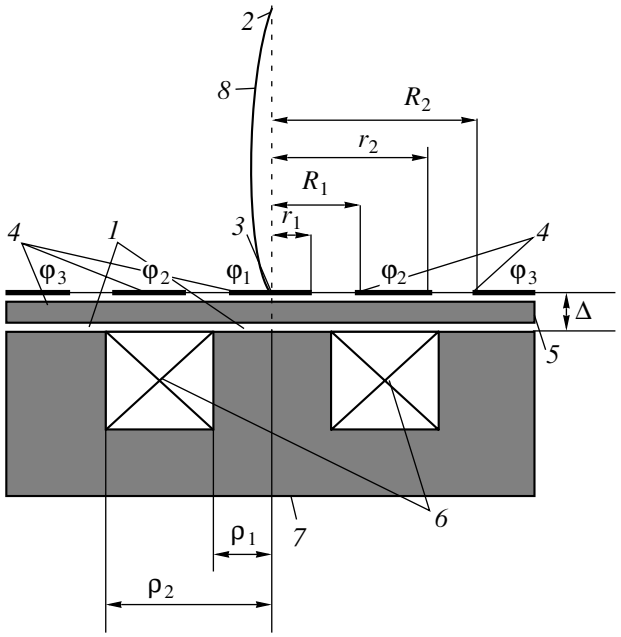

Schematic diagram of a flat combined axisymmetric magnetoelectrostatic lens: (*1*) magnetic poles; (*2*) electron source; (*3*) electron source image; (*4*) electrodes; (*5*) insulator; (*6*) focusing coil; (*7*) ferromagnet; (*8*) paraxial electron trajectory.

The results of these calculations showed that a decrease in the aberration coefficients is observed for at least two different configurations of the field sources: (i) for an additional accelerating potential applied to the first electrode of the electrostatic lens, a decelerating potential applied to the second electrode, and grounded third electrode; (ii) for the opposite variant, whereby potentials of the opposite signs are applied to the electrodes (with some changes in the values of potentials and the dimensions of electrodes). The widths of insulating gaps between electrodes were selected much smaller (about ten times) than their inner radii, which ensured the validity of the approximations used to derive the analytical field equation (1) and allowed us ignore the effect of the electric potential distribution at the poles of the magnetic lens on the halfspace above electrodes. The inner and outer radii of the nonmagnetic gap were selected so as to provide that a "half-width" of the axial distribution of the *z*-component of the magnetic field would be approximately equal to the radius of the inner electrode. The ampere-turns in the field-exciting coil were selected so that the paraxial trajectories in the combined field would be focused at $z = 0$.

Under these conditions, it is possible to decrease the coefficients of both chromatic and spherical aberrations to approximately one-sixth of the values for the purely magnetic lens. This effect is twice as large as that achieved in [5], which confirms our expectations (based on the results presented in [7]) concerning the use of immersion conditions in the combined objective. The application of combined lenses of the type considered above may be promising in the ion and electron projectors and microprobe systems, especially in those intended for the microlithography purposes [10].

REFERENCES

1. O. Scherzer, Optik (Stuttgart) **2**, 114 (1947).
2. M. Szilgui, *Electron and Ion Optics* (Plenum, New York, 1988).
3. Yu. F. Shchetnev, Tr. Gos. Opt. Inst. **58** (192), 42 (1982).
4. J. Froisen, E. Plies, and K. Auger, J. Vac. Sci. Technol. B **7**, 1874 (1989).
5. S. Beck, E. Plies, and B. Schiebel, Nucl. Instrum. Methods Phys. Res. A **363**, 31 (1995).
6. V. A. Zhukov, A. V. Zav'yalova, Yu. V. Vorob'ev, and V. D. Gelever, in *Proceedings of the 18th All-Russia Conference on Electron Microscopy, Chernogolovka, 2000*, p. 111.
7. W. Glaser, *Grundlagen der Elektronenoptik* (Springer, Vienna, 1952; Gostekhizdat, Moscow, 1957).
8. V. A. Zhukov, E. N. Kotlikov, and V. D. Gelever, Zh. Tekh. Fiz. **69** (8), 133 (1999) [Tech. Phys. **44**, 990 (1999)].
9. V. A. Zhukov, V. D. Gelever, A. V. Zav'yalova, and Yu. V. Vorob'ev, Izv. Akad. Nauk, Ser. Fiz. **64** (8), 1584 (2000).
10. G. Gross, R. Kaesmaier, H. Loschner, *et al.*, J. Vac. Sci. Technol. B **16**, 3150 (1998).

Translated by P. Pozdeev

Technical Physics Letters, Vol. 27, No. 12, 2001, pp. 1018–1020. Translated from Pis'ma v Zhurnal Tekhnicheskoĭ Fiziki, Vol. 27, No. 23, 2001, pp. 77–83.

Vacuum Discharge as an Effective Source of Multiply Charged Ions

M. F. Artamonov, V. I. Krasov, and V. L. Paperny*

Irkutsk State University, Irkutsk, Russia

** e-mail: paperny@math.isu.runnet.ru*

Received July 10, 2001

Abstract—The time-of-flight (TOF) spectra measured under high vacuum conditions revealed ion beams of a cathode material (Cu^{n+}) with a maximum charge of up to +19 generated in the initial stage of a spark discharge development at a storage voltage of up to U_0 = 2.5 kV. As the U_0 value increases, the range of the multiply charged states of ions detected by the TOF technique increases, the average ion charge reaching +9. © *2001 MAIK "Nauka/Interperiodica".*

Introduction. Creation of the sources of high-energy multiply charged metal ions is of interest for materials science and microelectronics. A promising type of such ion sources is offered by a high-vacuum spark discharge. Using this process, it is possible to obtain, at a relatively low total energy consumption and rather simple system design, a sufficiently high energy density in the plasma column that is necessary for the multiply charged ion production. However, many years of attempts showed that a maximum ion charge detected in the plasmas of vacuum spark discharges of various types did not exceed +7 (W^{7+} [1], Cu^{7+} [2]), although the voltage applied to the interelectrode gap in these experiments reached up to several tens [2] or even hundreds of kilovolts [1].

Previously [3, 4], we studied the vacuum spark discharge at relatively low storage voltages (not exceeding 1.5 kV) and observed the beams of cathode material ions (Cu^+, Cu^{2+}) with energies of up to 10 keV. Below, we report on the results obtained in an experimental setup analogous to that employed previously but under significantly improved vacuum conditions: a residual gas pressure in the working chamber was one and a half orders of magnitude lower as compared to that reached in [3, 4]. The purpose of our experiments was to detect ions of the cathode material with a high degree of ionization, the content of which sharply drops when the working chamber pressure increases above 10^{-5} Torr [5].

Experimental procedure. The experiments were performed with a vacuum spark discharge obtained using a storage voltage of up to U_0 = 2.5 kV. The electrode system comprised a copper cathode with a diameter of 1 mm and a flat grounded grid anode spaced by 9 mm from the cathode. The vacuum in the working chamber was no worse than $(5–8) \times 10^{-6}$ Torr. The discharge was initiated at the cathode edge by breakdown over the surface of a dielectric spacer between the cathode and the igniter. The discharge current was maintained by a capacitor (C = 2 μF) and measured with the aid of a Rogovsky coil immediately in the cathode circuit. The total inductance in the discharge circuit did not exceed 40 nH. Prior to measurements, the electrode system was trained by approximately 10^3 shots, after which the discharge current scatter in various experiments did not exceed 20%.

The ion energy and charge distribution was studied by the time-of-flight (TOF) method using an electrostatic energy analyzer of the plane capacitor type possessing an energy resolution of $\Delta\varepsilon/\varepsilon \approx 2 \times 10^{-2}$ and a detector time resolution of about 40 ns. The analyzer was arranged behind the grid anode and detected ions emitted from the cathode torch, moving along the discharge axis toward the anode.

Using the TOF technique, it is possible to determine the μ/Z ratio (μ is the atomic weight and eZ is the ion charge) for each type of ions by measuring a delay time of the corresponding detector signal for a detected ion energy ε/Z determined by a voltage applied to the energy analyzer plates. For ions with a given atomic number, the charge resolution $\alpha = Z/\Delta Z$ is determined by the energy resolution of the analyzer, the time resolution of the detector circuit, the length of the ion production zone, and the measured flight time for ions traveling from the production zone to the detector. Under the experimental conditions studied, the ion flight path length was 60 cm and the charge resolution for Cu^{n+} ions was $\alpha(\varepsilon) = 20$.

Experimental results. Figure 1a shows a typical oscillogram of the discharge current measured at a storage voltage of 2.0 kV. The use of a low-inductance discharge circuit ensured a high rate of the current buildup (up to 2×10^{10} A/s) at a relatively low storage voltage. Figure 1b shows a typical analyzer signal (TOF spectrum) measured at a fixed ion energy of ε/Z = 2.1 keV.

1063-7850/01/2712-1018$21.00 © 2001 MAIK "Nauka/Interperiodica"

Assuming that the last peak in the spectrum of Fig. 1b corresponds to Cu^+ ions (characterized by the maximum value of $\mu/Z = 64$ and, hence, by a maximum flight time), we can determine the start instant for these ions (indicated by arrows in Figs. 1a and 1b). According to the time delays of the other peaks relative to the start instant, we can determine the μ/Z values for ions corresponding to these peaks. Thus, the values of μ/Z = 32, 21, and so on, are naturally assigned to Cu^{2+}, Cu^{3+}, …, respectively (assuming that the ions in all charged states are produced simultaneously).

As can be seen in Fig. 1b, a significant peak of H^+ ions was detected in addition to copper ions representing the cathode material. Moreover, the detected signal may also contain contribution due to ions of the other light impurities desorbed from the surface of the cathode and the dielectric spacer (O^{n+}, C^{n+}, N^{n+} with n = 1, 2), which possess the μ/Z values close to those for some copper ions (e.g., Cu^{4+}, Cu^{5+}, Cu^{8+}, etc.). These light ions were also detected in our previous experiments [3, 4]. However, a thorough analysis of the data obtained in this study showed that improved vacuum conditions and prolonged pretreatment of the electrode system led to a significant decrease in the content of impurity ions in the discharge plasma, which produce only an insignificant contribution to the charged beam composition. This conclusion agrees with the results of analogous measurements in a laser plasma, where the signals of multiply charged metal ions were accompanied by an intense signal due to hydrogen ions; the H^+ signal was 5–10 times as great as the peaks of other light impurities, the influence of which on the overall distribution of charged states was ignored [6].

The signals of ions in a given charged state Cu^{n+} detected in various shots at a fixed storage voltage exhibited a considerable scatter in the amplitude. For the subsequent treatment, each signal amplitude was averaged in a series of 12 shots. These averaged signal amplitudes, corresponding to ions in a certain charged state, were measured at various ε/Z values and used to construct the energy spectrum of ions produced in the discharge.

By integrating the spectra of ions in various charged states measured at various energies, we determined a distribution of the discharge-induced copper ions with respect to charge. Figure 2 shows such distributions for two values of the storage voltage U_0. As can be seen, an increase in the U_0 value leads to expansion of the range of the multiply charged states of ions detected by the TOF. The maximum copper ion charge observed under the experimental conditions studied was +19.

An important parameter characterizing the efficiency of the operating ionization mechanism is the average ion beam charge determined from the ion charge distributions. Figure 3 presents a plot of this parameter versus the storage voltage showing that the average ion charge monotonically increases with U_0.

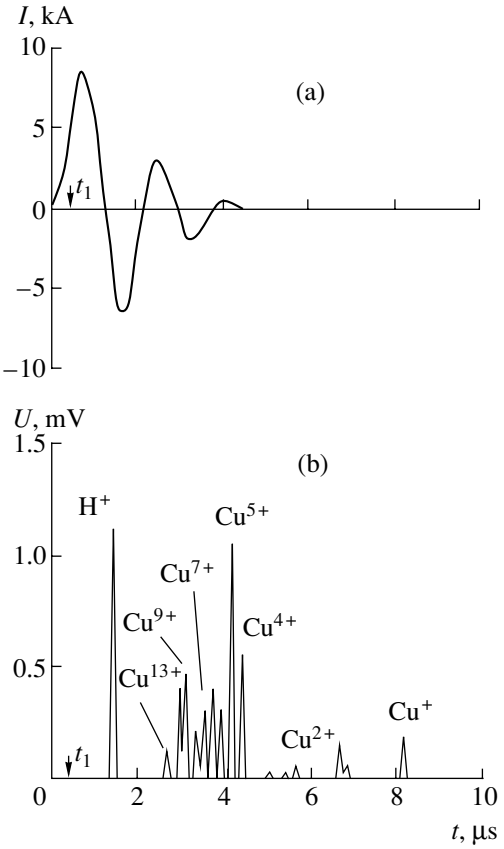

Fig. 1. Typical oscillograms of (a) the discharge current measured at a storage voltage of 2.0 kV and (b) the corresponding analyzer signal (TOF spectrum) measured for Cu^{n+} ions at a fixed ion energy of ε/Z = 2.1 keV.

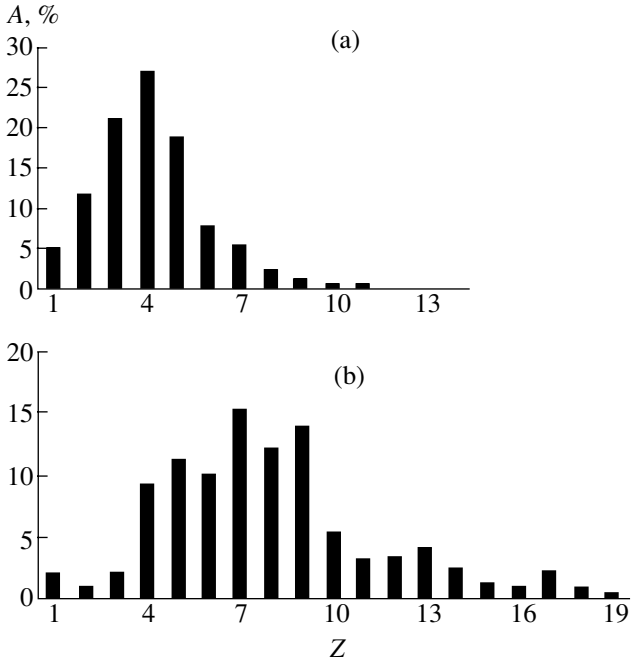

Fig. 2. Histograms showing the charge distribution in a Cu^{n+} ion beam formed in a spark discharge at a storage voltage of U_0 = 0.3kV (a) and 2.0 kV (b).

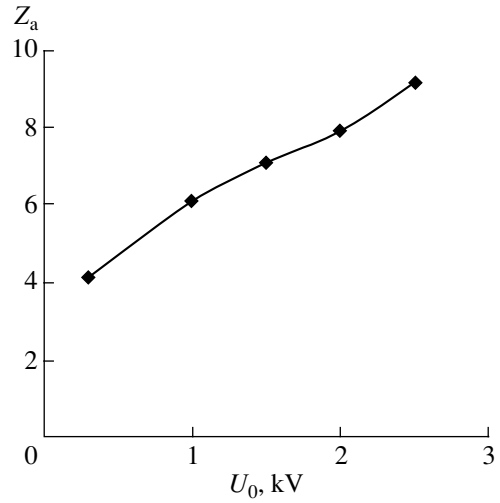

Fig. 3. The plot of average copper ion charge Z_a versus storage voltage U_0.

For the maximum storage voltage (U_0 = 2.5 kV) employed in this study, the average ion charge reaches +9.

Discussion. The results of our experiments showed that a cathode plasma torch of the vacuum spark discharge generates short bunches of multiply charged ions of the cathode material. The process takes place in the initial stage of the discharge, delayed by $t_1 \approx 300$–400 ns from the onset. According to the previous analysis, the moment t_1 of the ion production is close to the time instant t_m of attaining a maximum discharge current buildup rate: $t_1 \le t_m$ [4]. On the other hand, it is known that the process of the interelectrode gap filling by the plasma (i.e., the "spark" stage with a duration of t_s) terminates on reaching the maximum discharge current buildup rate: $t_s \ge t_m$ [7]. From this, we may conclude that the multiply charged ions are ejected from a local region at the front of the propagating cathode plasma torch before this boundary reaches the anode. It should be pointed out that in [2], where ions of the cathode material (Cu^{n+}) were also detected for a discharge current on the order of 10 kA, the maximum ion charge (not exceeding +7) was significantly lower as compared to our values. However, in contrast to our experiment, the measurements in [2] were performed in a late stage of the discharge, when the plasma had already filled the interelectrode gap. This comparison indicates that a significant role in the multiply charged ion production belongs to a free boundary of the cathode plasma torch expanding into vacuum.

The results obtained in this study indicate that a vacuum spark discharge at a relatively low storage voltage and energy can be used as a source of multiply charged ions. The charge composition of the ion beam, which can be controlled within broad limits by the storage voltage, approaches the charge composition of a plasma generated in a target of the same material by a high-power laser pulse [6] with an energy greater by two orders of magnitude than the values used in our experiments.

REFERENCES

1. K. D. Korop and A. A. Plyutto, Zh. Tekh. Fiz. **41** (5), 1055 (1971) [Sov. Phys. Tech. Phys. **16**, 830 (1971)].
2. A. Anders, I. G. Brown, R. A. MacGill, *et al.*, IEEE Trans. Plasma Sci. **25** (4), 718 (1997).
3. N. V. Astrakhantsev, V. I. Krasov, and V. L. Paperny, J. Phys. D **28** (12), 2514 (1995).
4. N. V. Astrakhantsev, A. V. Vanteev, A. A. Varnakov, *et al.*, Pis'ma Zh. Tekh. Fiz. **21** (11), 37 (1995) [Tech. Phys. Lett. **21**, 412 (1995)].
5. A. G. Nikolaev, E. M. Oks, and G. Yu. Yushkov, Zh. Tekh. Fiz. **68** (9), 24 (1998) [Tech. Phys. **43**, 1031 (1998)].
6. W. Mroz, P. Paris, J. Wolowski, *et al.*, Fusion Eng. Des. **32**–**33**, 425 (1996).
7. D. F. Alferov, N. I. Korobova, and I. O. Sibiryak, Fiz. Plazmy **19** (3), 399 (1993) [Plasma Phys. Rep. **19**, 207 (1993)].

Translated by P. Pozdeev

Technical Physics Letters, Vol. 27, No. 12, 2001, pp. 1021–1023. Translated from Pis'ma v Zhurnal Tekhnicheskoĭ Fiziki, Vol. 27, No. 23, 2001, pp. 84–89.

The Character of Terahertz Oscillations in Resonance Tunneling Structures

É. A. Poltoratskiĭ* and G. S. Rychkov

State Research Institute of Physical Problems, Zelenograd, Moscow, Russia

** e-mail: polt@niifp.ru*

Received June 14, 2001

Abstract—A general approach to investigations of the dynamic behavior of nanostructures is developed and applied to the study of complex oscillations in resonance tunneling structures. Using a modified equivalent scheme of a resonance tunneling structure, based on a quantum-mechanical description of the dynamic properties of this structure, the system behavior in the phase space is qualitatively analyzed. It is shown that the system may occur in the state of "soft" or "rigid" excitation of oscillations. *© 2001 MAIK "Nauka/Interperiodica".*

The results of experimental and theoretical investigations show that nanoelements may occur in various dynamic and static equilibrium states. An exact description of the behavior of nanoelements is provided by the methods of quantum physics. However, such a description usually requires the analysis of nonlinear differential equations in partial derivatives; unfortunately, no regular methods for solving such equations have been developed to the present. On the other hand, using numerical methods would be effective only if behavior of a dynamic nanosystem were qualitatively known.

Under these conditions, a natural approach is to consider, based on certain aprioric assumptions, a given nanoelement as an electric system composed of nonlinear resistances, capacitances, and inductances and estimate the system parameters using the apparatus of the quantum mechanics. This approach allows the dynamic states of nanoelements to be qualitatively analyzed in terms of a system of ordinary differential equations, thus revealing complicated dynamic processes underlying nontrivial static features of the nanoelement [1, 2]. An example of this is offered by the presence of a "plateau" and hysteresis loops in the region of a negative differential resistance of a resonance tunneling structure. The results of numerical modeling of the behavior of such structures performed by various researchers showed the possibility of exciting terahertz oscillations of the electric current in these systems, the constant component of which accounts for the plateau [3–7]. The formation of hysteresis loops was explained by the charge redistribution between the emitter and the quantum well [4–7].

The possible excitation of high-frequency oscillations was related to the presence of an inductive element inside the resonance tunneling structure. The role of this element (see [4–7]) is played by a part of the emitter adjacent to the barrier (see the inset in Fig. 1). Introduction of the inductive element allowed Buot *et al.* [7] to describe the "soft" excitation of small oscillations using a system of ordinary differential equations. However, this description provided only a qualitative explanation of the "plateau" because of the smallness of the oscillation amplitude.

With an allowance for the inductive element, an equivalent scheme was suggested [4–7] that is depicted by solid lines in Fig. 1, which can be used to explain behavior of the system only under the action of small high-frequency perturbations. However, the same equivalent scheme completed with a capacitor C (dashed lines in Fig. 1) allows all features of the measured current–voltage characteristic to be explained (including both plateau and hysteresis loops) from a common standpoint. According to this, the oscillatory process (without restrictions to the amplitude) is characterized by the excitation of oscillations in a "soft"

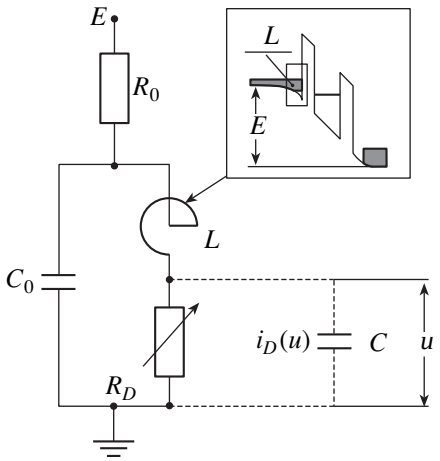

Fig. 1.

1063-7850/01/2712-1021$21.00 © 2001 MAIK "Nauka/Interperiodica"

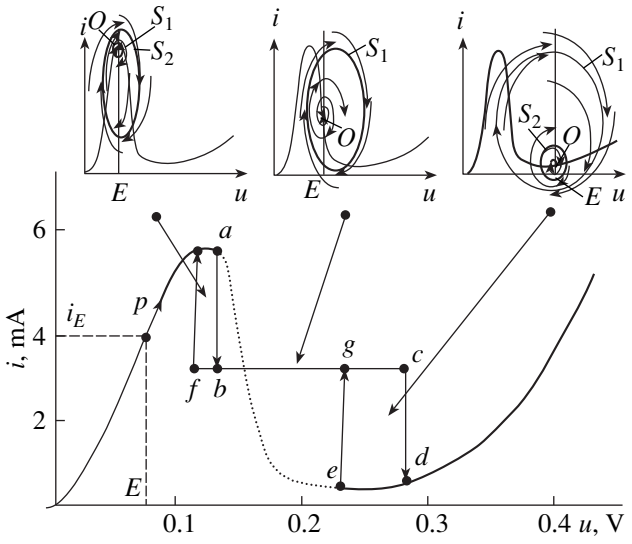

Fig. 2.

regime in the "plateau" region and in a "rigid" regime in the region of hysteresis loops.

The capacitor C, representing capacitance of the quantum well with a charge localized in this well, shunts the nonlinear resistor possessing a static (rather than measurable) current–voltage characteristic $i_D(u)$ of the resonance tunneling structure proper (without contact resistance). Adding this capacitance, even negligibly small, gives rise to high-frequency oscillations in the internal circuit comprising elements L, C, and R_D. An analysis of the oscillations in a dynamic system described by the ordinary differential equations is equivalent to the analysis of limiting cycles of this system.

For the dynamic systems described by the equivalent scheme presented in Fig. 1, criteria of the presence and absence of the limiting cycles were developed in [8–11]. Note that, for $C \ll C_0$, the oscillations $i_D(u)$ arising in the circuit LC are shunted by capacitance C_0 and the C_0R_0 chain is stabilizing the external voltage E applied to this circuit. For simplicity, we will assume that $R_0 = 0$. Then, the number of limiting cycles in the system is merely equal (in a certain approximation) to the number of intersection points of the $i_D(u)$ curve at $u > E$ with the mirror-reflection curve relative to the $u = E$ line. The cycles are embedded into one another and exhibit alternating stability (according to the mirror-reflection criterion [11]).

A static current–voltage characteristic will be selected in the form depicted in Fig. 2. This is a continuous curve with a negative differential resistance region indicated by dashed line. In order to determine a current–voltage characteristic corresponding to the measured one, it is necessary to know the constant component of current oscillations in the circuit. This constant component strongly depends on the character of oscillations, which may vary from harmonic oscillations to relaxation. Our task in this study is to show that the plateau and hysteresis loops exist (rather than to determine the exact positions of these features) and are related to the high-frequency oscillations. For this reason, we will assume that the oscillations exhibit a pronounced relaxation character with an average current of $i_{av} = (I_p + I_v)/2$, where I_p and I_v are the values of $i_D(u)$ at the maximum and minimum, respectively (Fig. 2).

Taking into account the above assumptions and using the "mirror reflection" criterion for the system with $C \neq 0$, we obtain a current–voltage characteristic (solid curve in Fig. 2) that correspond to the measured one. Qualitative changes in the system behavior are most conveniently followed by moving along the current–voltage characteristic with point p, the abscissa and ordinate of which represent the E and i_E values, respectively. This behavior is illustrated by insets in Fig. 2 showing the phase portraits corresponding to indicated regions of the current–voltage characteristic.

As the voltage E increases starting from zero, the dynamic system exhibits only stable static states. When the point p reaches the maximum (point a), the singular point of the system converts from stable to unstable and the system exhibits oscillations (the so-called "soft" excitation). This corresponds to the point p jumping from a to b. As the voltage E increases further, the "soft" excitation regime is retained until point p reaches position g. The segment bg (called the "plateau") corresponds to an unstable singular point O and a stable limiting cycle S_1 in the phase space (see the middle inset in Fig. 2).

The subsequent voltage growth leads to the development of an unstable limiting cycle S_2 from the singular point O, which corresponds to the system passing from "soft" to "rigid" excitation regime. The "rigid" regime is characterized by the existence of two stable states—static (represented by the stable singular point O) and dynamic (represented by the limiting cycle S_1)—which corresponds to the hysteresis loop $gcde$ (see the right-hand inset in Fig. 2). Since the system occurred (with increasing E) in the oscillatory regime, the oscillations will be retained in the "rigid" excitation regime until point p would reach the position c. At this point, the phase portrait of the system features merging of the stable limiting cycle S_1 with unstable cycle S_2. As a result, the system passes to the stable static state O, which is manifested by the point p sharply jumping from c to d.

Now, we will decrease the voltage E and the system will occur in the above stable static state, while possessing a stable dynamic state as well, until the moving point p would reach position e. At this instant, the unstable limiting cycle S_2 merges with the singular point O. This point turns into unstable singular point and the system passes into the "soft" excitation regime that lasts until point p moves to reach position b. As the voltage E is decreased further, the system will occur in the excited state despite possessing a stable static state. In this case, the phase portrait exhibits the stable limit-

ing cycle S_1 and the unstable cycle S_2 (see the left-hand inset in Fig. 2) and the system occurs in the "rigid" excitation regime. Finally, point *p* reaches position *f* where the system passes into a single static state *O*.

Thus, the dynamic processes in the system are manifested by the appearance of two hysteresis loops (related to the "rigid" excitation regime) and a "plateau" (related to the "soft" excitation) in the measured current–voltage characteristic. In order to reveal the "rigid" regime by quantum-mechanical methods, it is necessary to find a "soft" regime and then gradually change the bias voltage so as to enter the "rigid" excitation regime.

Acknowledgments. This study was partly supported by the Joint Russian–Ukrainian Program "Nanophysics and Nanoelectronics."

REFERENCES

1. E. A. Poltoratsky and G. S. Rychkov, in *Abstracts of Invited Lectures and Contributed Papers of the International Symposium "Nanostructures: Physics and Technology," St. Petersburg, 1994*, p. 292.
2. É. A. Poltoratskiĭ and G. S. Rychkov, in *Proceedings of the 2nd International Scientific and Technical Conference "Microelectronics and Information Science," Moscow, Zelenograd, 1997*, p. 66.
3. B. A. Biegel and J. D. Plammer, Phys. Rev. B **54** (11), 8070 (1996).
4. K. L. Jensen and F. A. Buot, Phys. Rev. Lett. **66**, 1078 (1991).
5. F. A. Buot and A. K. Rajagopal, J. Appl. Phys. **76** (9), 5552 (1994).
6. F. A. Buot and A. K. Rajagopal, Mater. Sci. Eng. B **35**, 303 (1995).
7. F. A. Buot, P. Zhao, H. L. Cui, *et al.*, Phys. Rev. B **61** (8), 5644 (2000).
8. G. S. Rychkov, Sib. Mat. Zh. **7** (6), 1425 (1966).
9. G. S. Rychkov, Diff. Uravn. **30** (3), 405 (1994).
10. G. S. Rychkov, Diff. Uravn. **21** (6), 991 (1985).
11. G. S. Rychkov, Doctoral Dissertation (Moscow, 1994).

Translated by P. Pozdeev

Technical Physics Letters, Vol. 27, No. 12, 2001, pp. 1024–1025. Translated from Pis'ma v Zhurnal Tekhnicheskoĭ Fiziki, Vol. 27, No. 23, 2001, pp. 90–94.

The Effect of Water Vapor on the Characteristics of a Pulsed-Periodic Ultraviolet Radiation Source

A. K. Shuaibov, A. I. Dashchenko, and I. V. Shevera

Uzhgorod National University, Uzhgorod, Ukraine

e-mail: ishev@univ.uzhgorod.ua

Received June 26, 2001

Abstract—The effect of a small admixture of water vapor on the optical characteristics of an UV radiation source using a He–air–H_2O mixture as the working medium was studied. The gas mixture was excited in a short-pulse transverse volume discharge operating at a charging voltage of $U_{ch} \le 10$ kV. As the partial pressure of helium was varied in the 10–45 kPa range at an air pressure of P(air) = 130 Pa and the water vapor pressure within $P(H_2O)$ = 50–100 Pa, the main optical emission from plasma in the UV wavelength range was concentrated in a broad band peaked at λ_{max} = 309.7 nm and was two times greater than the intensity of the base emission bands of the nitrogen molecule in this spectral range (λ = 337.1 and 315.9 nm, N_2(C–B)). Adding water vapor to the He–air mixture increases the spectral range of the UV source toward shortwave region, which is related to a spontaneous decay of the products of dissociation of water molecules. © *2001 MAIK "Nauka/Interperiodica".*

One of the most simple types of a pulsed-periodic source of spontaneous optical emission in the 300–400 nm wavelength range is represented by lamps based on the 2^+ system of the nitrogen molecule. These lamps are capable of generating relatively intense UV radiation pulses of a nanosecond and subnanosecond duration [1]. The UV radiation sources of this type can operate using both nitrogen and air as the working gas medium. In the context of the recent development of effective dc discharge lamps using inert gas mixtures with water vapor (λ = 306.4 nm, OH*) [2], it was of interest to study operation of these sources in a pulsed mode and expand the working spectral range by using the emission from nitrogen molecules. In order to eliminate the conditions under which nitrogen molecules would prevail over water molecules, the plasma composition was controlled so as to maintain comparable partial pressures of N_2 and H_2O molecules, $P(N_2, H_2O)$ = 50–130 Pa, while the pressure of the buffer gas (helium) would dominate: P(He) ≥ 10 $P(N_2, H_2O)$.

Below, we present the results of an experimental investigation of the effect of water vapor on the characteristics of a pulsed-periodic UV radiation source employing the 2^+ system of levels of the nitrogen molecule.

A transverse volume discharge was UV-spark-initiated in $18 \times 2.2 \times 1.0$ cm volume, where 2.2 cm is the interelectrode gap width. The discharge circuit included the main storage capacitor with a capacitance of 10 nF, and 9.4-nF pulse-shaping capacitors. The charging voltage was controlled within 7–10 kV. The discharge unit design and the scheme of a circuit measuring the source characteristics were described in more detail elsewhere [3–5]. The partial pressure of air and water vapor in the He–air–H_2O mixture were 130 and 100 Pa, respectively. A discharge current pulse consisted of three halfwaves with a duration of 30–50 ns and a repetition rate of f = 1–5 Hz. The length of the optical emission pulses did not exceed 50–70 ns.

The main intensity of emission from the transverse volume discharge in the He–air–H_2O mixture was concentrated in the region of 280–380 nm, including the most intense N_2(B–C) bands and the bands close to the ON(A–X) system. In order to more reliably identify the emission bands related to the presence of water vapor, the emission spectra from the discharge plasma were measured in the second diffraction order of a grating monochromator (MDR-2) equipped with a 1200 line/mm diffraction grating.

Figure 1 shows a fragment of the emission spectrum in the visible range measured at a resolution of 0.2 nm. As can be seen, this region contains the spectral bands peaked at 587.6 nm (HeI) and 656.3 nm (H_α). The UV emission in the region of 306–316 nm represents a superposition of bands related to a spontaneous decay of the products of dissociation of water molecules (λ_{max} = 307.1, 309.7, 313.8 nm) and the well-known band with λ_{max} = 315.9 nm N_2(C–B)(0–1).

It should be noted that the bands related to the presence of water vapor in the working medium rather poorly correspond to the known OH(A–X) transitions [6, 7]. For example, the band at λ_{max} = 307.1 nm is observed instead of the OH(A–X)(0–0) transition manifested at λ_{max} = 306.4 nm. For this reason, the bands observed in the region of 307–313 nm can be assigned

1063-7850/01/2712-1024$21.00

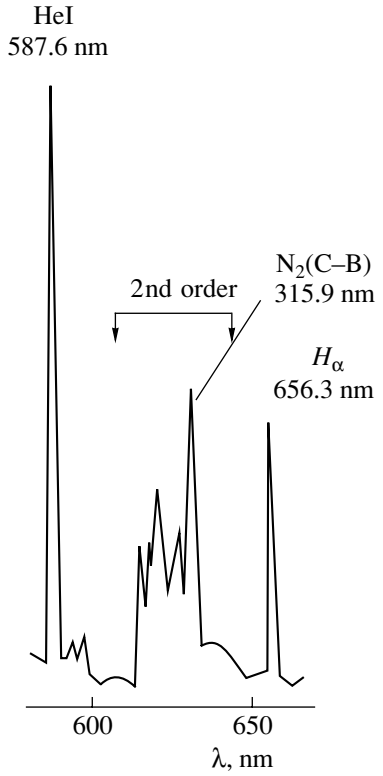

Fig. 1. A fragment of the emission spectrum of a transverse volume discharge in a He–air–H_2O mixture.

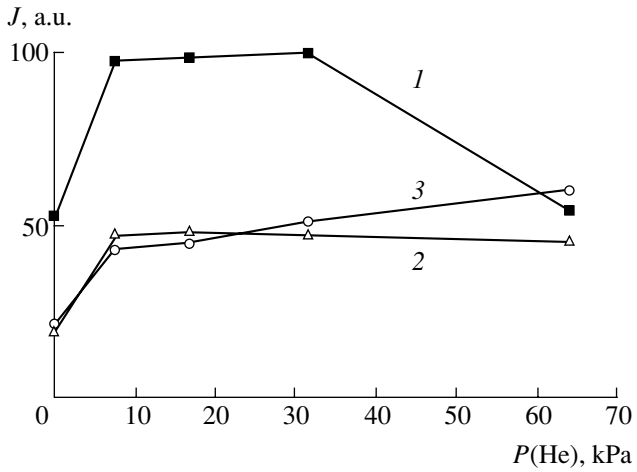

Fig. 2. Plots of the intensity of emission bands at (*1*) 309.7 nm, (*2*) 315.9 nm N_2(C–B)(0–1), and (*3*) 337.1 nm N_2(C–B)(0–0) versus partial pressure of helium *P*(He) in the plasma of a transverse volume discharge (U_{ch} = 10 kV) in a He–air–H_2O mixture.

to the emission from cluster molecules formed in the discharge plasma from OH* radicals (of the OH_2^* dipole type), the emission from which can be expected to shift toward longwave region relative to the OH(A–X) band.

Figure 2 shows the results of optimization of the total intensity of emission in the 307–313 nm interval and the characteristic UV bands of the nitrogen molecule depending on the partial pressure of helium for a transverse volume discharge in the He–air–H_2O mixture. For U_{ch} = 10 kV, the optimum partial pressure of helium in the mixture is 10–40 kPa. The intensity of emission bands in the 307–313 nm interval is approximately two times that of the bands due to N_2(C–B) at 337.1 and 315.9 nm. For *P*(He) ≥ 40 kPa, the emission intensity of the band at λ = 337.1 nm slightly increased, while that of the band at 315.9 nm was almost independent of *P*(He) in the 10–60 kPa range. When the partial pressure of He was increased from 0 to 10 kPa, the intensity of all emission bands increased by a factor of 2.0–2.5.

Thus, it was established that the spectrum of emission due to the N_2(C–B) system of nitrogen for the transverse volume discharge in the He–air–H_2O working mixture is supplemented by a system of bands in the 307–313 nm interval, which is related to the presence of water vapor. In order to provide for a maximum intensity of emission within Δλ = 307–313 nm, the partial pressure of helium must fall within 10–40 kPa. For *P*(He) = 60 kPa, the intensities of emission at 337.1, 315.9, and 307–313 nm are equal. Therefore, a working medium based on the He–air–H_2O mixture can be used in pulsed-periodic UV radiation sources with dominating emission in the 307–313 nm wavelength interval. Such UV sources can be employed for the purposes of laser photometry, microelectronics, and high-energy chemistry.

REFERENCES

1. F. A. Ermalitskiĭ and I. E. Zalesskiĭ, Zh. Prikl. Spektrosk. **38** (4), 550 (1983).
2. A. Ya. Vul', S. V. Kidalov, V. M. Milenin, *et al.*, Pis'ma Zh. Tekh. Fiz. **25** (8), 62 (1999) [Tech. Phys. Lett. **25**, 321 (1999)].
3. O. K. Shuaibov, L. L. Shimon, I. V. Shevera, and A. J. Minja, J. Phys. Stud. **3** (2), 157 (1999).
4. A. K. Shuaibov, Pis'ma Zh. Tekh. Fiz. **26** (9), 1 (2000) [Tech. Phys. Lett. **26**, 357 (2000)].
5. A. K. Shuaibov, L. L. Shimon, A. I. Dashchenko, and I. V. Shevera, Zh. Tekh. Fiz. **71** (2), 77 (2001) [Tech. Phys. **46**, 207 (2001)].
6. L. Wallace, Astrophys. J., Suppl. Ser. **7**, 245 (1962).
7. R. W. B. Pearse and A. G. Gaydon, *The Identification of Molecular Spectra* (Chapman and Hall, London, 1963).

Translated by P. Pozdeev

Technical Physics Letters, Vol. 27, No. 12, 2001, pp. 1026–1027. Translated from Pis'ma v Zhurnal Tekhnicheskoĭ Fiziki, Vol. 27, No. 24, 2001, pp. 1–5.

Low-Temperature Internal Friction in an Aluminum–Aluminum Oxide Fiber Composite

A. N. Kachevskiĭ

Novorossiysk State Naval Academy, Novorossiysk, Russia

Received July 19, 2001

Abstract—The temperature dependence of the internal friction during bending oscillations in an aluminum–aluminum oxide fiber composite exhibits sharp unstable peaks of damped mechanical oscillations, apparently, of a nonrelaxation nature. © *2001 MAIK "Nauka/Interperiodica".*

Solving a fundamental problem concerning the mechanisms of relaxation phenomena in materials with noncoherent interphase boundaries is important for both the theory and practice of the internal friction method, as well as for the investigation of real structures of various heterophase composite materials, including construction composites, metal–insulator–semiconductor heterostructures for electronics, etc. [1–4]. According to a generalized classification [5], a composite material representing aluminum reinforced by continuous aluminum oxide fibers is characterized by the so-called "oxide binding" of components. We have studied the binding of components in such composites by the method of internal friction with a view to evaluating the structural instability of these materials.

An aluminum–aluminum oxide fiber ($Al–Al_2O_3$) composite obtained by the method of vacuum compression impregnation contained virtually no shrinkage voids, hot cracks, or nonimpregnated regions between fibers (Fig. 1). The bulk fraction of aluminum oxide fibers in the composite was 45% at an average fiber diameter of 14 μm. The internal friction in the composite samples was measured by the mechanical coupling and the inverse torsion pendulum techniques [1, 2]. The internal friction measurements were performed in the amplitude-independent spectral range on heating the samples from liquid nitrogen temperature. It was assumed that the relative variation of the dynamic elasticity (storage) modulus E/E_0 was equal to a relative change in the square intrinsic oscillation frequency of the sample f^2/f_0^2 (where f_0 is the room-temperature intrinsic oscillation frequency).

Figure 2 shows some results on the temperature dependence of the internal friction and E/E_0 values determined by the mechanical coupling method for bending oscillations. The internal friction peak at 120 K was previously identified as due to the Bordoni effect in the composite matrix deformed under the action of thermal stresses. It was established that, irrespective of the type of binding at the interphase boundaries (we studied Al–B, Al–C, Al–SiC, and $Al–Al_2O_3$ fiber-reinforced composites, as well as the Al composites with SiC and CaCl filaments, this series including virtually all types of binding according to Metcalf [5]), the Bordoni dislocation relaxation is an inherent low-temperature property of all composites based on aluminum alloys [4, 6–9]. It was also found that thermal stresses play a determining role in the formation and behavior of the Bordoni thermal friction peak observed in the $Al–Al_2O_3$ fiber composites studied.

In addition to the Bordoni peak, the temperature dependence of the internal friction for bending oscillations in $Al–Al_2O_3$ fiber composites display sharp and unstable peaks of damped mechanical oscillations, apparently, of a nonrelaxation nature (Fig. 2). The temperature positions and heights of these peaks significantly depend on the thermal prehistory of a sample, including the number of thermal cycles, while being weakly affected by the amplitude of deformation oscillations. This behavior is somewhat analogous to a nonrelaxation internal friction peak observed for the torsion oscillations in Al–SiC filament composites [9]. On the other hand, the two cases differ in the type of

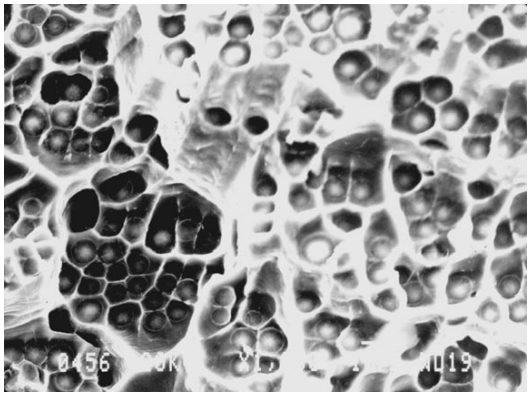

Fig. 1. A typical image of the fracture surface of an $Al–Al_2O_3$ fiber composite.

1063-7850/01/2712-1026$21.00 © 2001 MAIK "Nauka/Interperiodica"

dynamic loading and the oscillation frequency. Indeed, the effect is not observed for the torsion oscillations in Al–Al_2O_3 fiber composites, although the Bordoni effect still takes place at 90 K.

An analysis of the aforementioned features experimentally observed for the nonrelaxation internal friction peaks in Al–Al_2O_3 fiber composites, in combination with some other data, allowed us to suggest that the latter peaks are related to microcracks formed at the interphase boundaries and are damped by a mechanism of the resonance loss type. This dynamic behavior of the cracks in fiber-reinforced composite materials was theoretically predicted by Awal *et al.* in [10], where it was demonstrated that, depending on the crack geometry and mutual arrangement in a composite, the frequency dependence (spectrum) of oscillations may exhibit several resonances. Apparently, the interaction of the elastic stress concentrator fields (reinforcing phase) with the elastic fields of dislocation pileups in the metal matrix at the crack vertex in the applied field of alternating stresses leads to the elementary microcrack opening–closing events and the resonance dissipation of the oscillation energy.

The role of thermal stresses in the matrix consists in providing conditions for the resonance behavior: these stresses should be minimum and comparable in magnitude with the stresses excited in the composite material in the course of internal friction measurements. This role of thermal stresses is confirmed by a change in the temperature positions of the nonresonance peaks observed in the course of thermal cycling. The presence of a distribution of microcracks with respect to size, shape, and mobility leads to the appearance of several resonance peaks.

It was of interest to estimate the size of microcracks at the interphase boundaries in the Al–Al_2O_3 fiber composites studied. Following Kelly [11] and using data on the crack propagation resistance (G_c = 40 J/m^2, K_c = 14 kgf/mm$^{3/2}$ [11]) and the Al– Al_2O_3 interface strength in the composite (σ = 9.1 kgf/mm^2, E = 93GPa), we obtain I = 0.15–0.8 mm.

As noted above, only fiber-reinforced composites with the oxide type binding of components exhibit sharp internal friction peaks. No inelastic effects of this kind are observed in materials with the component binding of other types (including mixed types such as in Al–B fiber composites, where both oxide and reactive binding take place). Therefore, the oxide binding of components in fiber-reinforced composites can be determined by the internal friction method. This will provide important data on the mechanism of binding. However, this approach requires certain additional data, in particular, on the physical nature of peaks in the internal friction spectra and the relationship between peak parameters and adhesion characteristics. These are the tasks for subsequent investigations.

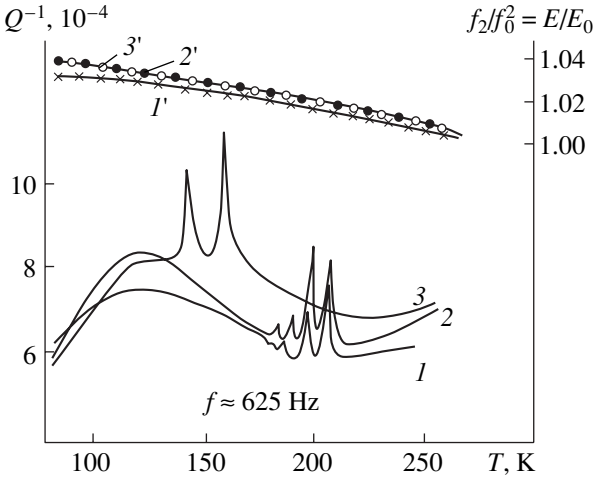

Fig. 2. Temperature variation of (*1*–*3*) the internal friction and (*1*'-*3*') storage modulus of an Al–Al_2O_3 fiber composite measured on heating from liquid nitrogen temperature in three sequential thermal cycles.

REFERENCES

1. V. S. Postnikov, *Internal Friction in Metals* (Metallurgiya, Moscow, 1974).
2. M. S. Blanter, Yu. V. Piguzov, and G. M. Ashmarin, *Method of Internal Friction in Physical Metallurgy Investigations* (Metallurgiya, Moscow, 1991).
3. V. P. Levin and V. B. Proskurin, *Dislocation Inelasticity in Metals* (Nauka, Moscow, 1993).
4. A. N. Kachevskiĭ, Author's Abstract of Doctoral Dissertation in Technical Sciences (IMET RAN, Moscow, 1992).
5. *Composite Materials*, Vol. 1: *Interfaces in Metal Matrix*, Ed. by A. Metcalfe (Academic, New York, 1974; Mir, Moscow, 1978).
6. A. N. Kachevskiĭ, Dokl. Akad. Nauk SSSR **323** (1), 78 (1992) [Sov. Phys. Dokl. **37**, 157 (1992)].
7. V. S. Postnikov, S. A. Ammer, and A. N. Kachevskiĭ, Pis'ma Zh. Tekh. Fiz. **5** (9), 560 (1979) [Sov. Tech. Phys. Lett. **5**, 229 (1979)].
8. A. N. Kachevsky and M. Kh. Shorshorov, Mater. Charact., No. 3, 177 (1991).
9. A. N. Kachevskiĭ, M. Kh. Shorshorov, and V. P. Alekhin, Dokl. Akad. Nauk SSSR **315** (6), 1377 (1990) [Sov. Phys. Dokl. **35**, 1083 (1990)].
10. M. A. Awal, T. Kundu, and S. P. Joshi, Eng. Fract. Mech. **33** (5), 753 (1989).
11. A. Kelly, *Strong Solids* (Oxford Univ. Press, London, 1971; Mir, Moscow, 1978).

Translated by P. Pozdeev

Technical Physics Letters, Vol. 27, No. 12, 2001, pp. 1028–1029. Translated from Pis'ma v Zhurnal Tekhnicheskoĭ Fiziki, Vol. 27, No. 24, 2001, pp. 6–10.

Vircator Radiation Controlled by Axial Current-Carrying Filament

A. E. Dubinov[a,*], V. D. Selemir[a], and V. P. Tarakanov[b]

[a] *Institute of Experimental Physics, Russian Federal Nuclear Center, Sarov, Russia*

[b] *Associated Institute for High Temperatures, Russian Academy of Sciences, Moscow, Russia*

* *e-mail: dubinov@ntc.vniief.ru*

Received May 21, 2001; in final form, July 26, 2001

Abstract—The operation of a vircator system with an axial current-carrying filament was studied by computer modeling. It is demonstrated that, by correctly selecting the value of current in the filament, the electron beam dynamics can be controlled so as to excite the output feeder in an optimum regime, which provides for a fourfold increase in the output power. *© 2001 MAIK "Nauka/Interperiodica".*

Previously [1], we proposed to increase the efficiency of a microwave generator with virtual cathode (VC)—vircator—by using the azimuthal magnetic field of an axial current-carrying filament (see also [2, 3]). The proposal was based on the idea of ensuring the cyclotron rotation of slow electrons in the VC at a frequency equal to that of electron oscillations in the cathode–VC potential well by adjusting the magnitude of current in the filament. However, this vircator configuration was neither experimentally implemented nor theoretically studied.

Below, we present the results of a two-dimensional computer modeling of the operation of a vircator with an axial current-carrying filament. For this purpose, we used the well-known fully self-consistent relativistic electromagnetic PIC code KARAT (version 80-007 win-rz) described in [4], employing the particle-in-cell (PIC) variant of the large particle method.

The proposed vircator geometry is depicted in Fig. 1. The vircator contains a hollow conducting coaxial cathode with the outer and inner diameters of 3 and 2 cm, respectively. The anode electrode represents a combination of two cylinders with the diameters 6 cm (in the diode and drift region) and 10 cm (radiation output region). Arranged inside the latter anode part is a cylindrical collector 6 cm in diameter. The anode and collector form a coaxial feeder with a wave impedance of ~30 Ω.

Spaced 1 cm from the cathode edge is an anode grid fully transparent for electrons. The axial current-carrying filament with a diameter of 2 mm passes through a window at the grid center. The total length of the drift region from anode grid to the collector front edge is 7 cm. In our study, the axial current-carrying filament was modeled by setting a stationary external azimuthally oriented magnetic field B_θ decaying at the current-carrying filament surface according to the r^{-1} law.

The anode and collector were grounded and a rectangular voltage pulse with an amplitude of –120 V and a duration of 5 ns was applied to the cathode. The computer program calculated evolution of the electromagnetic field at the right-hand end of the output feeder. Calculations performed for various values of the magnetic field strength B_θ showed that the microwave radiation frequency is about 3 GHz and varies but weakly with the B_θ value. The program also calculated evolution of the Poynting vector flux at the feeder end, by which the pulse-average output radiation power was determined.

Figure 2 shows a typical model oscillogram of the output microwave radiation power. It was found that, in contrast to the frequency, the pulse-average output radiation power significantly depends on the azimuthal magnetic field strength. Figure 3 presents a plot of the output microwave radiation power versus magnetic field strength. Positive B_θ values corresponds to the current direction coinciding with that of the electron beam

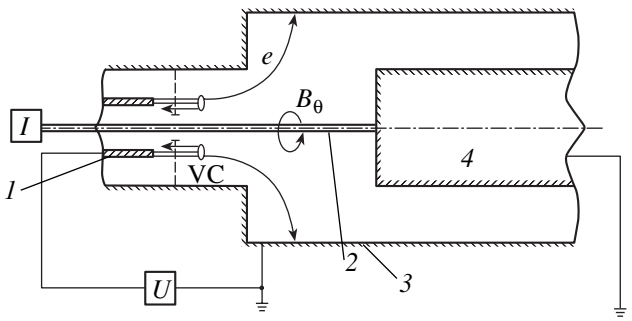

Fig. 1. A schematic diagram of the model vircator: (*1*) cathode; (*2*) current-carrying filament; (*3*) anode; (*4*) collector; (VC) virtual cathode; (*I*) current source; (*U*) pulsed voltage generator. Arrows indicate the directions of electron motion.

1063-7850/01/2712-1028$21.00 © 2001 MAIK "Nauka/Interperiodica"

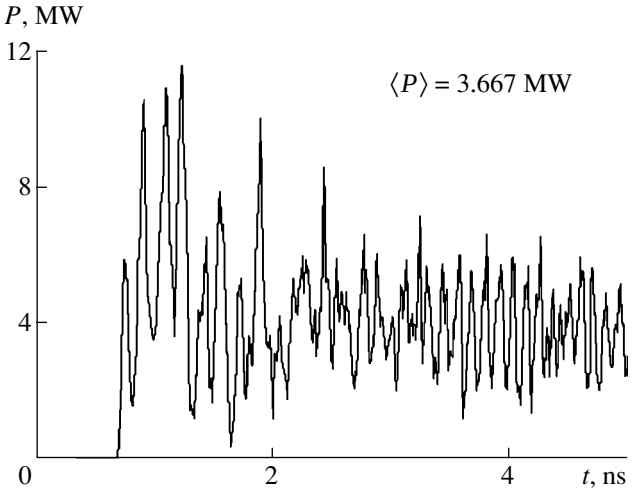

Fig. 2. A typical model oscillogram of the output microwave radiation power ($\langle P \rangle$ is the pulse-average output radiation power).

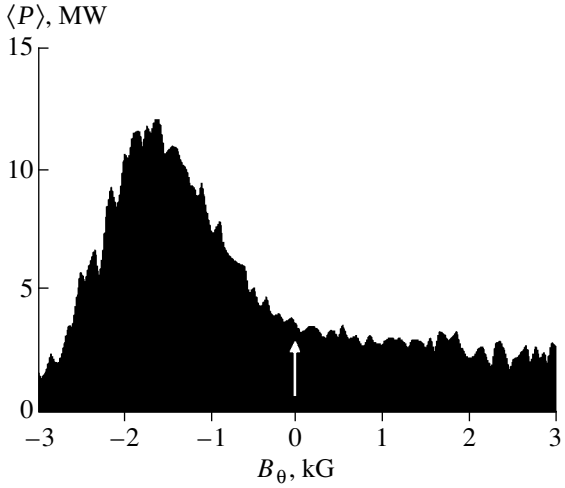

Fig. 3. A plot of the output microwave radiation power versus azimuthal magnetic field strength for the vircator with an axial current-carrying filament (arrow indicates the $\langle P \rangle$ value for a usual vircator without such filament).

propagation in the diode (favoring the beam pinching); negative B_θ values correspond to the opposite current direction and lead to defocusing of the electron beam.

An analysis of the data presented in Fig. 3 showed that the role of the cyclotron resonance, even if this takes place, is rather insignificant. A more important factor is a particular site where the flying electrons are absorbed. Indeed, for positive B_θ, the electrons are absorbed on the collector and the output power is virtually independent on the magnetic field strength. For $B_\theta < -2$ kG, the electrons strike the anode cylinder of smaller diameter and, hence, the output radiation power is as small as in the previous case. However, should the electrons strike the anode cylinder of large diameter (as indicated by arrows in Fig. 1), the output feeder excitation becomes more effective and the output power exhibits growth—nearly fourfold at $B_\theta = -1.6$ kG (Fig. 3).

As is known, the electron beam current in a vircator is modulated in amplitude, which implies that the coaxial feeder in the optimum regime is excited by a modulated radial electron beam. Thus, by correctly selecting the current in the axial filament, it is possible to provide for an optimum beam dynamics in the vircator and ensure the optimum output feeder excitation.

REFERENCES

1. A. E. Dubinov and V. D. Selemir, RF Patent No. 2068596, H 01 J 25/68 (1991), Byull. Izobret., No. 30 (1996).
2. A. I. Pavlovskiĭ, V. S. Bosamykin, V. D. Selemir, *et al.*, in *Relativistic High-Frequency Electronics* (Inst. Prikl. Fiz. Akad. Nauk, Nizhni Novgorod, 1992), Vol. 7, p. 81.
3. B. V. Alyokhin, A. E. Dubinov, V. D. Selemir, *et al.*, IEEE Trans. Plasma Sci. **22** (5), 945 (1994).
4. V. P. Tarakanov, *User's Manual for Code Karat* (Berkley Research Associate Inc., Springfield, 1992).

Translated by P. Pozdeev

Technical Physics Letters, Vol. 27, No. 12, 2001, pp. 1030–1031. Translated from Pis'ma v Zhurnal Tekhnicheskoĭ Fiziki, Vol. 27, No. 24, 2001, pp. 11–15.

Laser Rockets

R. A. Liukonen

Vavilov Optical Institute, State Scientific Center of the Russian Federation, St. Petersburg, 190164 Russia
e-mail: liukonen@soi.spb.ru

Received June 26, 2001

Abstract—The results of experimental and theoretical investigations of the dynamic characteristics of a laser rocket in the initial flight path segment are presented. The energy to a laser jet propulsor was delivered with the beam of a CO- or CO_2-pulsed laser with a pulse energy ranging from 0.1 to 3.0 kJ at a repetition frequency of 100 Hz. © *2001 MAIK "Nauka/Interperiodica".*

In recent years, the interest of researchers in the problem of accelerating bodies in the atmosphere and space with the aid of lasers has been permanently increasing, especially after our first communications [1, 2] demonstrating that prospects for the creation of laser rockets have firm ground. This was confirmed by the SPIE Symposium on lasers held in 2000 in Santa Fe, where about ten reports were devoted to this subject (see, e.g., [3–6]).

Below, we report on the results of experimental and theoretical investigations of the dynamic characteristics of laser rockets (LRs) with a mass of 0.1–5.0 kg driven by laser beams with an average power from 10 to 300 kW.

Figure 1 shows a prototype laser rocket without jet nozzle and two types of a laser jet propulsor (LJP). Placed in a jet nozzle, the LJP generates a reactive recoil impulse when a plasma is initiated on the propulsor surface as a result of the optical discharge in the laser-ablated material or at the focal points of a parabolic matrix. In our experiments, the plasma was generated by a pulsed radiation of CO or CO_2 laser acting upon various gases and materials, ranging from air to a high-efficiency material known as "slavit" [8]. The laser rockets were launched either vertically or at an angle of 30° to the horizon with a forced trajectory stabilization.

In addition, a special theoretical model was developed for calculating the laser rocket trajectory in the initial flight path segment. The model system of equations, derived using the laws of mass, momentum, and energy conservation, relates the laser radiation parameters to the plasma characteristics and provides for the use of experimental data in the calculations:

$$\Delta V = I(t)\tau S/M(t)[(1 + R)/c + v_p\eta(1 - R)] \text{ [m/s]}, \quad (1)$$

$$f_{\min} = Mg/C_m W \text{ [s}^{-1}\text{]}, \quad (2)$$

$$V_{\max} = tC_m fW/M \text{ [m/s]}. \quad (3)$$

Here, Eq. (1) describes an increment of the laser rocket velocity due to a single laser pulse with the energy $W = I\tau S$ (I is the laser beam intensity, τ is the laser pulse duration, and S is the ablator surface area). The first term in this equation determines the light pressure momentum and the second term describes the reactive recoil impulse corresponding to the plasma jet velocity v_p in the nozzle with an energy equivalent η of the laser-ablated mass. For the substances used in the experiment, this parameter was experimentally determined for a laser beam energy density ranging from 2 to 20 J/cm^2.

Figure 2 shows typical experimental data on the parameter η and the plasma jet velocity v_p studied as functions of the specific delivered laser energy for an LJP using a poly(methyl methacrylate) ablator (fuel).

The second equation in the model system allows a minimum laser pulse repetition rate [7] to be determined that is necessary for overcoming the earth gravity for an LJP with a mass M for a given specific reac-

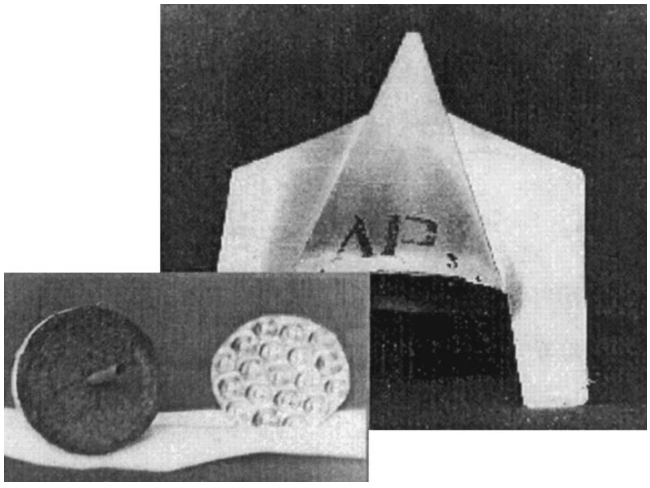

Fig. 1. Prototype laser rocket and laser jet propulsors.

1063-7850/01/2712-1030$21.00

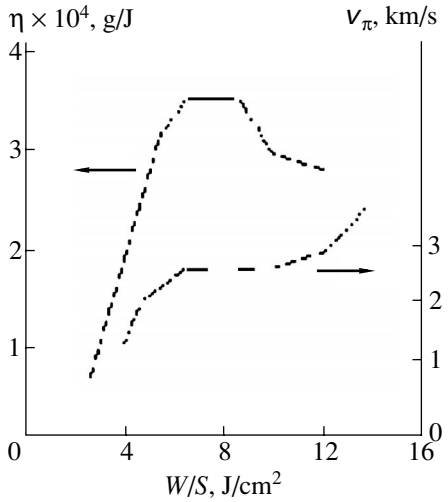

Fig. 2. Experimental data on the mass energy equivalent η and the plasma jet velocity v_p studied as functions of the specific delivered laser energy for an LJP using a poly(methyl methacrylate) ablator.

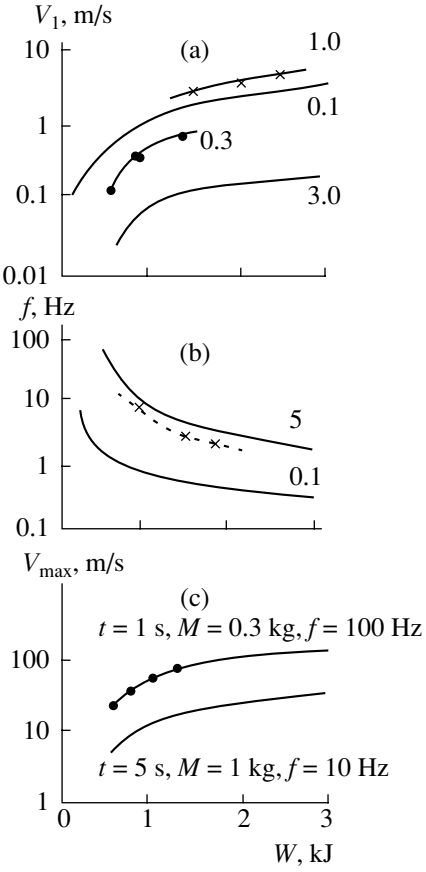

Fig. 3. Plots of the dynamic characteristics of a laser rocket versus laser beam power for various projectile masses in the vertical launch: (a) projectile velocity increment per laser pulse; (b) minimum laser pulse repetition rate sufficient to overcome the earth gravity; (c) maximum laser rocket velocity attained within 1 and 5 s for a laser pulse repetition rate of 10 and 100 Hz, respectively. Dots and crosses refer to the experimental data for the air plasma and slavit-3 ablator, respectively; solid curves show the results of model calculations by Eqs. (1)–(3).

tive recoil impulse C_m that was either calculated or experimentally measured [8].

Using the third model equation, it is possible to calculate the maximum velocity of a flying vehicle attained within the time t for various values of the average laser beam power (without an allowance for the atmospheric drag).

Figure 3 presents a comparison between theoretical results and experimental data for the air plasma and slavit-3 ablators. Figures at the curves indicate the mass of accelerated projectiles in kilograms. As can be seen from these data, the maximum reactive thrust force for single pulses (observed in the experiments using slavit-3 as the laser-ablated fuel) amounted to 4.8×10^5 (dyn s), and the maximum acceleration achieved for the vertical launching was 5.0×10^3 m/s^2 (~500g).

Acknowledgments. The author is grateful to the managing staff of the Research and Production Corporation "Astrofizika" and the State Laser Research and Testing Center "Raduga" for financial and technical support in experiments with a pulsed-periodic CO_2 laser radiation.

REFERENCES

1. R. A. Liukonen, I. K. Babaev, N. D. Belkin, *et al.*, in *Technical Digest of the 8th Laser Optics Conference, St. Petersburg, 1995*, Vol. 1, p. 260.
2. R. A. Liukonen, in *Proceedings of SPIE XII International Symposium on Gas Flow and Chemical Lasers and High-Power Laser Conference, St. Petersburg, 1998*, Proc. SPIE **3574**, 470 (1998).
3. S. Uchida, K. Imasaki, X. Zhou, *et al.*, in *Proceedings of SPIE International Symposium on High-Power Laser Ablation III, Santa Fe, USA, 2000*, Proc. SPIE **4065**, 495 (2000).
4. C. R. Phipps, J. P. Reilly, and J. W. Campbell, in *Proceedings of SPIE International Symposium on High-Power Laser Ablation III, Santa Fe, USA, 2000*, Proc. SPIE **4065**, 502 (2000).
5. L. Berthe, A. Sollier, P. Peure, *et al.*, in *Proceedings of SPIE International Symposium on High-Power Laser Ablation III, Santa Fe, USA, 2000*, Proc. SPIE **4065**, 511 (2000).
6. E. McKenzie, A. Forbes, G. R. Turner, *et al.*, in *Proceedings of SPIE International Symposium on High-Power Laser Ablation III, Santa Fe, USA, 2000*, Proc. SPIE **4065**, 860 (2000).
7. C. R. Phipps and M. M. Michaelis, Laser Part. Beams **12**, 23 (1994).
8. R. A. Liukonen and A. M. Trofimenko, Pis'ma Zh. Tekh. Fiz. **18** (7), 76 (1992) [Sov. Tech. Phys. Lett. **18**, 235 (1992)].

Translated by P. Pozdeev

Technical Physics Letters, Vol. 27, No. 12, 2001, pp. 1032–1034. Translated from Pis'ma v Zhurnal Tekhnicheskoĭ Fiziki, Vol. 27, No. 24, 2001, pp. 16–21.

Ferroelectric (Ba,Sr)TiO_3 Thin-Film 60-GHz Phase Shifter

A. B. Kozyrev, A. V. Ivanov, O. I. Soldatenkov, A. V. Tumarkin, S. V. Razumov, and S. Yu. Aigunova

St. Petersburg State Electrotechnical University, St. Petersburg, Russia

e-mail: mcl@eltech.ru

Received May 24, 2001; in final form, July 24, 2001

Abstract—The design and microwave characteristics of an integral ferroelectric $Ba_{0.3}Sr_{0.7}TiO_3$ thin-film microwave phase shifter operating in the millimeter wavelength range ($f \sim 60$ GHz) are reported. In this frequency range, the device introduces a loss of $S_{21} = -10$ dB and allows a continuous phase shift in the interval from zero to 220 deg with a small phase error (not exceeding ±5 deg). © *2001 MAIK "Nauka/Interperiodica".*

Previous investigations [1, 2] showed good prospects for the use of thin ferroelectric films in tunable microwave devices. These materials offer a number of advantages over semiconductor and ferrite based microwave elements. In particular, it was found that the nonlinear properties of thin ferroelectric films can be successfully employed in phase shifters for the microwave range, operating at frequencies up to 30 GHz [1, 2]. In addition, it was established that ferroelectric films ensure a high operation speed in response to unipolar voltage pulses; moreover, these materials can operate at elevated microwave power levels without significant degradation in dielectric properties [3, 4]. An important additional factor is the relatively low cost of manufacturing ferroelectric thin-film components for microwave devices.

Unfortunately, virtually no information is available on the properties of thin ferroelectric films at 30–60 GHz, and almost no data on the related device characteristics in this frequency range were reported. Johnson *et al.* [5] investigated the dispersion of permittivity ε of bulk $Ba_{0.27}Sr_{0.73}TiO_3$ at frequencies above 50 GHz; the reported behavior showed evidence of a decrease in tunability and increase in insertion losses, which must negatively influence the characteristics of tunable microwave devices.

The purpose of our study was to create a microwave phase shifter capable of operating at a frequency of 60 GHz based on a thin ferroelectric (Ba,Sr)TiO_3 film and to estimate the effect of ε dispersion on the device characteristics.

Ferroelectric $Ba_{0.3}Sr_{0.7}TiO_3$ film technology and microwave phase shifter topology. Thin ferroelectric films were prepared in a Leybold Z-400 setup by ion-plasma RF magnetron on-axis sputtering of a $Ba_{0.3}Sr_{0.7}TiO_3$ ceramic target with a diameter of 76 mm. This target composition was established to be optimum from the standpoint of obtaining sputtered films with best characteristics for microwave applications [6]. The films were deposited onto alumina (Al_2O_3 ceramics) substrates in a pure oxygen atmosphere at a pressure of ~10 Pa and a substrate temperature of 905°C. After deposition, the films were allowed to cool in pure oxygen at a rate of 2–3 K/min. Then, the $Ba_{0.3}Sr_{0.7}TiO_3$ film surface was covered with a layer of copper deposited by thermal evaporation in vacuum. The microwave phase shifter topology was formed by chemical etching.

The phase shifter topology is depicted in Fig. 1 together with a detailed structure of the resonance *LC* circuit unit and an equivalent scheme of the ferroelectric microwave phase shifter. The phase shifter is based on a 125-μm-thick alumina substrate bearing an ~0.7-μm-thick $Ba_{0.3}Sr_{0.7}TiO_3$ film and an ~1-μm-thick copper metallization layer. The microstrip line with a characteristic impedance of $z_0 = 50\ \Omega$ is loaded with a periodic structure of 20 parallel *LC* circuits. Each *LC* circuit comprises inductance *L* connected in parallel with capacitance *C*, the inductance representing a rectangular open circuit shunt microstrip stub with a length exceeding λ/4 and the capacitance being determined by a gap between the microstrip line and the radial λ/4 stub. The radial λ/4 stub ensures shortening of the capacitive gap in response to the microwave signal. A dc control voltage is applied to the capacitive gap between the microstrip line and the radial λ/4 stubs linked by narrow (30 μm) microstrip lines to a contact pad to which a dc voltage source is connected.

Microwave characteristics of the ferroelectric phase shifter. The experimental characteristics of the ferroelectric thin-film microwave phase shifter described above are presented in Fig. 2. The measurements were performed with the aid of waveguide-strip junctions possessing the following loss characteristics in the 55.5–65.5 GHz frequency interval: $S_{21} = -3$ dB and $S_{11} = -(7–10)$ dB. These junction parameters, taken into account in studying the phase shifter characteris-

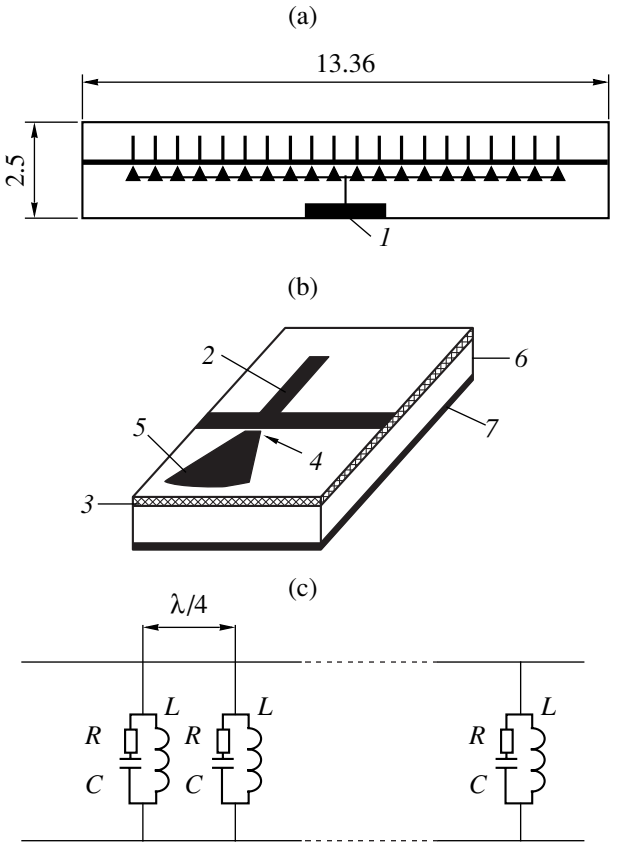

Fig. 1. Schematic diagrams showing (a) general topology, (b) detailed *LC* circuit structure, and (c) equivalent scheme of a ferroelectric $Ba_{0.3}Sr_{0.7}TiO_3$ thin-film microwave phase shifter based on a microstrip line: (*1*) contact pad for the dc control voltage application; (*2*) rectangular microstrip stub determining inductance *L*; (*3*) barium strontium titanate film; (*4*) capacitive gap determining capacitance *C*; (*5*) radial microstrip λ/4 stub; (*6*) Al_2O_3 substrate; (*7*) copper metallization layer (figures indicate dimensions in millimeters).

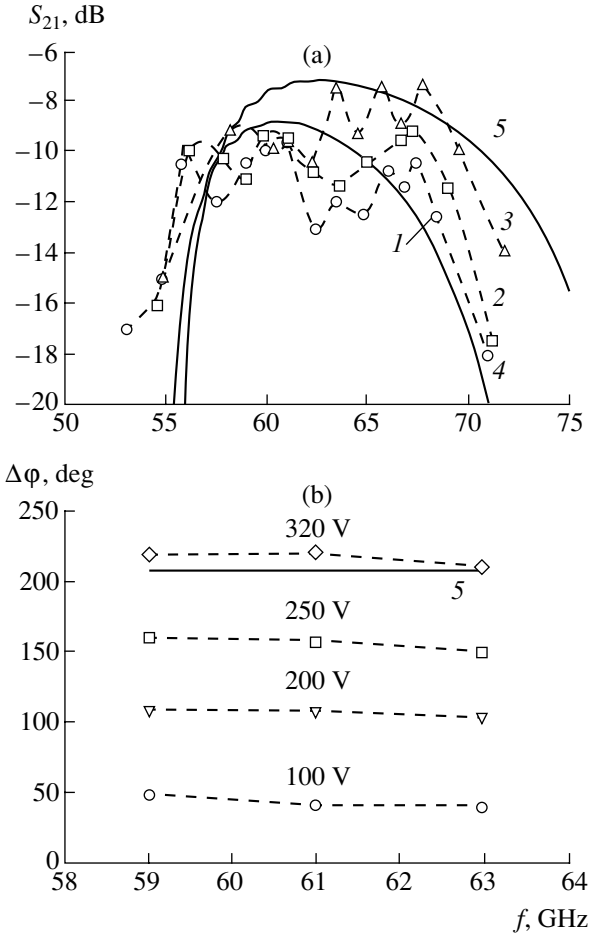

Fig. 2. Experimental characteristics of a ferroelectric microwave phase shifter (dashed curves): (a) transmission coefficient versus frequency measured at a control voltage of U = 0 (*1*), 200 (*2*), and 320 V (*3*); (b) phase shift variation measured at a control voltage indicated at the curves. Solid curves show the results of the phase shifter simulations for $\tan\delta$ = 0.12 and C = 0.0375 (*4*) and 0.022 pF (*5*).

tics, were the main factors determining uncertainty of the measurements.

The ferroelectric thin-film phase shifter was characterized by a microwave signal damping of $S_{21} \sim -10$ dB near $f \sim 60$ GHz with a weak variation of the transmission coefficient (±0.5 dB) on applying a dc voltage of up to 320 V to the capacitive ferroelectric gaps. The microwave signal phase shift in response to this control dc voltage was $\Delta\varphi = 220$ deg at a phase uncertainty not exceeding ±5 deg in the 59–63 GHz frequency interval for all values of the control voltage. The reflection coefficient (S_{11}) of the phase shifter in the 59.7–62 GHz band was not worse than –5.5 dB and remained virtually unchanged upon application of the control voltage. Thus, the phase shifter was characterized by a figure of merit of $F(60\ \text{GHz}) = \Delta\varphi/S_{21} = 22$ deg/dB.

Besides the experimental plots, Fig. 2 shows the calculated functions $S_{21}(f)$ and $\Delta\varphi(f)$ (curves *4* and *5*, respectively). The calculations were performed using equivalent schemes of the microstrip elements. The capacitive gaps were modeled by serially connected capacitance C and resistance R with an allowance for the dielectric losses ($\tan\delta$) in the ferroelectric film. The microwave properties of the ferroelectric films were described by extrapolating the virtually linear dispersion law for $\tan\delta$ (previously determined for the films in the 1–30 GHZ frequency range [7]) up to a 60 GHz region. The value of dielectric losses used in the model was $\tan\delta\,(U = 0) = 0.12$. The calculation was performed assuming the absence of frequency dispersion of the permittivity and using the controllability factor K = 1.7 characteristic of the films studied at lower frequencies [6].

As can be seen from Fig. 2, the calculated curves are in a good agreement with the experimental data.

Because of the uncertainty of results obtained in recalculating the phase shifter parameters to the properties of ferroelectric films, the question as to whether the dispersion of ε is manifested in the $Ba_{0.3}Sr_{0.7}TiO_3$ films studied remains open. However, we may conclude that this effect, even if present, does not hinder the possibility of creating a sufficiently effective devices based on the ferroelectric films operative at frequencies up to 60 GHz.

Conclusion. We have considered the design and microwave characteristics of an integral ferroelectric phase shifter capable of controlling the phase of a signal in the millimeter wavelength range. To our knowledge, this is the first demonstration of the possibility of using ferroelectric microwave phase shifters and the ferroelectric thin-film technology in this frequency band. The proposed phase shifter showed a figure of merit of 22 deg/dB at a maximum phase shift of $\Delta\varphi$ = 220 deg at frequencies near 60 GHz.

REFERENCES

1. A. Kozyrev, A. Ivanov, O. Soldatenkov, *et al.*, Pis'ma Zh. Tekh. Fiz. **25** (20), 78 (1999) [Tech. Phys. Lett. **25**, 836 (1999)].
2. C. M. Carlson, T. V. Rivkin, P. A. Parilla, *et al.*, Appl. Phys. Lett. **76** (14), 1920 (2000).
3. A. B. Kozyrev, O. I. Soldatenkov, and A. V. Ivanov, Pis'ma Zh. Tekh. Fiz. **24** (19), 19 (1998) [Tech. Phys. Lett. **24**, 755 (1998)].
4. A. Kozyrev, A. Ivanov, T. Samoilova, *et al.*, J. Appl. Phys. **88** (9), 5334 (2000).
5. D. A. Johnson, K. B. Mallory, R. H. Miller, *et al.*, Proc. IEEE **51**, 332 (1963).
6. S. Razumov, A. Tumarkin, O. Buslov, *et al.*, Integr. Ferroelectr. (2001) (in press).
7. A. Kozyrev, V. Keis, O. Buslov, *et al.*, Integr. Ferroelectr. **34**, 271 (2001).

Translated by P. Pozdeev

Technical Physics Letters, Vol. 27, No. 12, 2001, pp. 1035–1037. Translated from Pis'ma v Zhurnal Tekhnicheskoĭ Fiziki, Vol. 27, No. 24, 2001, pp. 22–28.

An Analysis of the Phase Transitions in Biocompatible $Ca_{10}(PO_4)_6(OH)_2$

N. A. Zakharov

Institute of General and Inorganic Chemistry, Russian Academy of Sciences, Moscow, 117907 Russia

Received April 24, 2001; in final form, July 30, 2001

Abstract—The results of investigations of the physical and chemical properties of calcium hydroxyapatite $Ca_{10}(PO_4)_6(OH)_2$ were summarized with a view to the synthesis and processing of this compound. Based on these data, the effects of steric factors, crystal structure defects, and composition on the phase transitions accompanying the thermal treatment of this substance are analyzed. *© 2001 MAIK "Nauka/Interperiodica".*

Investigation of the properties of calcium hydroxyapatite $Ca_{10}(PO_4)_6(OH)_2$ (CHA), a compound close in composition to the inorganic components of teeth and bone tissues in animals and humans [1], is important from the standpoint of both basic knowledge and practical applications. An important practical task is to develop an effective approach to the synthesis and thermal processing of CHA, which would provide for the obtaining of implants with controlled properties. Taking into account lability of the crystal structure of inorganic compounds in the region of phase transitions, it is interesting to study the phase transitions in CHA as a factor of influence upon the physicochemical properties of this compound. Data on the temperatures corresponding to the phase transitions facilitate development of the synthesis of CHA-based materials with controlled properties and optimization of the corresponding implant technology.

This paper summarizes the results of investigations of the phase transitions in CHA performed by a number of methods employing thermostimulated exoelectron emission (TSEE) [2], thermostimulated depolarization currents (TSDC) [3–5], measurements of the thermal [6], X-ray diffraction [7], dielectric [8], and optical [9] properties, and chemical and thermal analysis [7]. The analysis will be aimed at establishing relationships important for the synthesis and characterization of the CHA-based implants.

The results of CHA characterization by the aforementioned methods (Fig. 1) must be interpreted taking into account the composition and steric factors determining the general character and special features of the crystal structure. The crystal structure of CHA is characterized by the presence of Ca channels and the OH^- dipole groups oriented perpendicularly to the Ca triangles (Fig. 2a) [1]. The structural transition from monoclinic ($P2_1/b$) to hexagonal ($P6_3/m$) phase in the region of $T_3 = 200$°C (Fig. 1) is related [1, 2, 5] to reorientation of the OH^- dipole groups in the channels of Ca^{2+} ions. In the presence of structural defects or foreign phases, the reorientation process is hindered and leads (as suggested in [5]) to an increase in T_3.

Close values of the temperature T_5 of anomalies observed by TSEE (390°C) [2] and TSDC (356°C) [5] correspond to a structural transition related to establishing the opposite polarization directions in the adjacent Ca channels of CHA (Fig. 2b) [1]. The difference between $T_5 = 390$°C determined by TSEE and the value (356°C) provided by TSDC [5] is probably explained

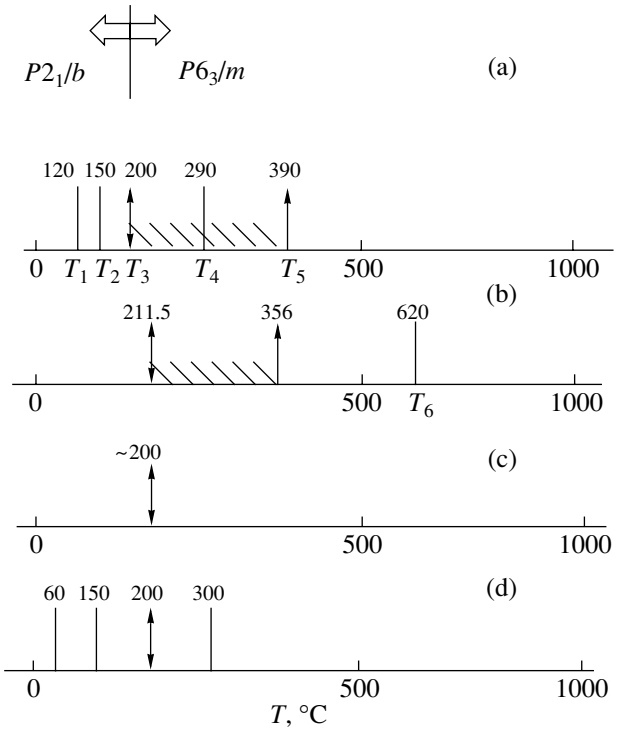

Fig. 1. A summary of special temperatures for CHA according to the data of various methods: (a) TSEE [2]; (b) TSDC [3–5]; (c) thermal properties [6] and X-ray diffraction [7]; (d) dielectric characteristics [8].

1063-7850/01/2712-1035$21.00 © 2001 MAIK "Nauka/Interperiodica"

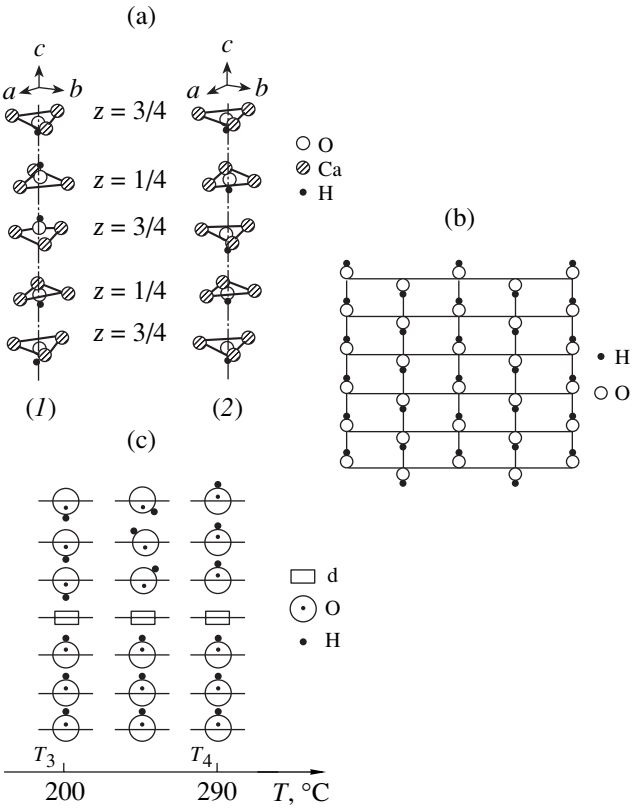

Fig. 2. CHA structure: (a) the orientation of OH^- groups in Ca channels (*1*) before and (*2*) after the structural transition from monoclinic to hexagonal CHA phase at T_3 = 200°C; (b) mutual orientation of the OH^- groups in adjacent Ca channels in the hexagonal CHA phase; (c) the effect of structural defects upon the orientation of OH^- groups in Ca channels before (T_3) and after (T_4) a transition to homogeneous orientation and the sequence of dipole group displacement ("d" indicates defects).

by a difference in composition and defectness of the samples studied and by possible experimental errors.

It must be noted that a TSEE peak observed in the region of T_4 = 290°C (i.e., between the structural transitions in CHA at T_3 and T_5) falls out of the system of special points common for the structural transitions in apatites of the general formula $Me_{10}(XO_4)_6Y_2$ (Me = Ca^{2+}, Sr^{2+}; X = PO_4^{3-}, As_4^{3-}; Y = OH^-, Cl^-) including CHA [2–6]. Taking into account the obvious defectness of CHA, this fact can be explained as follows.

The TSEE peak at 290°C can be attributed to an intermediate structural transition related to the presence of defects hindering the complete orientation of the OH^- groups in the whole Ca channel. Within the framework of this hypothesis, it is naturally suggested that the transition at T_3 = 200°C corresponds to a partial dipole orientation in the channels, whereby the process terminates on the structural defects (Fig. 2c). Overcoming the potential barrier related to the presence of defects in the CHA crystal structure, the dipoles can be completely oriented in the same direction only at a higher temperature (about $T_4 \sim 290$°C). In addition to rotation of the OH^- groups by 180° relative to the initial orientation, the centers of OH^- groups are displaced from the Ca triangle plane in a jumplike manner at T_4. The character of this transition indicates that the T_4 value depends both on the degree of CHA defectness and on the other experimental conditions (e.g., on the heating rate affecting the character of defect distribution).

It should be noted that the TSEE peak at T_4 can be determined not only by the positional ordering of structural units in CHA. Another possible factor is the excitation of emission as a result of the surface recombination of active species (ions, radicals) in an adsorption layer formed on the defective CHA surface [10–12]. A final judgment on this problem requires additional investigations (e.g., of the behavior of the TSEE peaks in the CHA samples subjected to thermal treatment in vacuum).

Outside the temperature interval studied by TSEE [2], there is only one special temperature point T_6, which was observed in the TSDC measurements in apatites [3–5]. For apatites with the compositions $Ca_{10}(PO_4)_6(OH)_2$, $Sr_{10}(PO_4)_6(OH)_2$, $Ca_{10}(PO_4)_6Cl_2$, and $Sr_{10}(AsO_4)_6CO_3$, the corresponding values of T_6 (Fig. 1) are 620, 725, 644, and 573°C, respectively. Based on the aforementioned relationship between the structural transitions on CHA and thermostimulated processes (TSEE, TSTD), we may suggest that a high-temperature transition in common for all the above apatites may exist at a temperature above T_5 (in terms of Fig. 1). This transition may be accompanied by the loss of the ordered arrangement of the OH^- groups in the Ca channels and by violation of the mutual orientation of polarization in the adjacent channels at temperatures above T_6. An analogous situation takes place, for example, in some hydrogen-containing ferroelectrics exhibiting transitions of the order–disorder type [13, 14].

Features of the chemical composition of CHA account for the possibility of topochemical reactions proceeding in the course of the thermal processing. These reactions lead to changes in the object composition [8]. For example, heating stoichiometric CHA above 500°C is accompanied by the formation of a defective phase $Ca_9(HPO_4)(PO_4)_5(OH)$ in the matrix, by decomposition of both defective and stoichiometric compounds according to the reactions [15, 16]

$$Ca_9(HPO_4)(PO_4)_5(OH) = 3Ca_3(PO_4)_2 + H_2O,$$

$$Ca_{10}(PO_4)_6(OH)_2 = 3Ca_3(PO_4)_2 + CaO + H_2O$$

and by the formation of oxoapatite $Ca_{10}(PO_4)_6O$ and vacancies (□) via the reaction [15]

$$Ca_{10}(PO_4)_6(OH)_2 = Ca_{10}(PO_4)_6O\square + H_2O.$$

The appearance of such defects suggests [17, 18] that the anomalies in TSEE and dielectric characteristics observed in the regions of T_1 (120°C), T_2 (150°C), and at 60°C can be related to the adsorption of water, oxygen, OH^- and O^- radicals on the defective CHA structure. Another possibility is that the structurized water and that formed as a result of CHA decomposition may participate in the emission and orientation processes in the alternating electric field. An evidence for this possibility is the shift of anomalies in the dielectric characteristics of CHA toward higher temperatures with increasing frequency of the probing field [8].

The above comparative analysis of the phase transitions and the corresponding physical effects in biocompatible CHA is of interest for technological applications, primarily for selecting the optimum regimes of CHA treatment during synthesis and processing.

REFERENCES

1. A. M. Smolegovskiĭ, in *History of Crystal Chemistry of Phosphates* (Nauka, Moscow, 1986), pp. 47–98.
2. V. P. Orlovskiĭ, N. A. Zakharov, V. A. Klyuev, *et al.*, Neorg. Mater. **31** (8), 1100 (1995).
3. N. Hitmi, C. Lacabanne, and R. A. Young, J. Phys. Chem. Solids **45** (6), 701 (1984).
4. N. Hitmi, C. Lacabanne, Q. Bonel, *et al.*, J. Phys. Chem. Solids **47** (5), 507 (1986).
5. N. Hitmi, C. Lacabanne, and R. A. Young, J. Phys. Chem. Solids **47** (6), 533 (1986).
6. G. L. Sharpataya, A. D. Fedoseev, V. V. Bogacheva, *et al.*, Zh. Neorg. Khim. **40** (4), 612 (1995).
7. H. Suda, M. Yashima, M. Kakihana, *et al.*, J. Phys. Chem. **99**, 6752 (1995).
8. V. P. Orlovskiĭ, N. A. Zakharov, and A. A. Ivanov, Neorg. Mater. **32**, 736 (1996).
9. N. B. van Rees, M. Mengeot, and E. Kostiner, Mater. Res. Bull. **8**, 1307 (1973).
10. I. V. Krylova, *Chemical Electronics (Electronic and Ionic Phenomena Accompanying Physicochemical Conversions on Solid Surfaces)* (Mosk. Gos. Univ., Moscow, 1993).
11. I. V. Krylova, Usp. Khim. **40** (12), 2138 (1976).
12. R. I. Mints, I. I. Mil'man, and V. I. Kryuk, Usp. Fiz. Nauk **119** (4), 749 (1976) [Sov. Phys. Usp. **19**, 697 (1976)].
13. R. Blinc and B. Zeks, *Soft Modes in Ferroelectrics and Antiferroelectrics* (North-Holland, Amsterdam, 1974; Mir, Moscow, 1976).
14. M. E. Lines and A. M. Glass, *Principles and Applications of Ferroelectrics and Related Materials* (Oxford Univ. Press, Oxford, 1977; Mir, Moscow, 1981).
15. J. Zhan, X. Zhanq, J. Chen, *et al.*, J. Mater. Sci.: Mater. Med. **4**, 83 (1993).
16. E. C. M. Driessens, *Bioceramics of Calcium Phosphate*, Ed. by K. de Groot (CRC Press, Boca Raton, 1983).
17. I. V. Krylova, in *Active Solid Surface: Subject Collection* (Akad. Nauk SSSR, Moscow, 1976), pp. 22–34.
18. N. I. Konyshkina and I. V. Krylova, in *Proceedings of the 4th International Symposium on Exoelectron Emission and Dosimetry, Liblice, 1973*, p. 154.

Translated by P. Pozdeev

Technical Physics Letters, Vol. 27, No. 12, 2001, pp. 1038–1040. Translated from Pis'ma v Zhurnal Tekhnicheskoĭ Fiziki, Vol. 27, No. 24, 2001, pp. 29–34.

Microwave Modulated Light Reflection in Semiconductors

M. A. Chernikov and O. A. Ryabushkin

IRE–Polus Group

Fryazino Branch, Institute of Radio Engineering and Electronics, Russian Academy of Sciences, Fryazino, Moscow oblast, Russia

e-mail: roa228@ire216.msk.su

Received July 4, 2001

Abstract—A new contactless modulation spectroscopy method for the investigation of semiconductor structures was experimentally realized. The technique employs the microwave-field-induced heating of free charge carriers in the semiconductor. Acting upon the exciton and acceptor states in a homogeneous GaAs film, the field-heated carriers modify the permittivity spectrum of the semiconductor near the fundamental absorption edge. This change is manifested in the effect of the microwave modulated field on the light reflection from a GaAs samples placed in the field. *© 2001 MAIK "Nauka/Interperiodica".*

The methods employing modulated light reflection [1] offer an effective tool for the investigation and diagnostics of semiconductor materials and heterostructures. Among a number of these techniques, the most widely used is the so-called photoreflectance method [2, 3]. According to this, a semiconductor structure is simultaneously illuminated with a probing light beam of constant intensity, possessing the light quantum energy close to that of the characteristic energy features of the sample, and with an intensity-modulated pumping beam possessing a quantum energy sufficient to excite electrons from the valence band to the conduction band. The nonequilibrium charge carriers generated by the pumping light are redistributed by the built-in electric fields. The charge carrier redistribution at the frequency of modulation of the pumping light leads to modulation of the built-in fields at the same frequency by the induced internal photo-emf.

In semiconductors, the permittivity and the reflection coefficient near the fundamental absorption edge depend on the built-in electric field. Thus, modulation of the pumping light intensity induces modulation of the probing light reflection ΔR. Near the characteristic energy features in the spectrum of the sample studied, the photoreflectance spectrum ($\Delta R/R$) exhibits an oscillatory character. This spectrum may contain information about both free and bound (exciton and impurity) electron states. Using the photoreflectance method, it is possible to study features of the semiconductor energy band structure, measure the built-in electric fields, and (in nanodimensional systems) determine the characteristic quantum confinement energies.

Despite obvious advantages of the photoreflectance measurements (this technique is contactless and requires virtually no special sample preparation), there are certain drawbacks hindering application of this method [3]. The main disadvantage is the presence of a photoluminescence signal (falling within the same spectral range as the photoreflectance response) related to recombination of the pumping-generated nonequilibrium carriers. In the case of measurements on low-dimensional structures, especially at low temperatures, the photoluminescence signal intensity can be several orders of magnitude greater than that of the photoreflectance response. The problem of effective separation of these signals is still incompletely solved.

Previously [4], a method of RF modulated reflectance (RMR) was proposed and realized, which is free of this disadvantage. According to the RMR technique, the light reflection is modulated by a microwave field of variable amplitude. In contrast to the pumping light employed in the photoreflectance method, the energy of the RF quanta is insufficient for the production of new nonequilibrium carriers; hence, photoluminescence does not arise. The RF field interacts with the built-in electric fields in a sample and modifies these fields.

It was also suggested [4] that the light reflection coefficient can be modulated using a microwave field which, acting upon a semiconductor, is capable of effectively changing the distribution of free charge carriers. This modification may lead to an increase in the electron and lattice temperatures and a change in the built-in electric fields, the rate of impact ionization, and the degree of screening of both exciton and impurity states. The modulated optical reflection measurements allow these effects to be studied on a spectroscopic level. However, some experimental difficulties hindered realization of this possibility until now.

Below, we report on the first experimental realization of the method of microwave modulated reflectance (MMR). The measurements were performed on a doped GaAs film with a thickness of $\sim 3 \times 10^{-6}$ m grown by gas phase epitaxy on a 500-μm-thick semi-insulating GaAs substrate. All experiments were performed at

1063-7850/01/2712-1038$21.00

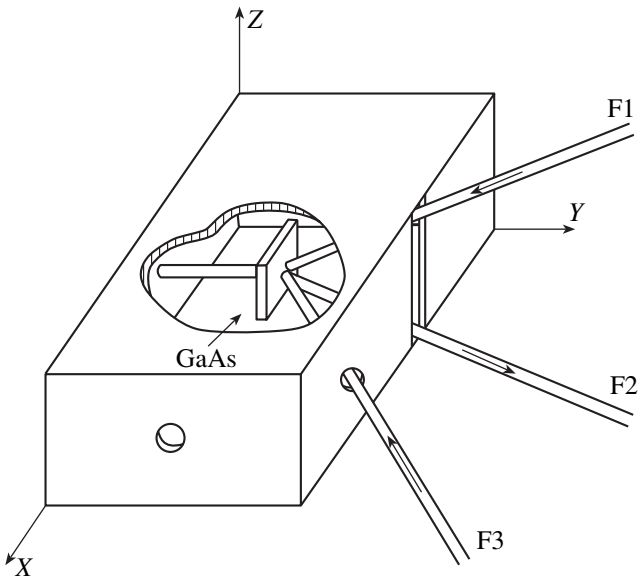

Fig. 1. Schematic diagram showing a GaAs sample mounted on a quartz rod and optical fibers F1–F3 in a microwave cavity used for the MMR measurements (*X*, *Y*, *Z* are spatial coordinate axes).

T = 77 K. At this temperature, the free carrier concentration in the sample film was $n \sim 10^{21}$ m^{-3} and the carrier mobility was $\mu \sim 1$ m^2 s/V.

The GaAs sample was mounted on a quartz rod, placed into a microwave (3-cm) cavity, and adjusted at the maximum electric field strength (Fig. 1). The electric component of the microwave field in the cavity was ~5×10^3 V/m. The sample plane was parallel to the electric field vector. The microwave field intensity in the cavity was modulated at a frequency of f = 330 Hz. The probing light beam from an incandescent lamp was passed through a monochromator and transmitted to the sample via an optical fiber F1. The probing light intensity on the sample surface was ~10 W/m^2. The reflected light was collected and transmitted via optical fiber F2. The MMR signal was measured at the frequency f by a lock-in technique. The optical fibers were introduced into the cavity via a slit in the narrow side wall. This geometry reduces to minimum the possible microwave field distortions in the cavity.

For the comparison, we have also measured the photoreflectance spectra. The pumping He–Ne laser radiation (quantum energy, E_p = 1.96 eV) with the intensity modulated at the same frequency (330 Hz) was transmitted to the sample via optical fiber F3. The pumping light intensity on the sample surface was 10^3 W/m^2. The guides F1–F3 represented multimode optical fibers with a diameter of 300 μm.

The photoreflectance spectrum of the GaAs sample studied (Fig. 2) exhibits a classical shape. The spectrum was described in terms of a model developed in [5]. For the probing quantum energies exceeding the bandgap of GaAs (E_g = 1.511 eV), the Franz–Keldysh oscillations in the photoreflectance spectrum are related to the pumping-induced modulation of the built-in electric field in a depleted subsurface region of the sample film.

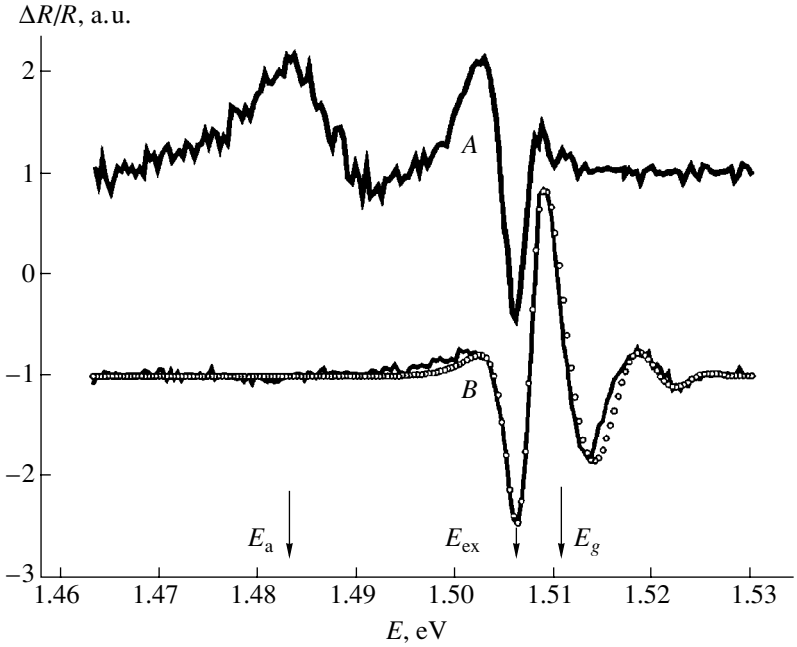

Fig. 2. Experimental (solid curves) and theoretical (open circles) GaAs reflectance spectra measured by (*A*) microwave modulated reflectance and (*B*) photoreflectance methods. For the convenient comparison, the spectra are reduced to the same sale and shifted in the ordinate by +1 and –1 relative to zero, respectively.

Estimated from the model spectrum, the strength of this field amounted to $\sim 3 \times 10^5$ V/m.

The microwave-field-induced heating of charge carriers in semiconductors violates a thermodynamic equilibrium between the diffusion and drift currents. This leads to the appearance of a built-in thermo-emf due to the hot electrons [6]. This phenomenon is most pronounced in heterostructures [7]. The charge carrier heating can also be achieved by passing electric current through contacts on the semiconductor. This way of heating is employed in the method of current-modulated reflectance measurements [8]. In contrast to this, the MMR technique is free of contacts. The absence of the Franz–Keldysh oscillations in the MMR spectrum (Fig. 2) shows that the longitudinal microwave field does not modify the transverse built-in electric field in the depleted region of the sample. This fact is indicative of a small level of the microwave-induced thermo-emf of hot electrons, which is quite natural for a thin-film sample.

The photoreflectance spectra of GaAs may reveal the acceptor states [9, 10], but we failed to observe the corresponding signals by this method. However, the MMR spectrum displayed a feature (E_a = 1.483 eV) in the energy region corresponding to electron transitions from the acceptor levels to the conduction band. The mechanisms responsible for modulation of the acceptor states in the photoreflectance and MMR techniques can be different. The *n*-GaAs sample film studied represented a compensated semiconductor, in which all acceptors are negatively charged in the absence of external perturbations. The conduction band electrons heated by the microwave field modify the fluctuation potential created by the charged impurities. This leads to a change in the probability of electron excitation from the acceptor levels to the conduction band by the probing light, that is, to a change in the absorption and reflection coefficients.

The exciton states (E_{ex} = 1.507 eV) sensitive to various external factors [11] are manifested in both photoreflectance and MMR spectra. In the MMR method, excitons can be modulated by a change in the rate of impact excitation by the microwave-heated conduction electrons. In the photoreflectance spectrum, the exciton-related feature overlaps with a peak due to the Franz–Keldysh effect in the depleted film region. The MMR spectrum displays the exciton response in a better resolved form.

The GaAs film was selected as an object for this investigation taking into account relative simplicity of interpretation of the experimental data. However, the possibilities of MMR measurements are by no means restricted to homogeneous semiconductor films. For example, we obtained the MMR spectra from heterostructures used in the high-electron-mobility transistors. The results of these investigations will published upon quantitative analysis.

Acknowledgments. The authors are grateful to A.V. Frantsesson (Fryazino Branch, Institute of Radio Engineering and Electronics) for fruitful discussions of the experimental part and to V.P. Gapontsev (IRE–Polus Group) for his help in all stages of this work.

This study was supported by the Russian Foundation for Basic Research, project no. 00-02-16655.

REFERENCES

1. M. Cardona, *Modulation Spectroscopy* (Academic, New York, 1969; Mir, Moscow, 1972), Series Solid State Physics, Supplement 11.
2. R. E. Nahory and J. L. Shay, Phys. Rev. Lett. **21** (23), 1569 (1968).
3. O. J. Glembocki and B. V. Shanabrook, Semicond. Semimet. **36**, 221 (1992).
4. O. A. Ryabushkin and V. A. Sablikov, Pis'ma Zh. Éksp. Teor. Fiz. **67** (3), 217 (1998) [JETP Lett. **67**, 233 (1998)].
5. J. P. Estrera, W. M. Duncan, and R. Glosser, Phys. Rev. B **49** (11), 7281 (1994).
6. V. I. Denis and Yu. K. Pozhela, *Hot Electrons* (Mintis, Vilnius, 1971).
7. Z. S. Gribnikov, K. Hess, and G. A. Kosinovsky, J. Appl. Phys. **77** (4), 1337 (1995).
8. O. A. Ryabushkin and E. I. Lonskaya, in *Proceedings of 10th International Conference on Modulated Semiconductor Structures, Linz, 2001*.
9. A. N. Pikhtin, V.-M. Airaksinen, H. Lipsanen, *et al.*, J. Appl. Phys. **65** (6), 2556 (1989).
10. A. N. Pikhtin and M. T. Todorov, Fiz. Tekh. Poluprovodn. (St. Petersburg) **28** (6), 1068 (1994) [Semiconductors **28**, 616 (1994)].
11. C. Tanguy, J. Appl. Phys. **80** (8), 4626 (1996).

Translated by P. Pozdeev

Technical Physics Letters, Vol. 27, No. 12, 2001, pp. 1041–1043. Translated from Pis'ma v Zhurnal Tekhnicheskoĭ Fiziki, Vol. 27, No. 24, 2001, pp. 35–39.

A Thin Subsurface Layer of a Polymer Film Studied by Atomic Force Microscopy

V. I. Trigub, A. V. Plotnov, and A. N. Kiselev

Nizhni Novgorod State Technical University, Nizhni Novgorod, Russia

Received March 13, 2001; in final form, August 7, 2001

Abstract—A thin subsurface layer of a PMMA based resist film was studied in an atomic force microscope (AFM). An analysis of the AFM image allowed a modified subsurface layer thickness to be estimated, in which the polymer density is greater than that in the bulk of the film. © *2001 MAIK "Nauka/Interperiodica".*

According to the Gibbs theory, a thin layer of a liquid phase at the liquid–gas interface is characterized by an excess of the free energy [1, 2]. During the formation of a thin polymer film from a melt or solution, the excess free energy must result in the formation of a thin modified subsurface layer [3, 4]. Indeed, a resultant of the forces acting upon a molecule on the polymeric liquid surface is directed toward the bulk, thus creating a surface molecular pressure. In the course of a thermal treatment of the polymer film, this pressure drives the molecules to approach one another to a distance sufficient for the formation of intermolecular bonds [5]. The process of polymerization under the of molecular pressure takes place only in a thin subsurface layer with a thickness from a few tenths of a nanometer to several dozens of nanometers, depending on the polymer composition. In the bulk of the liquid phase, a time-average resultant of the molecular interaction forces is zero due to the symmetry of the overall force field.

The presence of such a modified subsurface layer in a polymer-based resist film gives rise to a barrier effect hindering the solvent outdiffusion from the film in the course of a thermal treatment [4]. The presence of a modified subsurface layer in a polymer film was indirectly confirmed in [5], where it was shown that the time required for the complete removal of solvent from a polymer resist film depends on the method of material drying. In the case of a rapid heating under the conditions of drying by IR radiation, the subsurface layer is significantly thinner as compared to that upon drying in a thermal box. As a result, a maximum rate of the solvent evaporation from the resist layer is achieved markedly faster under the IR drying conditions than in the thermal box.

Other evidence for the existence of a thin modified subsurface layer was obtained in our recent experiments reported in [6]. We observed a periodic variation in the thickness of a poly(methyl methacrylate)–methacrylic acid (PMMA–MAA) copolymer film heated at a constant temperature. Such a periodic change in the copolymer film thickness as a result of the thermal treatment can take place only in the presence of a modified subsurface layer [7]. However, experimental determinations of the thickness of this layer in polymer films were not performed previously because this value is very small.

We have studied a thin subsurface layer in the films of a positive photoresist formed on a KDB-4 silicon wafer surface by centrifugal method using a polymer solution (4.5% solution of PMMA with $M = 638400$ in diglyme modified with organohydride disilane) [8]. The electron resist solution viscosity was 46.7 cSt and the substrate was rotated during deposition in the centrifuge at a rate of 850 rpm. After the centrifugal deposition, the resist film was dried in air for 30 min at 170°C in a thermal box. After this treatment, the resist layer thickness was about 1.0 μm (see the figure).

A thin subsurface layer in the resist film was studied in an atomic force microscope (AFM) of the Topometrix TMX-2100 type. The investigation was performed in air by the method of friction force measurement in the contact mode. According to this method, the sample surface is scanned with a point microprobe and the friction force acting upon the probe is measured. The force can be expressed as

$$F = \mu N, \tag{1}$$

where N is the normal response force acting upon the probe from the sample upon and μ is the local friction coefficient.

In an AFM image, the regions characterized by a higher friction coefficient appear as bright, while the regions with lower μ values show a dark contrast. It must be emphasized that the local friction coefficients in Eq. (1) can significantly differ from the well-known values of the dry friction coefficients given in hand-

1063-7850/01/2712-1041$21.00

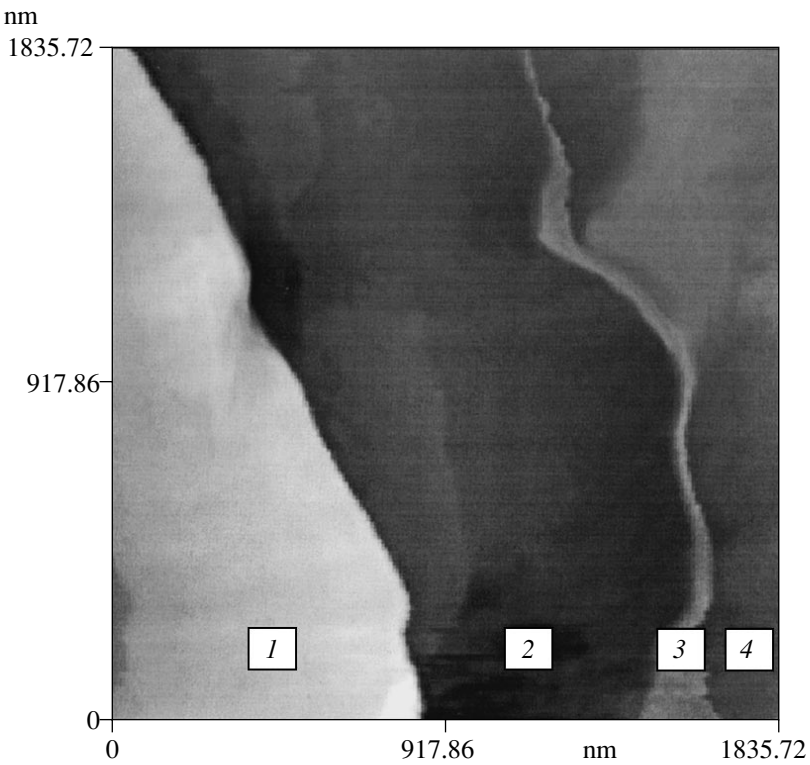

An AFM image of the cross section fracture surface: (*1*) silicon substrate; (*2*) PMMA based resist layer; (*3*) thin modified subsurface polymer layer; (*4*) FP-383 resist layer.

books for various materials. This is explained by a fundamental difference between mechanisms involved in the dry friction between macroscopic solid bodies and in the interaction between AFM microprobe and the sample surface. In the former case, a significant role in friction belongs to the entanglements between microscopic roughnesses on the two surfaces in contact. In the latter case, the size of a contact region between the AFM probe and the sample surface is as small as 0.1–1 nm, depending on the probe load, which is much smaller that the usual surface roughness size. The local friction coefficient is directly proportional to the sample material density. As a result, bright areas in the AFM image (see the figure) correspond to the sample regions of higher density.

In the samples studied, a modified subsurface layer was found in the AFM images of a cross section fracture surface of a silicon substrate coated with a polymer resist layer. The samples were prepared by fracturing at liquid nitrogen temperature as described in [9]. The low temperature prevents the resist edge from plastic deformation during fracture. However, the study of the sample cross section edges in the AFM is hindered by jumps of the force field at the solid–gas interface [10]. In order to eliminate this effect, the base PMMA film was covered with a film of the FP-383 photoresist deposited by centrifuging onto a substrate rotating at 550 rpm. The layer of FP-383 (representing a mixed solution of the light-sensitive compound naphthoquinonediazide and a novolac resin in dioxane [11]) was dried in a thermal box for 20 min at 70°C, which resulted in the formation of a 7.2-μm-thick polymer film. A typical AFM image of the cross section of a silicon substrate with a double resist layer is presented in the figure. As can be seen, the thickness of a modified subsurface layer clearly observed in the PMMA resist fracture surface varies along the resist surface, ranging from 14.1 to 70.5 nm.

Conclusions. (1) A resist film deposited by centrifuging from a PMMA solution in diglyme, followed by drying in a thermal box at 170°C, contains a modified subsurface polymer layer.

(2) The density of this thin modified subsurface polymer layer is greater than that of the bulk polymer (as indicated by bright contrast in the AFM image).

(3) The thickness of the modified subsurface layer formed in the PMMA-based resist film exhibits a scatter from 14.1 to 70.5 nm.

REFERENCES

1. A. S. Kompaneets, *Theoretical Physics* (Gostekhizdat, Moscow, 1957).

2. E. A. Guggenheim, *Modern Thermodynamics by the Methods of Willard Gibbs* (Methuen, London, 1933; Goskhimizdat, Leningrad, 1941).
3. V. I. Trigub and P. B. Boldyrevskiĭ, Pis'ma Zh. Tekh. Fiz. **25** (23), 91 (1999) [Tech. Phys. Lett. **25**, 967 (1999)].
4. V. I. Trigub and G. L. Gol'denberg, Izv. Vyssh. Uchebn. Zaved., Mater. Élektron. Tekh., No. 4, 41 (1988).
5. V. P. Lavrishchev, Yu. I. Prokhorov, and Z. I. Khorina, Élektron. Tekh., Ser. 3: Mikroélektron. **1**, 86 (1975).
6. V. I. Trigub, A. V. Plotnov, I. N. Bykova, *et al.*, Zh. Prikl. Khim. (St. Petersburg) **73** (8), 1353 (2000).
7. V. I. Trigub, A. V. Plotnov, and N. A. Potatina, in *Proceedings of the Seventh International Scientific and Technical Conference "Topical Problems of Solid-State Electronics and Microelectronics" (PÉM-2000), Taganrog, 2000*, Part 1, p. 71.
8. S. A. Bulgakova, Yu. D. Semchikov, V. V. Semenov, *et al.*, Vysokomol. Soedin., Ser. B **37** (4), 706 (1995).
9. *Introduction to Integrated Optics*, Ed. by M. K. Barnoski (Plenum, New York, 1974; Mir, Moscow, 1977).
10. Yu. N. Moiseev, V. M. Mostepanenko, V. I. Panov, *et al.*, Phys. Lett. A **132**, 354 (1988).
11. A. I. Kurnosov, *Materials for Semiconductor Devices and Integrated Circuits* (Vysshaya Shkola, Moscow, 1980).

Translated by P. Pozdeev

Technical Physics Letters, Vol. 27, No. 12, 2001, pp. 1044–1046. Translated from Pis'ma v Zhurnal Tekhnicheskoĭ Fiziki, Vol. 27, No. 24, 2001, pp. 40–45.

Bragg's Reflection of the Optical and Acoustic Waves from Photoinduced Periodic Structures in Iron-Doped Lithium Niobate

N. M. Ushakov and V. V. Kolosov

Saratov Branch, Institute of Radio Engineering and Electronics, Russian Academy of Sciences, Saratov, Russia
e-mail: nmu@mail.saratov.ru

Received April 28, 2001; in final form, August 7, 2001

Abstract—The possibility of the longitudinal hypersonic wave reflection from a photoinduced Bragg's grating in a photorefractive medium such as $LiNbO_3$:Fe is experimentally demonstrated. The results can be of interest for the development of optically controlled acoustic wave delay lines. *© 2001 MAIK "Nauka/Interperiodica".*

In one of the first papers reporting on a photoinduced variation of the velocity of transverse acoustic waves in lithium niobate [1], it was pointed out that a change in the refractive index at the laser beam spot on the target is accompanied by a change in the velocity of shear waves. This phenomenon suggests the possibility of a resonance reflection of acoustic waves from a photoinduced periodic structure. Below, we report on the results of investigation of the photoinduced gratings obtained in $LiNbO_3$:Fe crystals in the visible spectral range and of Bragg's reflection of the optical and acoustic waves on these gratings.

The experiments were performed with lithium niobate single crystals with an iron impurity concentration of 0.02%. A sample shaped as a 52-mm-long rectangular bar with a 3×5.5-mm cross section was oriented with the long edge parallel to the principal optical axis *C* of the acoustic waveguide. A thin-film zinc-oxide-based electroacoustic piezotransducer mounted on one edge perpendicular to the *C* axis was excited in a 400–900 MHz frequency range by a flat spiral electrode. The efficiency of a single longitudinal wave conversion was ≈6 dB. The optical radiation entered the crystal through a long side edge (3×52 mm) parallel to the optical axis.

Figure 1 shows a schematic diagram of the experimental setup used for the measurement of Bragg's reflection of the optical and acoustic waves from a grating photoinduced in the piezoelectric photorefractive medium. A laser beam passed through an optical system comprising a beam splitter, optical gates (*2*, *3*), and cylindrical lenses (*6*, *7*) convert into two orthogonally polarized crossed flat rays (*1*, *1*'). The rays converge in the focal planes of identical cylindrical lenses, coinciding with the principal plane of a lithium niobate crystal (*8*) mounted on a goniometer table. The orthogonally polarized rays making an angle of 2θ form a photoinduced grating in the crystal. The recorded gratings could be erased with the aid of a diverging beam formed by a reflector (*9*) irradiated with a UV (380 nm) laser (*10*).

The radioelectronic measuring circuit represented a superheterodyne microwave receiver comprising two fast-response photodetectors (*11*, *12*), directional microwave mixing coupler (*16*), intermediate frequency amplifier (*17*), microwave heterodyne (*18*), and oscillograph (*19*). The hypersonic wave was excited in the crystal with the aid of a microwave generator (*13*) operating in the 400–1200 MHz range. The transmitted and reflected microwave signals were commutated by coaxial switches (*14*, *15*).

The microwave-modulated photoresponse was measured in a photomixer by a laser-heterodyne technique when two collinear optical beams with the frequencies

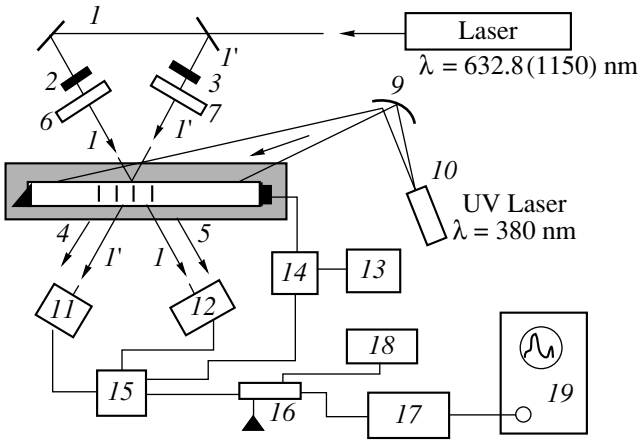

Fig. 1. A schematic diagram of the experimental setup used for the measurement of Bragg's reflection of the optical and acoustic waves from a grating photoinduced in the piezoelectric photorefractive medium. See the text for explanations.

1063-7850/01/2712-1044$21.00 © 2001 MAIK "Nauka/Interperiodica"

ω and ω ± Ω struck the detector. Here, ω is the frequency of a ray *1* diffracted on the photoinduced grating at the closed gate *3* (or ray *1*' diffracted at the close gate *2*) and ω ± Ω is the frequency of rays *1*' and *1*, respectively, diffracted on the acoustic waves in the crystal. The sensitivity of the microwave receiver for the laser-heterodyne operation was ~120 dB.

The photoinduced grating recording at a wavelength of 0.63 μm was performed using two crossed flat 1.5-mW beams. The optical system allowed the grating size to be changed from 1 to 18 mm, whereby the incidence angle θ varied within 2.17°–2.3° and the grating period, within 7.8–8.3 μm. The grating was recorded and monitored at two wavelengths (0.63 and 1.15 μm) by means of Bragg's diffraction using one of the two crossed extraordinary rays (*1* or *1*') on the photoinduced grating. The recorded gratings were fixed using a method described elsewhere [2].

As is known, the efficiency I_d/I_0 of Bragg's scattering on a periodic structure is determined by the formula [3]

$$I_d/I_0 = \sin^2(\pi\Delta n L_1/\Lambda), \quad (1)$$

where $\Lambda = V/f$ is the grating period, Δn is a change in the refractive index, L_1 is the interaction (or the grating) length, V is the acoustic wave velocity, and f is the hypersonic wave frequency.

At the same time, a change in the refractive index of the extraordinary ray for the internal field E_s directed along C or Z axis in the electrooptical medium can be determined as [4]

$$\Delta n_e = -0.5ne3r_{33}E_{sz}. \quad (2)$$

Combining expressions (1) and (2), it is easy to determine the induced internal field E_s in the $LiNbO_3$:Fe [001] crystal:

$$E_s = (2\Lambda/\pi L_1 n_e^3 r_{33})\arcsin(I_d/I_0)^{1/2}, \quad (3)$$

where n_e is the refractive index for the extraordinary ray, r_{33} is the electrooptical coefficient of lithium niobate for the electric field oriented along Z axis. The values of the diffraction efficiency parameter and the interaction length are determined experimentally.

The photoinduced grating size (width) in the direction perpendicular to the optical axis varied from 2 to 18 mm. Using the value of diffraction efficiency (80%) experimentally measured at a wavelength of 0.63 μm, we can readily determine a change in the refractive index Δn_e from relationship (1). For the parameters indicated above, the amplitude of perturbation of the refractive index of the extraordinary beam amounts to $\Delta n_e = 1.1 \times 10^{-4}$, in good agreement with the published data (see, e.g., [4, 5]). The internal induced electric field strength determined by formula (3) for the same parameters is $E_s \approx 7.4 \times 10^6$ V/m.

Let us consider the acoustic part of this experiment. During the photoinduced grating recording, the periodic induced electric field E_s produces a change in the acoustic wave velocity as a result of the nonlinear piezoelectric effect. For a constant electric field E_s and a mechanically constrained crystal, the effective elastic modulus C^*_{ijkl} can be written as [6]

$$C^*_{ijkl} = C_{ijkl} - e_{mijkl}E_m.$$

As can be readily shown, $\Delta V(E)/V(0) = \Delta C^*(E)/2C(0)$. For $C_{3333} = 2.279 \times 10^{11}$ N/m^2 and $e_{3333} = -17.3$ C/m^2, the relative change in the hypersonic wave velocity amounts to $\Delta V(E)/V(0) \approx 2.81 \times 10^{-4}$.

By analogy with relationship (1), the acoustic wave reflection coefficient R_{ac} can determined as

$$R_{ac} = I_r/I_0 = \sin^2(\pi(\Delta V(E)/V(0))L_z/\Lambda),$$

where L_z is the grating length along Z axis and Λ is the acoustic wavelength.

The longitudinal acoustic wave excited by the thin-film transducer propagates along the grating. The condition of Bragg's reflection for the acoustic wave diffracting on the grating is fulfilled provided that the acoustic wavelength is equal to a doubled grating period. The acoustic wave reflection coefficient measured at a frequency of 420 MHz for a grating length of 2.6 mm was as small as 0.01, in agreement with the calculated value.

Figure 2 shows a plot of the experimental acoustic wave reflection coefficient versus grating length. The grating period was equal to the length of the acoustic wave excited at 840 MHz. The dashed curve in Fig. 2

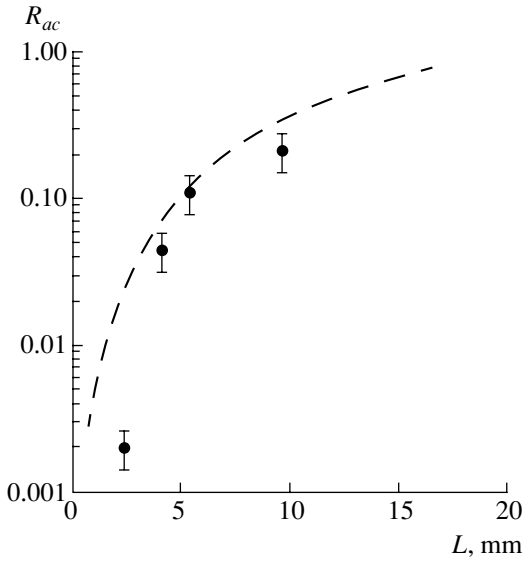

Fig. 2. Experimental (black dots with error bars) and calculated (dashed curve) plots of the acoustic wave reflection coefficient R_{ac} versus photoinduced grating length L. The grating period was equal to the length of the acoustic wave excited at 840 MHz.

presents the results of calculations using the impedance method [7].

The photoinduced grating, as a periodic reflecting structure or a distributed acoustic feedback element, can be formed at any distance from the acoustic transducer. Taking into account the possibilities of well developed rapid grating record and erase technology, we may suggest that the phenomenon of optically controlled acoustic wave reflection in photorefractive media can find wide application in data processing systems, for example, as microwave signal delay lines with an optically controlled delay time.

REFERENCES

1. Yu. V. Vladimirtsev and A. V. Golenishchev-Kutuzov, Fiz. Tverd. Tela (Leningrad) **22** (2), 217 (1980) [Sov. Phys. Solid State **22**, 125 (1980)].
2. I. F. Kanaev, V. K. Malinovskiĭ, and N. V. Surovtsev, Fiz. Tverd. Tela (St. Petersburg) **42** (11), 2079 (2000) [Phys. Solid State **42**, 2142 (2000)].
3. Yu. K. Rebrin, *Optical Beam Handling* (Sov. Radio, Moscow, 1977).
4. Yu. S. Kuz'minov, *Lithium Niobates and Tantalates. Materials for Nonlinear Optics* (Nauka, Moscow, 1975).
5. M. Zgonik, R. Schlesser, I. Biaggio, *et al.*, J. Appl. Phys. **74** (2), 1287 (1993).
6. B. D. Zaitsev and I. E. Kuznetsova, IEEE Trans. Ultrason. Ferroelectr. Freq. Control **43** (4), 701 (1996).
7. H. A. Haus, *Waves and Fields in Optoelectronics* (Prentice-Hall, Englewood Cliffs, 1984).

Translated by P. Pozdeev

Technical Physics Letters, Vol. 27, No. 12, 2001, pp. 1047–1049. Translated from Pis'ma v Zhurnal Tekhnicheskoĭ Fiziki, Vol. 27, No. 24, 2001, pp. 46–51.

Atmospheric Degradation of the Proton-Irradiated Textured Oxide Superconductors

M. U. Kalanov, E. M. Ibragimova*, T. Kh. Khaidarov, M. S. Paizullakhanov, and V. M. Rustamova

Institute of Nuclear Physics, Academy of Sciences of the Republic of Uzbekistan, Tashkent, Uzbekistan

** e-mail: eibragim@suninp.tashkent.su*

Received May 21, 2001

Abstract—Atmospheric degradation of the structure and superconducting properties of the isotropic and textured $YBa_2Cu_3O_{7-\delta}$ ($\delta = 0.07$) ceramics as a result of prolonged storage in air under normal conditions was studied on the samples possibly irradiated with 18-MeV protons to a maximum fluence of 6×10^{14} p/cm^2. It is demonstrated that the proton irradiation to a certain dose increases stability of the structure and superconducting properties of the ceramics with respect to atmospheric degradation; an additional inhibition of the degradation is achieved in textured ceramics. *© 2001 MAIK "Nauka/Interperiodica".*

As is known, the structure of superconducting yttrium–barium oxide ceramics of the $YBa_2Cu_3O_{7-\delta}$ (YBCO) type is unstable on exposure to atmospheric air, especially under conditions of increased humidity and CO_2 content [1–5]. This disadvantage significantly impairs the prospects for wide practical applications of the YBCO ceramics [6]. In connection with this problem, there were attempts at protecting the yttrium ceramics from atmospheric degradation by doping the material with noble metals [7], two-side coating with thin organic films or epoxy compounds [4], or modifying the structure by irradiation [8, 9]. Below, we report on the results of investigation of the stability of structural parameters and superconducting properties of YBCO ceramics in the course of prolonged storage. The comparative test was performed on the initial (unirradiated) and proton-irradiated samples of isotropic and textured ceramics.

The samples of isotropic ceramics were prepared by the conventional solid-state synthesis in air, while the textured samples were obtained by recrystallization [10]. Among the series of as-sintered ceramic pellets with a diameter of 12 mm and a thickness of 0.6 mm (both isotropic and textured), we selected the $YBa_2Cu_3O_{6.93}$ samples characterized by the same oxygen content ($\delta \approx 0.07$) and lattice parameters ($a \approx 3.824$ Å, $b \approx 3.885$ Å, $c \approx 11.676$ Å). The densities of isotropic and textured samples were 4.9 and 5.2 g/cm^3, respectively. The degree of texturing was determined as $F_t = (P_t - P_i)/(1 - P_i) = 0.64$, where P_t and P_i are the intensity ratios of the sum of (OO*L*) reflections to the total sum of structural lines (*HKL*) for the textured and isotropic ceramics, respectively [10]. A fraction of the samples were irradiated by protons with an energy of 18 MeV to various doses (up to 6×10^{14} p/cm^2). The proton irradiation was effected in air at room temperature on the U-150 particle accelerator.

The structural characteristics of YBCO pellets (lattice parameters *a*, *b*, *c*; the ratio of line intensities I_{012}/I_{102} in the (012) and (102) doublet; and the bulk oxygen content ($7 - \delta$)) were determined from the X-ray diffraction patterns measured on a DRON-UM1 diffractometer using CuK_α radiation with $\lambda = 1.542$ Å. The physical characteristics (resistivity ρ, critical temperature T_c, and superconducting transition width ΔT) were measured by the conventional dc four-point-probe technique using a probing current of 1 mA. The samples were stored for three months in air at 300 K and a relative humidity of ~50% with periodic (every decade) measurements of the structural and electrical characteristics. The results of determination of the structural parameters and superconducting properties of isotropic and textured YBCO samples tested before and after the proton irradiation are summarized in the table.

A comparative analysis of the X-ray diffraction patterns of unirradiated and irradiated samples revealed changes neither in the shapes, intensities, and angular positions of the main diffraction peaks such as (013), (103), (110), (006), (020), (200), (116), (123), (213), nor in the interdoublet spacings at $2\theta = (46–48)°$ and $(58–60)°$ (where θ is the scattering angle) characteristic of the orthorhombic superconducting YBCO phase. As can be seen from data in the table, the lattice parameters (*a*, *b*, *c*), the oxygen content ($7 - \delta$), and the degree of texturing F_t are virtually unaffected by the proton irradiation; nor did these characteristic change upon prolonged storage in air under the conditions indicated above.

Among the structural characteristics, only the ratio of line intensities I_{012}/I_{102} varied with increasing proton

Variation of the structural parameters, superconducting properties, and resistivity of superconducting YBCO ceramics upon prolonged room-temperature storage in air

Sample	Fluence, p/cm^2	a, Å	b, Å	c, Å	7–δ, a.u.	F_t, a.u.	After sintering				After 3-month storage			
							T_c, K	ΔT, K	ρ, mΩ cm	I_{012}/I_{102} a.u.	T_c, K	ΔT, K	ρ, mΩ cm	I_{012}/I_{102} a.u.
Isotropic	0	3.824	3.884	11.676	6.930	–	91	1.8	3.1	0.660	87.1	2.7	7.9	0.690
	2×10^{14}	3.824	3.885	11.676	6.929	–	90.8	2.0	6.2	0.681	89.7	2.4	6.9	0.686
	4×10^{14}	3.825	3.885	11.676	6.927	–	90.4	2.5	11.1	0.708	89.1	2.9	12.4	0.725
Textured	0	3.826	3.891	11.677	6.929	0.64	91.5	1.7	2.1	0.654	90.3	2.0	3.3	0.669
	2×10^{14}	3.826	3.891	11.677	6.929	0.64	91.4	1.8	2.4	0.655	90.9	1.9	2.5	0.661
	4×10^{14}	3.826	3.891	11.677	6.928	0.64	91.2	1.9	3.0	0.662	90.8	2.0	3.1	0.668

fluence and storage time. This is explained by the fact that the (012)–(102) doublet is extremely sensitive to the oxygen content in the intergranular and subsurface layers of the material [10–12]. It must me noted that the change in I_{012}/I_{102} was well correlated with variations in the resistivity of samples. The most pronounced increment in the resistivity at 300 K was observed in the samples of non-irradiated ceramics, where ρ increased by 155 and 60% in the isotropic and textured ceramics, respectively; simultaneously, the I_{012}/I_{102} ratio increased by 4.5% in the isotropic ceramics and by 2.5% in the textured samples, while the superconducting transition temperature decreased by 3.9 and 1.2 K, respectively.

In the ceramics irradiated to a fluence of 4×10^{14} p/cm^2, the increase in resistivity and I_{012}/I_{102} ratio upon a 3-month storage reached 11.7 and 2.7%, respectively, for the isotropic samples versus 3.3 and 1% for the textured samples. A decrease in the superconducting transition temperature in the isotropic and textures ceramics did not exceed 1.3 and 0.4 K, respectively. The samples irradiated with protons to a dose of 6×10^{14} p/cm^2 exhibited a significant increase in the I_{012}/I_{102} ratio (up to 0.796), a sharp drop in the superconducting transition temperature (to 85 K), and considerable increase in the crystal lattice parameters.

The observed difference in the stability of initial and proton-irradiated YBCO samples (both isotropic and textured) can be explained within the framework of a model of granulated oxide superconductor structure. According to this, a ceramic superconductor is considered as a system of grains connected by intergranular contacts representing Josephson's junctions [13]. The states of oxygen atoms occurring in the intergranular and subsurface layers (featuring unsaturated valence bonds) are more active as compared to those of atoms in the regular grain structure (inside the grains) [9–12]. Since the superconducting oxide compounds belong to the well-known class of materials with a perovskite structure, which are capable of reversibly absorbing and releasing oxygen even under the normal conditions [6, 14], we may expect that changes in the phase state of a ceramic sample take place predominantly in the intergranular and subsurface layers and are related to the active behavior of oxygen [10–12].

An increase in the I_{012}/I_{102} ratio in the irradiated samples is evidence of the formation of a tetragonal phase layer in the intergranular and subsurface regions as a result of the *ortho–tetra* phase transition, which is caused by the radiation-stimulated desorption of oxygen from the CuO_x planes [8–12]. In the course of the proton irradiation, the radiation-stimulated desorption of oxygen from ceramics dominates over the thermal sorption of oxygen from the environment [9–11]. As a result, each superconducting grain becomes coated with a thin layer of the tetragonal phase. At the same time, the granules retain the initial superconducting structure inside because neither lattice parameters nor the bulk oxygen content $(7 - \delta)$ is changed by the irradiation. Since the tetragonal modification is more stable under normal conditions than the orthorhombic phase [1–3, 6], this layer effectively protects the sample from further degradation in the course of prolonged storage in air. Indeed, an increase in the I_{012}/I_{102} ratio in the samples irradiated to a fluence of 4×10^{14} p/cm^2 and then stored for three months was as small as 2.7 and 1% for the isotropic and textured ceramics, respectively.

A significantly greater stability with respect to degradation observed for the textured ceramics as compared to the isotropic samples is explained by a smaller volume fraction of the subsurface and intergranular layers in the former case, which is related to a more ordered and dense arrangement of grains in the textured samples [10, 11]. Storage of the unirradiated ceramics is accompanied both by the formation of a passivating tetragonal phase in the intergranular and subsurface layers of samples and by the appearance of an impurity (1–4%) of the $BaCO_3$ type as a result of decomposition of the 1–2–3 YBCO phase [1–3, 5, 6]. Therefore, a dominating process in the unirradiated YBCO samples

stored in air is the oxygen and water vapor sorption from outside [1–5] rather than the oxygen desorption from the intergranular and subsurface regions as a result of thermodiffusion. The absorbed water vapor leads to a partial decomposition of the superconducting orthorhombic phase [5, 6], which predominantly also takes place in the intergranular regions and on the surface.

Thus, the proton irradiation to a certain dose increases stability of the structure and superconducting properties of the YBCO ceramics with respect to atmospheric degradation during prolonged storage under normal conditions. The protective effect is due to the formation of a thin surface passivating layer of a tetragonal phase. An additional inhibition of the degradation is achieved in textured ceramics.

REFERENCES

1. I. V. Harris and F. K. Nyang, Solid State Commun. **67** (4), 359 (1988).
2. K. Yu. Kravchenko and V. A. Marchenko, Pis'ma Zh. Tekh. Fiz. **24** (24), 45 (1998) [Tech. Phys. Lett. **24**, 966 (1998)].
3. A. P. Gusev, L. F. Kamalova, *et al.*, Izv. Akad. Nauk, Ser. Fiz. **60** (2), 49 (1996).
4. R. P. Vasquer, M. C. Foote, B. D. Munt, *et al.*, Appl. Phys. Lett. **55** (17), 1801 (1989).
5. B. M. Gorelov, D. V. Morozovskaya, V. M. Pashkov, and V. A. Sidorchuk, Zh. Tekh. Fiz. **70** (9), 50 (2000) [Tech. Phys. **45**, 1147 (2000)].
6. *Physical Properties of High Temperature Superconductors*, Ed. by D. M. Ginsberg (World Scientific, Singapore, 1989; Mir, Moscow, 1990).
7. Beiling Shao, Ansheng Liu, Yigu Zhou, *et al.*, Mater. Res. Bull. **24** (11), 1369 (1989).
8. B. B. Boĭko, F. B. Korshunov, G. V. Gatal'skiĭ, *et al.*, Vestsi Akad. Navuk BSSR, Ser. Fiz.-Mat. Navuk, No. 1, 31 (1990).
9. A. G. Ashirov, É. M. Gasanov, É. M. Ibragimova, *et al.*, Sverkhprovodimost: Fiz., Khim., Tekh. **3** (7), 1454 (1990).
10. M. S. Paĭzullakhanov, M. U. Kalanov, M. Karimov, *et al.*, Sverkhprovodimost: Fiz., Khim., Tekh. **5** (11), 2548 (1992).
11. M. U. Kalanov, M. S. Paĭzullakhanov, R. Kh. Maminov, *et al.*, Pis'ma Zh. Tekh. Fiz. **23** (1), 13 (1997) [Tech. Phys. Lett. **23**, 13 (1997)].
12. V. B. Vykhodets, T. E. Kurennykh, B. V. Slobodin, *et al.*, Fiz. Tverd. Tela (St. Petersburg) **39** (1), 42 (1997) [Phys. Solid State **39**, 35 (1997)].
13. E. Z. Meĭlikhov, Sverkhprovodimost: Fiz., Khim., Tekh. **3** (7), 1422 (1990).
14. P. S. Galasso, *Structure, Properties and Preparation of Perovskite-Type Compounds* (Pergamon, New York, 1969).

Translated by P. Pozdeev

Technical Physics Letters, Vol. 27, No. 12, 2001, pp. 1050–1051. Translated from Pis'ma v Zhurnal Tekhnicheskoĭ Fiziki, Vol. 27, No. 24, 2001, pp. 52–56.

On the Possibility of Increasing and Controlling the Radiation Pulse Duration in Gas-Discharge Lasers

A. I. Fedorov

Institute of the Optics of Atmosphere, Siberian Division, Russian Academy of Sciences, Tomsk, Russia

** e-mail: lfmi@asd.tomsk.su*

Received July 4, 2001

Abstract—The experimental results demonstrating the possibility to increase and control the pulse duration in molecular lasers by means of quasistationary energy pumping into the active laser media are presented. It is shown that the pulse duration in the XeCl, N_2, and CO_2 lasers can be controlled by matching parameters of the energy source and the gas-discharge plasma in the active laser media pumped in a quasistationary regime. © *2001 MAIK "Nauka/Interperiodica".*

The problem of increasing the efficiency of high-pressure gas-discharge molecular lasers by controlling the laser pulse duration is of current importance in many applications. As is known, the regime of excitation of molecules in the working medium determines the specific energy (both deposited and released) and, hence, the laser pulse duration, for example, in XeCl lasers [1–7]. However, increasing the specific deposited energy leads to the development of discharge instabilities related mostly to overheating of the active medium (in a fast pump regime) and instabilities in the gas medium and/or on the electrode surface (in a quasistationary pump regime).

Investigations of the XeCl lasers pumped in a quasistationary regime showed that the laser pulse duration depends both on the discharge gap electrode material (metal, plasma, or combined metal and plasma) [8] and on the time of UV preionization stabilizing the active medium [5–7]. It is believed that one of the main reasons for the discharge instability development is the difficulty of impedance matching between the energy source and a discharge plasma in the active laser medium. A promising method of stabilizing the self-maintained discharge consists in using a quasistationary pump regime with a self-matching UV radiation source (corona, spark, or plasma discharge) operating over the entire discharge period.

Below, we present the experimental results on the possibility to increase and control the pulse duration in molecular lasers by means of quasistationary energy pumping into the active laser media stabilized by UV radiation. The experiments were performed with a two-stage pumping scheme employing self-maintained spark-discharge UV preionization similar to that described in [4]. The discharge parameters and energy characteristics were studied for XeCl, N_2, and CO_2 active laser media.

Figure 1 shows oscillograms of the voltage across the discharge plasma in a XeCl lasers with different parameters of the power supply circuit. A special feature of the quasistationary energy pump regime is the presence of two stages in the discharge: fast (I) and quasistationary (II). Since the UV preionization scheme is included into the power supply storage circuit, the preionization duration is determined by the storage capacitance C_1 (at a constant capacitance of the power supply pulse sharpening circuit, C_2 = 10 nF). In case *1* ($C_2 = C_1$ = 10 nF), the fast stage I lasted for 10 ns and was followed by the discharge contraction corresponding to a negative voltage across the plasma. In case *2* (C_2 = 10 nF, C_1 = 60 nF), the fast stage (I) increased to 20 ns with a smooth transition to the quasistationary stage II. The total bulk discharge duration exceeded 100 ns.

The discharge contraction was observed only at the end of the quasistationary discharge stage. Therefore,

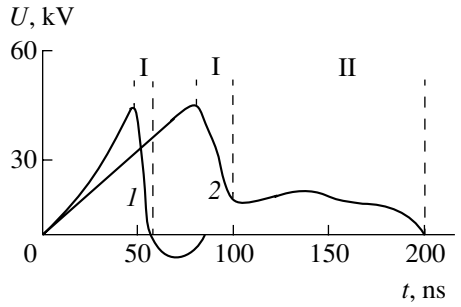

Fig. 1. Oscillograms of the voltage across the discharge plasma in (He)Xe–HCl 10:1 (3 Torr) mixtures at a pressure of 3 atm and a charging voltage of 30 kV in a laser pumped by two-stage schemes employing self-maintained spark-discharge UV preionization: (*1*) $C_1 = C_2$ = 10 nF; (*2*) C_1 = 60 nF, C_2 = 10 nF. Regions I and II correspond to the fast and quasistationary discharge stages, respectively.

1063-7850/01/2712-1050$21.00 © 2001 MAIK "Nauka/Interperiodica"

the transition from fast to quasistationary stage may proceed without discharge contraction. For a short UV preionization, the bulk and electrode instabilities cover the working period. The UV preionization operating over the entire discharge period stabilizes the discharge and does not allow the bulk and electrode instabilities to develop, so that the discharge exhibits a smooth transition from fast to the quasistationary stage. According to Fig. 1, the fast stage duration may exhibit an even twofold increase.

An analogous situation was previously observed for quasistationary pumping with the plasma-discharge UV preionization [8]. Figure 2 shows oscillograms of the voltage across the discharge gap in the form of two plasma electrodes (curve *1*) or a combination of metal and plasma electrode (curve *2*) in a He–Xe–HCl mixture. The plasma electrode ensuring the UV preionization over the entire discharge period limited the discharge contraction, although anode spots were still observed on the metal electrode surface. A criterion of the discharge contraction being absent in the fast discharge stage I can be a decrease to zero in the voltage drop across the plasma, followed by a transition to the quasistationary stage II. The presence of two plasma electrodes increased the UV preionization intensity and, accordingly, reduced the plasma gap breakdown voltage and almost doubled the fast discharge stage duration. In this case, no bulk and electrode instabilities were developed in the discharge gap. Analogous investigations of the duration of fast and quasistationary stages of discharge were performed for the active media of N_2 and CO_2 lasers.

Using stabilization of the self-maintained discharge by the UV preionization (corona, spark, or plasma discharge), we succeeded in increasing the XeCl laser pulse duration from 5 to 400 ns [2, 5, 6]. The quasistationary pump regime, ensuring controlled redistribution of the energy fed to the active medium in the fast and quasistationary discharge stages, allowed the shape of the laser radiation pulses to be controlled [5]. In a CO_2 laser pumped in a quasistationary regime, the pulse duration can be smoothly varied from 0.15 to 2.5 μs and the peak radiation power to be increased up to 10 MW/pulse by extending the fast discharge stage [9]. In an N_2 laser, the pulse duration can be increased from 5 to 20 ns [9–11].

As is known, the N_2 lasers (337 nm) on self-confined transitions operate only in the fast pump regime with a pulse duration on the order of 5 ns. An increase in the pulse duration can be provided by extending the fast discharge stage followed by the transition to a quasistationary stage without discharge contraction (i.e., by using the quasistationary stage as an element of self-matching between impedances of the energy source and the discharge plasma). Therefore, elimination of the early discharge contraction provides for a severalfold increase in the N_2 laser pulse duration.

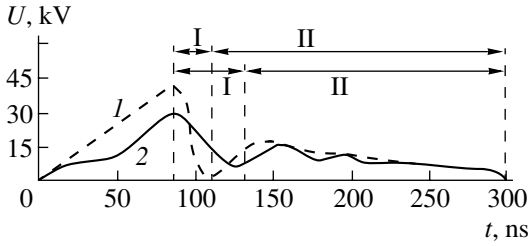

Fig. 2. Oscillograms of the voltage across the discharge plasma in (He)Xe–HCl 20:1 (1.5 Torr) mixtures at a pressure of 2 atm and a charging voltage of 30 kV in a laser pumped by two-stage schemes employing self-maintained plasma-discharge UV preionization with (*1*) plasma electrodes and (*2*) metal and plasma electrodes for C_1 = 30 nF and C_2 = 5 nF. Regions I and II correspond to the fast and quasistationary discharge stages, respectively.

Thus, the method of matching and controlling the parameters of energy source and gas-discharge plasma in molecular lasers, based on the quasistationary pumping of the active laser media stabilized by the UV radiation, allows the pulse duration to be increased in a controlled manner.

REFERENCES

1. V. F. Tarasenko and A. I. Fedorov, Izv. Vyssh. Uchebn. Zaved., Fiz., No. 2, 15 (1981).
2. Yu. I. Bychkov, S. V. Mel'chenko, G. A. Mesyats, *et al.*, Kvantovaya Élektron. (Moscow) **9** (12), 2423 (1982).
3. R. C. Taylor, Appl. Phys. B: Photophys. Laser Chem. **B41**, 1 (1986).
4. A. I. Fedorov and S. A. Brichkov, Opt. Atmos. **2** (7), 772 (1989).
5. A. I. Fedorov, Opt. Atmos. Okeana **10** (11), 1274 (1997).
6. A. I. Fedorov, Opt. Atmos. Okeana **13** (11), 1056 (2000).
7. A. I. Fedorov, Pis'ma Zh. Tekh. Fiz. **26** (14), 71 (2000) [Tech. Phys. Lett. **26**, 625 (2000)].
8. A. I. Fedorov and S. V. Mel'chenko, Zh. Tekh. Fiz. **60** (4), 105 (1990) [Sov. Phys. Tech. Phys. **35**, 463 (1990)].
9. A. I. Fedorov, S. I. Tikhomirov, and B. A. Zhunusov, Opt. Atmos. **2** (9), 1003 (1989).
10. A. I. Fedorov, Opt. Atmos. Okeana **8** (11), 1664 (1995).
11. A. I. Fedorov, Opt. Atmos. Okeana **11** (2/3), 135 (1998).

Translated by P. Pozdeev

Technical Physics Letters, Vol. 27, No. 12, 2001, pp. 1052–1054. Translated from Pis'ma v Zhurnal Tekhnicheskoĭ Fiziki, Vol. 27, No. 24, 2001, pp. 57–63.

Investigation of the Structure of (*p*)3C-SiC–(*n*)6H-SiC Heterojunctions

A. A. Lebedev, G. N. Mosina, I. P. Nikitina, N. S. Savkina, L. M. Sorokin, and A. S. Tregubova

Ioffe Physicotechnical Institute, Russian Academy of Sciences, St. Petersburg, 194021 Russia

Received July 26, 2001

Abstract—The structure of (*p*)3C-SiC–(*n*)6H-SiC epitaxial structures obtained by sublimation epitaxy in vacuum on 6H-SiC substrates was studied by methods of X-ray topography, X-ray diffraction, and transmission electron microscopy. The results showed high structure perfection in the epitaxial layers of both SiC polytypes with a sharp interface between the 3C-SiC and 6H-SiC layers. © *2001 MAIK "Nauka/Interperiodica"*.

Silicon carbide (SiC) is promising material for high-power and microwave electronic devices operated under high-temperature conditions. Owing to a large number of existing crystalline SiC modifications (polytypes), characterized by the same composition but significantly differing physical (in particular, electrical) properties, silicon carbide offers a unique possibility of creating various heterostructures based on the same material [1, 2].

Previously, it was demonstrated that adding certain impurities into the growth zone during the SiC layer synthesis allows the epitaxial layers to be obtained belonging to a structural polytype different from that of the substrate [3–5]. It was found that a factor significantly influencing the heteropolytype epitaxy is the Si/C ratio in the growth zone. An increase in the relative content of Si increases the probability that a cubic silicon carbide modification (3C-SiC) would grow on a 6H-SiC substrate.

In recent years, considerable progress has been achieved in the sublimation epitaxy technology [6] that allowed high-quality epitaxial heterostructures of the (*n*)3C-SiC–(*n*)6H-SiC type to be obtained with good characteristics of the (*n*)3C-SiC films [7]. The purpose of this study was to estimate the structure perfection in epitaxial SiC layers with different conductivity types and for the (*p*)3C-SiC–(*n*)6H-SiC heterojunctions.

We have studied the *p–n* heterostructures grown by sublimation epitaxy in vacuum [6]. The conductivity type of the epitaxial layers and the concentrations of uncompensated donors (acceptors) were determined by measuring the capacitance–voltage (*C–V*) characteristics. The structure of the epitaxial layers was evaluated by the X-ray topographs measured in the X-ray backscattering mode using the Cu$K_{\alpha 1}$ radiation. These measurements employed the asymmetric (113) reflections of a cubic SiC modification, which were shown to reveal a twinned structure of the 3C-SiC layers [8].

In the first growth stage, the *n*-type silicon carbide layer with an uncompensated donor concentration of 2×10^{17} cm^{-3} was grown on the (0001)Si face of Laly's 6H-SiC substrate under the conditions of excess silicon content in the growth zone. An analysis of the X-ray topographs of these deposits (Fig. 1) showed that the epitaxial layer grown on most of the substrate area (central region I) belongs to the 3C-SiC modification, while the remaining part of the epitaxial layer

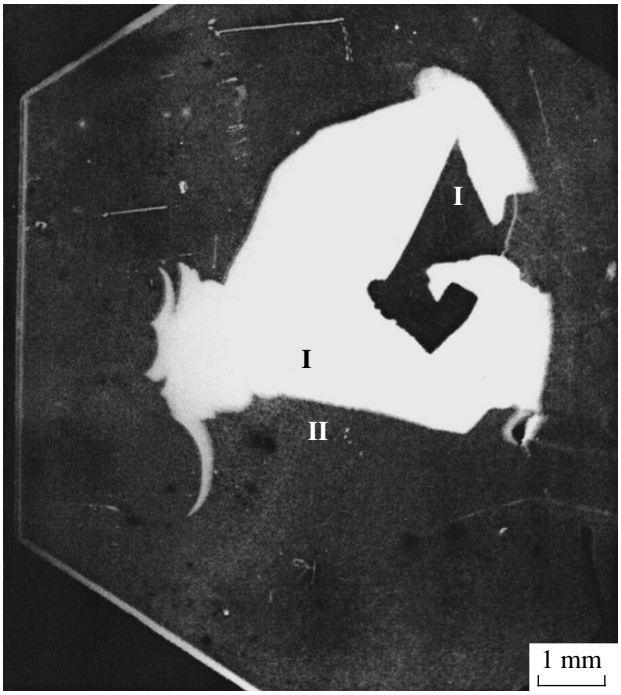

Fig. 1. X-ray topograph of an 6H-SiC substrate with an *n*-SiC epitaxial layer showing the regions of polytypes 3C-SiC (I) and 6H-SiC (II). The pattern was obtained using Cu$K_{\alpha 1}$ radiation in the Bragg geometry for $(311)_{3C}$ reflection.

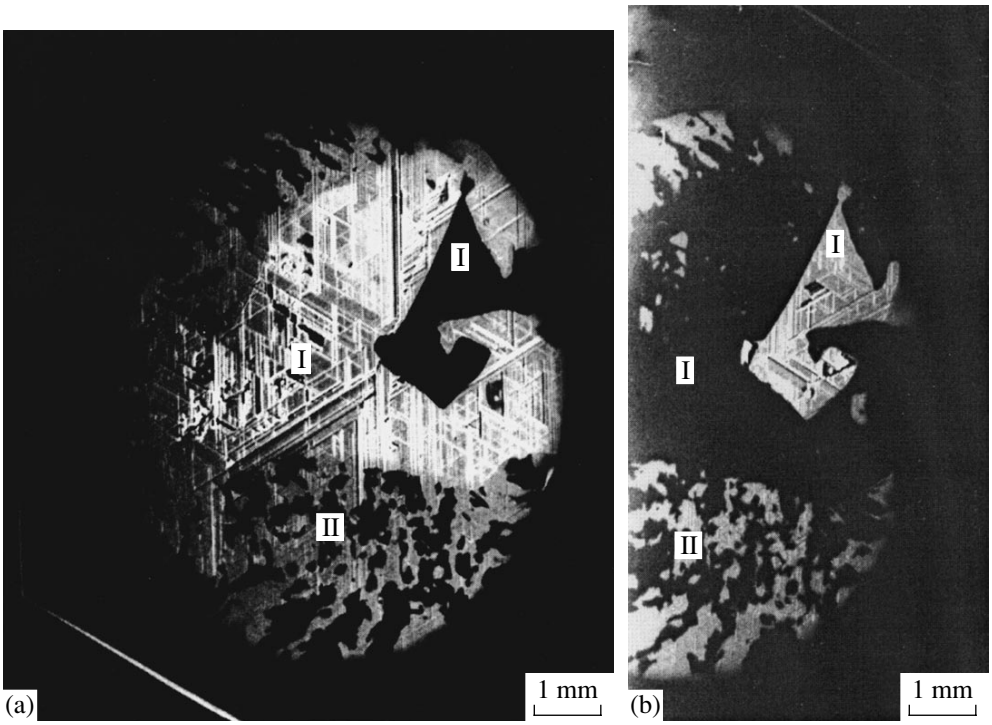

Fig. 2. X-ray topograph of a sample obtained upon growing a *p*-SiC epitaxial layer (a) for the same crystal orientation as that in Fig. 1 and (b) after rotating the crystal by 180° about the normal to the surface. The measurements were performed using Cu$K_{\alpha 1}$ radiation in the Bragg geometry for $(311)_{3C}$ reflection.

(region II) is the 6H-SiC polytype. It was also established that region I of the epitaxial layer (3C-SiC) represents a couple of twins with a total area of ~25 mm^2, which accounts for approximately half of the total epitaxial growth area. In the topograph of Fig 1, the twins appear as the areas of bright and dark contrast, which is explained by the diffraction conditions selected so as to reveal the twins with a 60° relative misorientation for a (111) habit of the 3C-SiC layer. The epitaxial *p–n* heterostructure was formed by growing a *p*-type SiC layer in the second stage, which was achieved by doping the growth zone with aluminum to an uncompensated acceptor concentration of 2×10^{18} cm^{-3}.

An analysis of the topographs measured on the samples with an upper *p*-SiC layer showed that this layer was formed in the *p–n* epitaxial structure both on the *n*-type 3C-SiC layer in region I and on the *n*-type 6H-SiC layer in region II (Fig. 2a). The *p*-SiC layer image observed in region I showed a well-pronounced band structure oriented in the ⟨110⟩ direction. In the pattern observed upon a 180° rotation, this structure was clearly manifested only in one of the twins (Fig. 2b). As for the *p*-SiC layer formed over region II, this area exhibited alternating areas with dark and bright contrast that was evidence of a small-twin structure of the epitaxial layer.

Thus, the results of the X-ray diffraction and *C–V* measurements showed that epitaxial growth on the 6H-SiC substrate led to the formation of a (*p*)3C-SiC–(*n*)3C-SiC homopolytype *p-n* structure in region I and a (*p*)3C-SiC–(*n*)6H-SiC heteropolytype *p-n* structure in region II.

For evaluating the integral structure perfection in the epitaxial layers grown over regions I and II, we have studied the widths (determined as the full width as half maximum, FWHM) of the X-ray diffraction reflection curves measured with a two-crystal diffractometer using the Cu$K_{\alpha 1}$ radiation. The FWHM values for a 5-μm-thick *n*-SiC epitaxial layer were 17.9″ (seconds of arc) for reflection (111) corresponding to the 3C-SiC polytype (region I) and 19.1″ for reflection (0006) corresponding to the 6H-SiC polytype (region II). The insignificant increase in the FWHM values for the epitaxial layers as compared to the halfwidths (~12″) determined for individual crystals of the 6H and 3C polytypes can be explained by the substrate bending caused by the initial growth of a twinned epitaxial layer. After the *p*-SiC layer growth, the FWHM values in region I were 34″ and 26″ for the reflections (111) and (0006) corresponding to the 3C and 6H polytypes, respectively, the corresponding values in region II with a heteropolytype structure being 13.2″ and 12″. These data are indicative of a high structure perfection in the epitaxial layers studied.

In order to estimate the local structure perfection in the epitaxial films and to reveal the heteropolytype boundary, we examined the cross section of a (*p*)3C-SiC–(*n*)6H-SiC epitaxial heterostructure by transmis-

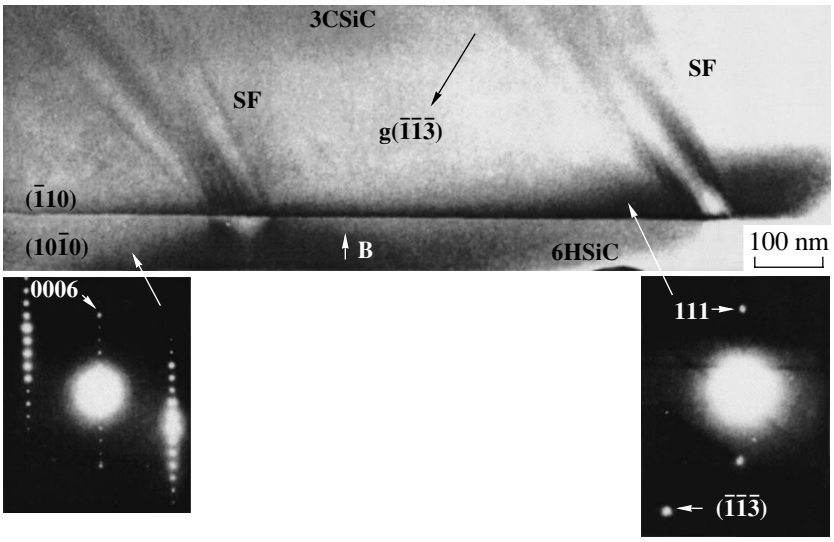

Fig. 3. TEM image of the cross section of an (*p*)3C-SiC–(*n*)6H-SiC epitaxial heterostructure: (B) boundary between 3C and 6H polytypes; (SF) stacking faults; g(-1-1-3) is the diffraction vector. The insets show the electron microdiffraction pattern corresponding to the regions indicated by arrows.

sion electron microscopy (TEM). A sample was thinned by sputtering with an argon ion beam (U = 5 kV, I = 2 μA). Figure 3 shows a TEM image of the cross section of this heterostructure. An analysis of the corresponding electron microdiffraction patterns confirmed that an epitaxial layer of the 3C-SiC polytype was formed above the initially grown epitaxial layer of the 6H-SiC polytype. The TEM image shows a sharp boundary between polytypes, which serves as a site of nucleation of the stacking faults (SF in Fig. 3) propagating into the epitaxial layers.

Thus, the results of our investigation demonstrate the possibility of obtaining a heteropolytype epitaxial structure (*p*)3C-SiC–(*n*)6H-SiC by sublimation deposition in vacuum. The electrical characteristics of these heterostructures, including the *p*–*n* junction parameters will be reported in the following publication.

Acknowledgments. This study was supported by the Russian Foundation for Basic Research, projects no. 00-02-16688 and 01-02-17657).

REFERENCES

1. A. R. Verma and P. Krishna, *Polymorphism and Polytypism in Crystals* (Wiley, New York, 1966; Mir, Moscow, 1969).
2. F. Bechstedt, P. Kackell, A. Zywietz, *et al.*, Phys. Status Solidi B **202**, 35 (1997).
3. Yu. A. Vodakov, G. A. Lomakina, and E. N. Mokhov, Fiz. Tverd. Tela (Leningrad) **24**, 1377 (1982) [Sov. Phys. Solid State **24**, 780 (1982)].
4. K. Vakhner and Yu. M. Tairov, Fiz. Tverd. Tela (Leningrad) **12**, 1543 (1970) [Sov. Phys. Solid State **12**, 1213 (1970)].
5. Yu. A. Vodakov, E. N. Mokhov, A. D. Roenkov, and M. M. Anikin, Pis'ma Zh. Tekh. Fiz. **5**, 367 (1979) [Sov. Tech. Phys. Lett. **5**, 147 (1979)].
6. N. S. Savkina, A. A. Lebedev, D. V. Davydov, *et al.*, Mater. Sci. Eng. B **61-62**, 165 (1999).
7. D. V. Davydov, A. A. Lebedev, A. S. Tregubova, *et al.*, Mater. Sci. Forum **338-342**, 221 (2000).
8. A. N. Andreev, N. Yu. Smirnova, A. S. Tregubova, *et al.*, Fiz. Tekh. Poluprovodn. (St. Petersburg) **31** (3), 285 (1997) [Semiconductors **31**, 232 (1997)].

Translated by P. Pozdeev

Technical Physics Letters, Vol. 27, No. 12, 2001, pp. 1055–1057. Translated from Pis'ma v Zhurnal Tekhnicheskoĭ Fiziki, Vol. 27, No. 24, 2001, pp. 64–70.

Permanent-Magnet Trap for Ultracold Neutron Storage

V. F. Ezhov[a], B. A. Bazarov[b], P. Geltenbort[c], N. A. Kovrizhnykh[d], G. B. Krygin[a,*], V. L. Ryabov[a], and A. P. Serebrov[a]

[a] *St. Petersburg Institute of Nuclear Physics, Russian Academy of Sciences, Gatchina, Leningrad oblast, Russia*
[b] *DOMEN Research Institute, St. Petersburg, Russia*
[c] *Max von Laue–Paul Langevin Institute, Grenoble, France*
[d] *Efremov Institute of Electrophysical Equipment, St. Petersburg, Russia*
* *e-mail: krygin@pnpi.spb.ru*

Received June 6, 2001; in final form, August 2, 2001

Abstract—The design of a permanent-magnet trap for ultracold neutron (UCN) storage is described. This trap excludes neutron collisions with the walls and, hence, eliminates anomalous losses. Used in the experiments on the neutron lifetime determination such UCN traps remove the main systematic error related to the anomalous neutron losses on the walls. © *2001 MAIK "Nauka/Interperiodica".*

In recent years, considerable progress has been achieved in the experiments on determining the neutron halflife. This was provided by using the basic property of ultracold neutrons (UCNs), according to which these neutrons can be stored in closed vessels. Presently, the value averaged over all data reported in the literature amounts to $\tau_{1/2} = 886.7 \pm 1.9$ s [1]. However, a further increase in the experimental accuracy is hindered by a systematic error related t the presence of anomalous UCN losses upon reflection from the container walls. The nature of this phenomenon is still not completely clear, which gives little hope for an increase in the accuracy of traditional experiments in the nearest future.

However, in the very early days upon the discovery of UCNs, Vladimirskiĭ [2] considered the possibility of UCN storage in magnetic traps. In such a system, UCNs possessing a certain polarization are reflected from a magnetic barrier and, hence, do not strike the walls. Therefore, the use of magnetic traps may principally eliminate the problem of anomalous losses. Thus, the problem reduces to creating a magnetostatic system in which the magnetic field strength increases in all directions.

Such traps are widely used in the atomic physics. The most known design is offered by traps of the Ioffe–Pritchard type [3, 4]. This device comprises a magnetic quadrupole, creating a reflecting barrier in the radial direction, and two gate coils at the quadrupole ends creating reflecting gradients on the quadrupole axis near edges. The particle admission and extraction can be controlled by switching current in one of the gate coils.

In application to UCNs, a system of this type was designed and constructed in Los Alamos [5]. The main difficulty in creating a UCN trap is related to the fact that the magnetic moment of a neutron is lower by three orders of magnitude as compared to that of an atom. Accordingly, the magnetic fields necessary to hold UCNs must be three orders larger. In the Los Alamos system [5], the magnetic trap implemented superconductor-based magnets.

However, the superconductor-based magnetic systems possess two significant disadvantages. The first is a relatively slow current variation. As a result, it takes a too long time to close the inlet hole. For this reason, designers of the Los Alamos system refused from using inlet and outlet holes and used to generate UCNs immediately inside the magnetic trap by means of thermal neutron scattering on a superfluid helium film covering the trap walls.

The second disadvantage is a relatively small volume of superconductor-based magnetic systems, since the statistical accuracy of the experimental neutron lifetime determination depends primarily on the trap volume. An increase in the superconductor-based magnetic system volume would lead to enormous growth of the cost of experiments. The volume of the Los Alamos trap was as small as 0.28 dm^3 (diameter, 3 cm; length, 40 cm) at a magnetic barrier of 1.1 T. For a UCN number density of 1.8 ± 0.3 cm^{-3}, the total number of trapped UCNs was 400 ± 65 per cycle. From a practical standpoint, this system design is overcomplicated, since the magnetic systems employing nonsuperconducting elements allow the same magnetic field strengths to be obtained in traps of a significantly greater size. Moreover, using modern magnetic materials, it is possible to create UCN traps with the same magnetic field strength and greater volume based on permanent magnets.

The magnetic potential $\boldsymbol{\mu} \cdot \mathbf{B}$ must correspond to a neutron energy of 0.6×10^{-7} eV/T (for comparison, the nuclear potential for beryllium is equivalent to 2.5×10^{-7} eV). Thus, the magnetic barrier with a height of

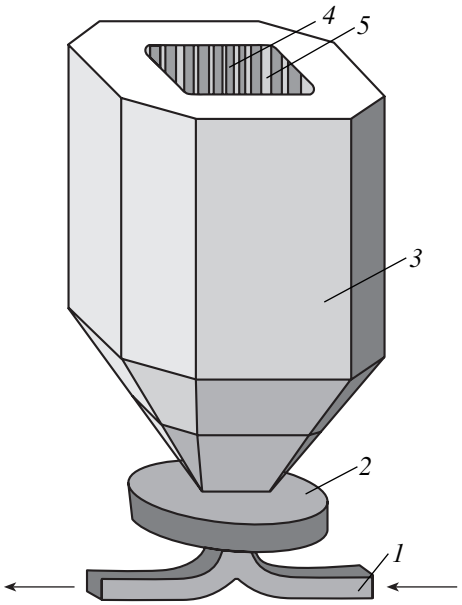

Fig. 1. A general schematic diagram of the permanent-magnet UCN trap: (*1*) neutron guides; (*2*) gate coil; (*3*) magnet yoke; (*4*) permanent magnets; (*5*) magnetic guide.

1 T reflects neutrons possessing a certain polarization up to a velocity of 3.4 m/s. The force acting upon the magnetic moment of a particle moving in an inhomogeneous magnetic field is

$$F = -\nabla U = \nabla(\boldsymbol{\mu} \cdot \mathbf{B}) = \pm\mu\nabla|\mathbf{B}|,$$

where the plus and minus signs refer to the cases of the magnetic moment oriented along the magnetic field and in the opposite direction, respectively. Let us estimate the possible magnitude of a magnetic field gradient reflecting UCNs. The magnetic moment precession in the field is described by the Bloch equation

$$\frac{d\boldsymbol{\mu}}{dt} = \gamma_n \boldsymbol{\mu} \times \mathbf{B},$$

where $\gamma_n = 1.83 \times 10^8$ s^{-1} T^{-1} is the gyromagnetic ratio. The spin of a neutron moving at a velocity v in the magnetic field will retain the orientation provided that the following adiabaticity condition is obeyed [6]:

$$\gamma_n B \gg (dB/dt)/B = v \cdot \nabla|B|/B.$$

For $B = 1$ T, a field gradient of $\nabla B = 1$ T/mm, and a neutron velocity of $v = 3.4$ m/s, the adiabaticity condition is obeyed to within $1.83 \times 10^8 \gg 3.4 \times 10^3$. Evidently, a special point only corresponds to the site where the magnetic field turns zero. At this point, the adiabaticity condition is violated and the magnetic moment projection onto the magnetic field direction may change. Vladimirskiĭ [2] estimated the probability of a nonadiabatic reversal of the neutron spin under the conditions when one field component (H_z) is constant and the other (H_x) performs rapid rotation. In this case, the neutron spin reversal probability is

$$w = e^{-\pi\omega\tau},$$

where $\omega = \mu H_z/\hbar$ is the neutron spin precession frequency about the H_z direction and $\tau = H_z/\dot{H}$ is the effective time of the magnetic field rotation. For a neutron performing a large number N of passages at the points of zero magnetic field or rapid field rotation, the adiabaticity condition will be obeyed provided that $N\omega \ll 1$. For a minimum magnetic field strength, we obtain the condition

$$\pi\mu H_{z\min}^2/\hbar|\dot{H}| > \ln N.$$

Thus, in any particular case, we may select a value of $H_{z\min}$ such that the nonadiabatic spin reversal can be ignored.

From the economic standpoint, the most favorable magnetic system design is that in which the magnetic field strength decays over a minimum distance. This would provide for a decrease in the energy (stored in the magnet) required for creating the necessary field strength and, hence, for a reduction in the permanent-magnet trap weight and cost. Moreover, this leads to an increase in the effective volume of UCN storage.

In the atomic physics, the problem of reflecting atoms from a magnetic barrier is frequently solved by using magnetic planes in periodic magnetic structures magnetized along the surface [7]. At these planes, the magnetic field decays by the exponential law $\exp(-kx)$, where x is the distance and k is a characteristic period of the structure. In the structures employed for experiments on the reflection of atoms, the k value may reach up to a few microns. Accordingly, the structures with a period on the order of several millimeters can be used in the experiments with UCNs. The calculation showed that systems employing the modern magnetically hard materials readily allow obtaining a field strength of $B = 1$ T at the reflecting wall with a field gradient of $\nabla B = 1$ T/mm.

Thus, let us summarize the main requirements to the experimental UCN trap setup:

(i) The magnetic trap height is determined by the gravitational potential (i.e., by the height above which the neutron of a given energy cannot rise in the gravitational field). For this reason, there is no sense in creating systems with a height exceeding 60 cm. At a sufficiently large height, there is no need for the upper lid.

(ii) There should be no points with zero magnetic field strength inside the magnetic trap.

(iii) The neutrons must be admitted in and extracted from the trap through a weak magnetic field region. Upon admitting neutrons, the field strength is increased and the UCNs are trapped.

(iv) Using gradually decreasing field for the neutron extraction, it is possible to measure the energy spectrum of stored neutrons.

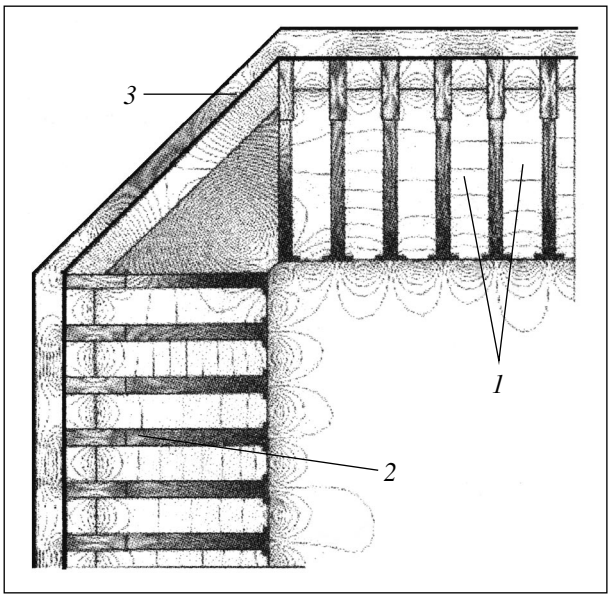

Fig. 2. Element of the UCN trap cross section: (*1*) permanent magnets; (*2*) magnetic guide; (*3*) closing yoke.

Figure 1 gives a general schematic diagram of the proposed magnetic trap. Figure 2 shows a quarter of the cross section. The trap comprises a vertical vessel with a almost square cross section of the UCN storage cavity. The neutrons are admitted in and extracted from the trap via a hole in the bottom. The magnetic field in this hole region is created by a gate coil. In order to eliminate the points of zero magnetic field inside the trap volume, the magnetic field of the gate coil is closed via an external magnetic guide through the upper part and the internal cavity of the trap. As a result, a vertical magnetic field component appears in the whole trap volume. Since the magnetic field of the walls is closed in the horizontal plane, no magnetic field zeros can take place in the trap. The whole system is placed into a vacuum.

The trap volume is about 20 dm^3. For a neutron number density of 5 cm^{-3}, this provides for the storage of up to 10^5 neutrons. The presence of a controlled magnetic barrier closing the entrance allows the stored UCN spectrum to be purified from over-barrier neutrons. By varying the current in the gate coil, it is possible to control the boundary energy of stored neutrons, which is important in searching for the possible systematic effects.

Acknowledgments. This study was performed within the framework of an experiment on the adiabatic cooling of atomic hydrogen, which is supported by the Russian Foundation for Basic Research project no. 99-02-17378.

REFERENCES

1. D. E. Groom *et al.* (Particle Data Group), Eur. Phys. J. C **15** (1-4), 1 (2000).
2. V. V. Vladimirskiĭ, Zh. Éksp. Teor. Fiz. **39** (4), 1062 (1960) [Sov. Phys. JETP **12**, 740 (1960)].
3. T. H. Bergeman, P. McNicholl, J. Kycia, *et al.*, J. Opt. Soc. Am. B **6**, 2249 (1989).
4. T. H. Bergeman, G. Erez, and H. Metcalf, Phys. Rev. A **35**, 1535 (1987).
5. P. R. Huffman, C. R. Brome, J. S. Butterworth, *et al.*, Nature **403**, 62 (2000).
6. A. Abragam, *The Principles of Nuclear Magnetism* (Clarendon, Oxford, 1961; Inostrannaya Literatura, Moscow, 1963).
7. E. A. Hinds and I. G. Hughes, J. Phys. D **32**, R119 (1999).

Translated by P. Pozdeev

Technical Physics Letters, Vol. 27, No. 12, 2001, pp. 1058–1061. Translated from Pis'ma v Zhurnal Tekhnicheskoĭ Fiziki, Vol. 27, No. 24, 2001, pp. 71–78.

The Interaction of Electromagnetic Radiation with a Plasma Stream of a Space Vehicle Electrojet Thruster

I. P. Kozlov

Moscow State Aviation Institute (Technical University), Moscow, Russia

Received July 24, 2001

Abstract—The interaction of an electromagnetic wave with a plasma stream of a space vehicle electrojet thruster was studied within the framework of the plane- and spherical-layer solid dielectric models. The problem of electromagnetic compatibility of the space vehicle radio systems is significantly complicated by the predicted phenomenon, whereby a solution in the vicinity of a zero permittivity may qualitative change with small variations of the problem parameters. The proposed theory provides for an exact solution of the problem of electromagnetic wave diffraction on two bodies. The results of calculations are presented. © *2001 MAIK "Nauka/Interperiodica".*

Development of the space vehicle technologies leads to the wider use of electrojet thrusters characterized by a high specific thrust. In connection with this, it is important to study the effect of a plasma jet emitted from the thruster on the radio systems of the space vehicle. A cold jet plasma can be considered within the framework of a solid dielectric model [1], in which the permittivity ε becomes zero at a certain critical plasma concentration. The existence of this critical point significantly complicates the problem of compatibility of the space vehicle radio systems (antennas) in the presence of a jet plasma, especially in view of increasing engine thrust.

Previously, the problem was studied in the case of an "almost" normal ($\theta_1 \ll 1$) incidence of a plane electromagnetic wave onto a plane-layer dielectric. The analysis revealed qualitative dependence of a solution near the point of zero ε on small $\mathrm{Im}(\varepsilon)$ and θ values (the solution at $\varepsilon = 0$ is considered as a limiting transition) [2–4]. In this study, the curvature of the ε = const surface is taken into account by considering a dielectric at the point of $\varepsilon = 0$ as an axisymmetric body composed of noncentrosymmetrically embedded homogeneous spherical layers (Fig. 1). A plane wave is incident onto this sphere with a radius r_1 from a homogeneous space with $\varepsilon = \varepsilon_1$. The wave is incident at an angle $\theta_1 \ll 1$ and is polarized in the plane of incidence. The solution of this diffraction problem can be formalized and markedly simplified by a previously developed method [5, 6] of the wave amplitude transformation with the variables separated in the spherical coordinate system.

Spherical layer geometry. Let the field in the *i*th layer ($\varepsilon = \varepsilon_i$) between spherical surfaces with the radii $r = r_i$ and r_{i+1} (Fig. 1) be described in the local coordinates centered at O_s ($s = \pm 1$) by unknown amplitudes of the electric (A_{nm}^{si}, B_{nm}^{si}, C_{nm}^{si}, D_{nm}^{si}) and magnetic ($\bar{A}_{nm}^{si}$, $\bar{B}_{nm}^{si}$, $\bar{C}_{nm}^{si}$, $\bar{D}_{nm}^{si}$) waves. The centers O_{-1} and O_{+1} are spaced by l_i ($\Delta_i = \sqrt{\varepsilon_i}\, k l_i$, where $k = 2\pi/\lambda$ and λ is the wavelength in vacuum). For a transition between the two coordinate systems centered at O_s, the wave

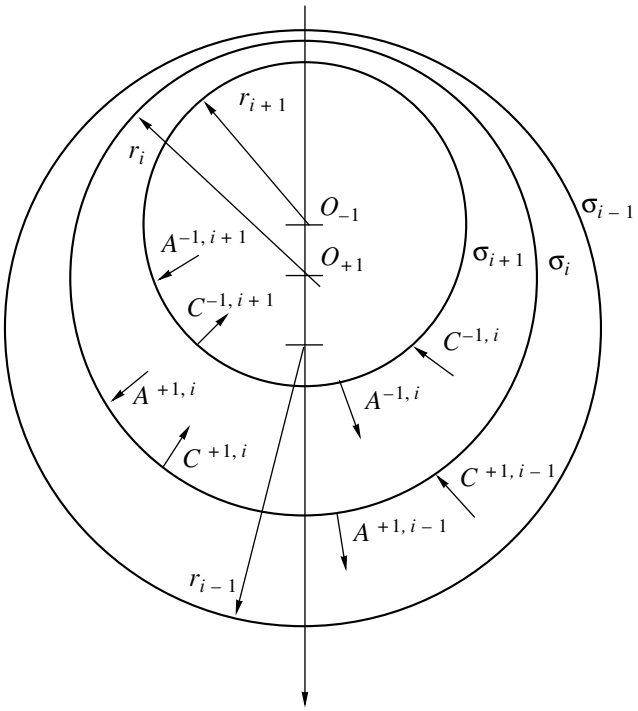

Fig. 1. Inhomogeneous dielectric ball.

1063-7850/01/2712-1058$21.00

amplitudes transform according to the following relationships [6]:

$$\begin{aligned} A_{nm}^{si} &= \sum_{j=m}^{\infty} \left\{ \beta_{nmj}^{-s} \; A_{jm}^{-si} + \frac{1}{w_i} \bar{\beta}_{nmj}^{-s} \; \bar{B}_{jm}^{-si} \right\}, \\ \bar{B}_{nm}^{si} &= \sum_{j=m}^{\infty} \left\{ \beta_{nmj}^{-s} \; \bar{B}_{jm}^{-si} - \frac{1}{w_i} \bar{\beta}_{nmj}^{-s} \; A_{jm}^{-si} \right\}, \\ C_{nm}^{si} &= \sum_{j=m}^{\infty} \left\{ \gamma_{nmj}^{-s} \; C_{jm}^{-si} + \frac{1}{w_i} \bar{\gamma}_{nmj}^{-s} \; \bar{D}_{jm}^{-si} \right\}, \\ \bar{D}_{nm}^{si} &= \sum_{j=m}^{\infty} \left\{ \gamma_{nmj}^{-s} \; \bar{D}_{jm}^{-si} - \frac{1}{w_i} \bar{\gamma}_{nmj}^{-s} \; C_{jm}^{-si} \right\}, \end{aligned} \quad (1)$$

where $n, m = 0, 1, 2, \ldots$ ($n \neq 0$, $m \leq n$) and $w_j = \sqrt{1/\varepsilon_j}$; expressions for the coefficients β_{nmj}^{s}, γ_{nmj}^{s}, $\bar{\beta}_{nmj}^{s}$, and $\bar{\gamma}_{nmj}^{s}$ can be found in [6]. Transformation (1) describes the relationship between electric and magnetic waves upon a shift of the coordinate origin. Assuming continuity of the tangential components of the fields on the surface $r = r_i$, we readily obtain the boundary conditions for the electric wave amplitude:

$$\begin{aligned} C_{nm}^{si} &= c_n^i A_{nm}^{si+1} + e_n^i C_{nm}^{si+1}, \\ A_{nm}^{si} &= a_n^i A_{nm}^{si+1} + b_n^i C_{nm}^{si+1}, \quad i = 1, 2, \ldots, I; \end{aligned} \quad (2)$$

where a_n, b_n, c_n, and e_n are the coefficients derived in [7]. For $i = 1$, the unknown amplitudes of the incident waves in (2) should be replaced by amplitudes of the external current waves. Upon the wave amplitude transformation (1) after passing from one local coordinate system to another, the incomplete system (2) for the electric waves and an analogous system for the magnetic waves are supplemented so as to become complete. A solution to the complete system can be obtained by the truncation method. Using the method of transreflections developed in [5], it is possible to perform calculations for the objects with dimensions up to several wavelengths.

Plane layer geometry. Consider a plane electromagnetic wave normally incident onto a nonabsorbing plane-parallel layer ($z_1 < z < z_N$) in which the smooth function $\varepsilon(z)$ decreases to zero (Fig. 2). Let $\varepsilon_1 = \varepsilon(z_1)$, $\varepsilon_N = \varepsilon(z_N)$, and $\varepsilon_1 > \varepsilon_N > 0$; in the region $z < z_1$ ($\varepsilon = \varepsilon_1$), the system features incident and reflected wave, while the region $z > z_N$ ($\varepsilon = \varepsilon_N$) contains the transmitted wave.

According to the proposed solution scheme, the layer (ε_1, ε_N) is divided into homogeneous sublayers of variable thickness such that $\delta^2 = \varepsilon_n/\varepsilon_{n+1} = \text{const}$ ($\Delta z_n = z_{n+1} - z_n \longrightarrow 0$ for $\varepsilon \longrightarrow 0$) as depicted by curve *3* in Fig. 2. In the vicinity of $\varepsilon = 0$, the layer is replaced by a nonlinear with

$$gr(\varepsilon_L) = \text{const} \quad (3)$$

and the reflection coefficient R_L, where $gr(\varepsilon) = -\alpha/\varepsilon^{3/2}$

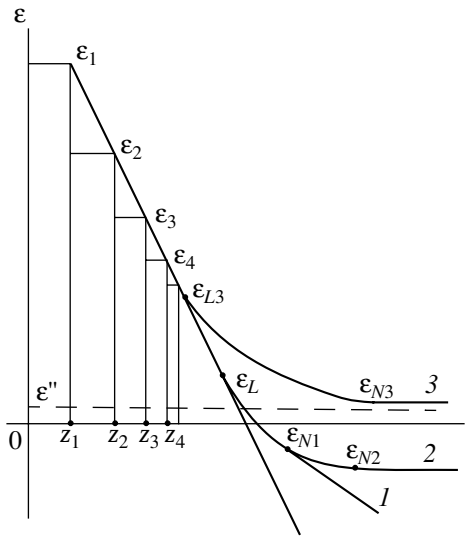

Fig. 2. Permittivity profile of a linear layer matched with nonlinear in the vicinity of $\varepsilon = 0$.

and $\alpha = d\varepsilon/d(kz) < 0$. For the layer (3), the problem can be solved exactly in elementary functions. This solution is adopted as a long-wave approximation for the problem under consideration at $-gr(\varepsilon) > 20$ [2]. As a result, we obtain the following recurrent formula for the reflection coefficient of the total layer [2]:

$$R^n \exp(2i\rho_n) = R_0^n = \frac{r + R_0^{n+1} \exp(i\Delta\rho_{n+1})}{1 + rR_0^{n+1} \exp(i\Delta\rho_{n+1})}, \quad (4)$$

where $n = 1, 2, \ldots, L-1$; $R_0^L = R_L$; $\Delta\rho_L = 0$; $\rho_n = \sqrt{\varepsilon_n}\, kz_n$, $r = \dfrac{(\delta - 1)}{(\delta + 1)}$, and $\Delta\rho_{n+1} = \dfrac{2(\delta^2 - 1)}{\delta^{3n} gr(\varepsilon_1)}$. The electric field strength E can be determined by the reverse "passage" [4]. The system obeys the similarity principle for plane-parallel layers possessing equivalent reflection coefficients $R_0^N = R\{gr(\varepsilon_1), \varepsilon_1/\varepsilon_N\}$ and equal fields at $\varepsilon \sim 0$. In the general solution for the E wave, $\varepsilon'(z) = \varepsilon - i\varepsilon''$, $\varepsilon'' = \text{const}$, and $\varepsilon_0 = \varepsilon_1' \sin\theta_1$ (ε_0 is a real quantity). In similar layers, the values of ε_0, ε'', $\varepsilon_1/\varepsilon_N$, and $gr(\varepsilon_n')$ = $-\alpha_n/(\varepsilon_n')^{3/2}$ ($n_n = 1, 2, \ldots, N-1$) are equal, while the α_n and ε_n' values are different. For a linear semiinfinite nonabsorbing layer ($\varepsilon < \varepsilon_1$) for $\theta = 0$ (the main solution), a solution is obtained from the general solution by a limiting transition for $\varepsilon_L \longrightarrow 0$ (in Fig. 2, this solution is depicted by curve *1*, curves *2* and *3* representing the approximations to curve *1*). The energy flux density of

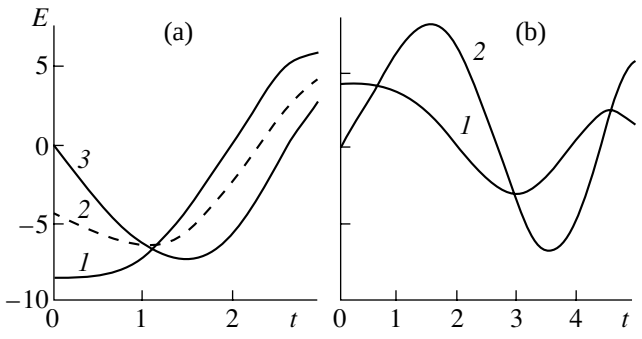

Fig. 3. Electric field strength $E(t)$ ($t = \varepsilon/\varepsilon_1[gr(\varepsilon_1)]^{-2/3}$) calculated for $\varepsilon'' = 0$, $\theta_1 = 0$, $gr(\varepsilon_1) = 0.001$ and $\varepsilon_1 = 0.1327354$ (a) and 0.1327356 (b): (*1*) exact solution; (*2*) approximate solution using one of the two Airy functions; (*3*) exact solution for the ideal conducting plane at $\varepsilon = 0$. The position of zero field point depends on small variations of the layer parameters.

the transmitted waver $S_L \longrightarrow 1$ and it is possible that $E \longrightarrow \infty$ for $\varepsilon_L \longrightarrow 0$. This property reveals a special qualitative feature of the solution in the vicinity of the point $\varepsilon = 0$. The Poynting vector direction for the transmitter *E* wave is determined by the formula

$$\cot\Phi_{nE} = \mathrm{Re}(\gamma_n^*\sqrt{\gamma_n - 1})/\mathrm{Re}(\gamma_n^*),$$

where $\gamma_n = \varepsilon_n'/\varepsilon_0$.

This direction coincides with the *z* axis for $\varepsilon''/\varepsilon_0 \gg 1$ and with the *y* axis for $\varepsilon''/\varepsilon_0 \ll 1$ (laminar energy flow). For $\varepsilon'' = 0$, there are two limiting cases for the wave propagating along the *z* axis for $\delta^{2n}(\theta_1)^2 \ll 1$ ($r_{nE} \approx -(\delta - 1)/2$) and along the *y* axis for $\delta^{2n}(\theta_1)^2 \gg 1$ (($r_{nE} \approx (\delta - 1)/2$). Since the r_{nE} value changes sign in the case of $\varepsilon''/\varepsilon_0 \ll 1$, we may assume that $R_E \approx 0$ at $\varepsilon = \varepsilon_p$. This sublayer contains only a transmitted *E* weave, for which $\varepsilon_0 = \varepsilon_p\sin^2\theta_p$. Provided that $\varepsilon''/\varepsilon_0 < a$ ($a \approx 0.1$), the wave energy can be converted into that of a surface *E* wave. In this case, the estimates (to within the order of magnitude) are as follows. In the shortwave approximation, $\varepsilon_p \approx 0.01(\alpha_1)^{2/3}$ at $R = 0.1$ [3] and then $\varepsilon'' \approx 10^{-3}(\alpha_1)^{2/3}$. As the ε'' value increases, the wave energy flow becomes turbulent.

A critical point at ε = 0; calculation results. The properties established for an "almost" plane-parallel layer lead to a bifurcation at $\varepsilon \sim 0$, whereby the solution of the physical problem is qualitatively dependent on small parameters ε'', ε_0, $1/r_i$, and l_i (with an allowance for the sign) for $\varepsilon'' \ll 0.1(\alpha_1)^{2/3}$. An allowance for the last two parameters leads to a relationship between the waves with different polarizations in (1).

In the plane-layer approximation (applicable for $\sqrt{|\varepsilon_n'|}\,kr \gg 1$), the ray exhibits "breakage" on a local level (within the incident ray limits) for $\varepsilon''/\varepsilon_0 \ll 1$: the wave is "pumped" into the layer with $\varepsilon \sim 0$ and propagates there as a surface *E* wave (the "pumping" problem can be considered as nonstationary); for $\varepsilon''/\varepsilon_0 \gg 1$, the wave "penetrates" into the region of $\varepsilon < 0$ ($\theta \sim 0$). The surface *E* wave is formed on the while surface $\varepsilon = \mathrm{const}$ (even outside the incident ray where the plane-parallel approximation is valid). For the main solution, Fig. 3 shows the results of calculations of the field *E* in comparison to a solution obtained using the Airy functions in [8], where one of the Airy functions was ignored because of a small jump in the derivative $d\varepsilon/dz$. The results of these calculations indicate that the exact solution (and, hence, both Airy functions) has to be employed in the vicinity of zero ε.

The quantitative criteria of applicability of the shortwave [3] and longwave approximations, as well as the condition of the appearance of a surface wave and the criterion of applicability of the model of normally incident plane wave [9], allow the calculations to be performed with a preset accuracy, which is necessary in view of the revealed anomaly in the solution to the wave equation. A description of the fields in a cold plasma near the critical concentration point, it is necessary to take into account the curvature of the surface $\varepsilon = \mathrm{const}$ and the microwave absorption. Further analysis will take into account the constant magnetic field (within the framework of the perturbation theory [8]) and the Landau damping.

Conclusion. The results of this investigation were implemented in the design of antennas for space vehicles [10]. The proposed theory of an "almost" plane-parallel layer can be applied to solving the internal problem (upon introducing the waveguide walls). The presence of a critical point (or a jump in ε) in the electrojet thruster channel, the possible energy conversion at this level, and the corresponding electron density variations provide an explanation for the experimentally observed resonance cathode heating at $\varepsilon < 0$ (with neglect of the constant electric and magnetic fields, the wave does not enter the layer with $\varepsilon = 0$) and a spontaneous buildup of the intrinsic microwave emission from electrojet thrusters of various types on reaching a maximum power level [11]. Note that the transformations of waves with different polarizations in a spherical-layer medium would complicate the polarization decoupling of the transmitting and receiving antennas.

REFERENCES

1. I. B. Safonov, Radiotekh. Élektron. (Moscow) **38** (3), 91 (1993).

2. I. P. Kozlov, Zh. Tekh. Fiz. **69** (8), 5 (1999) [Tech. Phys. **44**, 873 (1999)].
3. I. P. Kozlov, Radiotekh. Élektron. (Moscow) **42** (2), 142 (1997).
4. I. P. Kozlov, Pis'ma Zh. Tekh. Fiz. **26** (14), 28 (2000) [Tech. Phys. Lett. **26**, 605 (2000)].
5. I. P. Kozlov, Radiotekh. Élektron. (Moscow) **46** (2), 180 (2001).
6. I. P. Kozlov, Izv. Vyssh. Uchebn. Zaved., Radiofiz. **18** (7), 997 (1975).
7. I. P. Kozlov, in *Propagation and Diffraction of Electromagnetic Waves* (Mosk. Fiz.-Tekh. Inst., Moscow, 1993), pp. 104–113.
8. V. L. Ginzburg, *The Propagation of Electromagnetic Waves in Plasmas* (Nauka, Moscow, 1967; Pergamon, Oxford, 1970).
9. I. P. Kozlov, Radiotekh. Élektron. (Moscow) **46** (1), 58 (2001).
10. I. P. Kozlov, in *Proceedings of the 26th International Electric Propulsion Congress (IEPC-99), Kitakyushu, Japan, 1999*, p. 229.
11. K. P. Kirdyashev and V. I. Brukhty, Pis'ma Zh. Tekh. Fiz. **27** (11), 36 (2001) [Tech. Phys. Lett. **27**, 457 (2001)].

Translated by P. Pozdeev

Technical Physics Letters, Vol. 27, No. 12, 2001, pp. 1062–1064. Translated from Pis'ma v Zhurnal Tekhnicheskoĭ Fiziki, Vol. 27, No. 24, 2001, pp. 79–84.

The Effect of an Alternating Electric Field on the Liquid Dielectric Convection in a Horizontal Capacitor

B. L. Smorodin

Perm State University, Perm, Russia

e-mail: smorodin@psu.ru

Received July 19, 2001

Abstract—The electroconvective instability in a low conducting nonuniformly heated liquid occurring in an alternating electric field between plates of a horizontal plane capacitor was studied in terms of the equations of electrohydrodynamics for arbitrary field modulation frequencies and various shapes (harmonic and triangular). In the gravitational field, the instability is determined by the interplay of dielectrophoretic and thermogravitational mechanisms. The layer heated from above can feature the parametric instability. In the low-frequency range, a numerical solution to the problem obtained by the Floquet method well agrees with the asymptotic results. © *2001 MAIK "Nauka/Interperiodica".*

Inhomogeneous heating of a low conducting liquid occurring in an electric field may render the equilibrium unstable and lead to the development of motion [1]. On heating from above, the Rayleigh–Benard convection does not arise but the instability may be caused by some other factors such as, for example, the dielectrophoretic instability mechanism [2]. The effect of electric fields on the motion of liquids is employed in the electrohydrodynamic energy converters—devices in which the electric field energy is directly converted into the kinetic energy of a liquid flow. Another technical application is related to the possibility of intensifying or suppressing the heat and mass transfer in high-voltage devices and, in some cases, to the ability of controlling such processes [3].

The effect of vibrations and modulated thermal fields on the convection in a liquid was studied in [4, 5]. However, there is another way for acting upon the stability of equilibrium in a liquid dielectric: we may apply an alternating electric field of a finite frequency [6] and study the possibility of a resonance excitation of electroconvective motions in the liquid. This phenomenon is important for the development of various technologies and devices employing electric fields.

Let us study the effect of a periodic field on the convection in the ideal liquid dielectric in a horizontal plane capacitor with a thickness h and the boundary planes heated to different temperatures: $T(-h/2) = 0$, $T(h/2) = \Theta$. The upper boundary potential is assumed to be zero, while the lower boundary potential periodically varies with time by the law $\varphi(-h/2) = Uf(t)$, where $f(t) = f(t + t_f)$ is a periodic function with a period t_f and a frequency $\Omega = 2\pi/t_f$ and U is the standard voltage level. We will consider various shapes of the applied voltage. In the case of a harmonic modulation, the periodic function has the form $f(t) = \eta_1 + \eta_2\cos(2\pi t/t_f)$, where the modulation amplitude η_2 may continuously vary and the term η_1 may take one of the two values: $\eta_1 = 0$ corresponds to the alternating potential difference and $\eta_1 = 1$, to the potential modulated on a constant field background. In the case of a triangular (sawtooth) modulation,

$$f(t) = \begin{bmatrix} -1 + 2t/(0.9t_f), & 0 \le t \le 0.9t_f \\ 10(1.9 - 2t/t_f), & 0.9t_f \le t \le t_f \end{bmatrix}, \qquad (1)$$

the voltage grows according to a linear law over most of the period and then linearly drop to the initial level. The permittivity is assumed to be a linear function of the temperature, $\varepsilon = \varepsilon_0(1 - \beta_\varepsilon T)$, with a positive temperature coefficient β_ε.

In the case when the voltage applied to the capacitor does not exceed a certain critical value, we may ignore the effect of charge injection [7] and write a system of equations for the convection in a liquid dielectric occurring in the gravitational and electric fields with the corresponding boundary conditions (in a dimensionless form):

$$\left(\frac{\partial \mathbf{v}}{\partial t} + \frac{1}{P}(\mathbf{v}\nabla)\mathbf{v}\right) = -\nabla p + \nabla^2\mathbf{v} + \mathrm{Ra}T\mathbf{e} - R_e'E^2\nabla\varepsilon,$$

$$P\frac{\partial T}{\partial t} + (\mathbf{v}\nabla)T = \nabla^2 T, \quad \mathrm{div}\mathbf{v} = 0, \quad \mathrm{div}\varepsilon\mathbf{E} = 0,$$

$$\mathbf{E} = -\nabla\varphi, \quad \mathbf{e} = (0, 0, 1), \quad \varepsilon = 1 - S_\varepsilon T, \qquad (2)$$

$$z = -1/2\colon \mathbf{v} = 0, \quad T = 0, \quad \varphi = f(t);$$

$$z = 1/2\colon \mathbf{v} = 0, \quad T = 1, \quad \varphi = 0.$$

Here p, $\mathbf{v}$, φ, and T are the pressure, velocity, potential, and temperature fields; $\mathbf{E}$ is the electric field strength;

$\mathrm{Ra} = g\beta\Theta h^3/\nu\chi$ is the Rayleigh number; $R'_e = \varepsilon_0 U^2/\nu\chi\rho$ is a dielectrophoretic analog of the Galileo number; $P = \nu/\chi$ is the Prandtl number, $\omega = \Omega h^2/\nu$ is the dimensionless field modulation frequency; $S_\varepsilon = \beta_\varepsilon\Theta$ is a parameter characterizing inhomogeneity of the permittivity; ρ, ν, χ, and β are the density, viscosity, thermal diffusivity, and thermal expansion coefficient of the liquid, respectively; and g is the acceleration of gravity. Note that, in our problem formulation, $\mathrm{Ra} > 0$ corresponds to the case of heating from above. For a weak temperature dependence of the permittivity, we may ignore spatial inhomogeneity of the field amplitude E_0 [2]. The state of quasi-equilibrium is characterized by the following conditions: $v_0 = 0$, $T_0 = 1/2 + z$, $\varphi = (1/2 - z)f(t)$, $E_0 = f(t)$.

Let the quasi-equilibrium to be subject to perturbations of the type $(\mathbf{v}, T, p, \mathbf{E}, \varphi) \sim \exp(ik_x x + ik_y y)$, where k_x and k_y are the wave numbers characterizing the perturbation periodicity in the capacitor plane ($k^2 = k_x^2 + k_y^2$). The amplitudes of perturbations in the vertical velocity w, temperature θ, and potential φ are described by a system of ordinary differential equations with variable coefficients:

$$\frac{\partial \Delta w}{\partial t} = \Delta^2 w - \mathrm{Ra}k^2\theta + k^2 R_e\left(\theta f^2(\omega t) + \frac{\partial \varphi}{\partial z} f(\omega t)\right);$$

$$P\frac{\partial \theta}{\partial t} + w = \Delta\theta; \quad \Delta = \partial^2/\partial z^2 - k^2; \tag{3}$$

$$\Delta\varphi + \frac{\partial \theta}{\partial z} f(\omega t) = 0; \quad R_e = R'_e S_\varepsilon^2;$$

$$z = 0; 1, \quad w = 0, \quad w' = 0, \quad \theta = 0, \quad \varphi = 0,$$

where R_e is the electrical analog of the Rayleigh number. For an arbitrary set of parameters R_e, Ra, ω, k and P, the solutions to system (3) either increase or decrease with time, while the boundary of the stability domain corresponds to a periodic regime. The boundaries of stability were determined by the Floquet method. A periodic solution was found by the Galerkin–Kantorovich method. The spatial basis set was constructed using eigenfunctions of the problem of perturbations in the motionless liquid layer [8].

Figure 1 presents the plots of R_e versus inverse modulation frequency for the alternating ($\eta_1 = 0$) and modulated ($\eta_1 = 1$) fields and different levels of heating. The instability regions are situated above the corresponding curves. The solid lines represent the boundaries of increasing perturbations synchronous with the external action, while dashed lines show the boundaries of subharmonic regimes. The high-frequency limit corresponds to $\omega \geq 100$. At a finite modulation frequency ω, the instability is related to a parametric resonance. For $\mathrm{Ra} = 500$, a minimum of the first resonance region in the alternating field ($\eta_1 = 0$) corresponds to a frequency

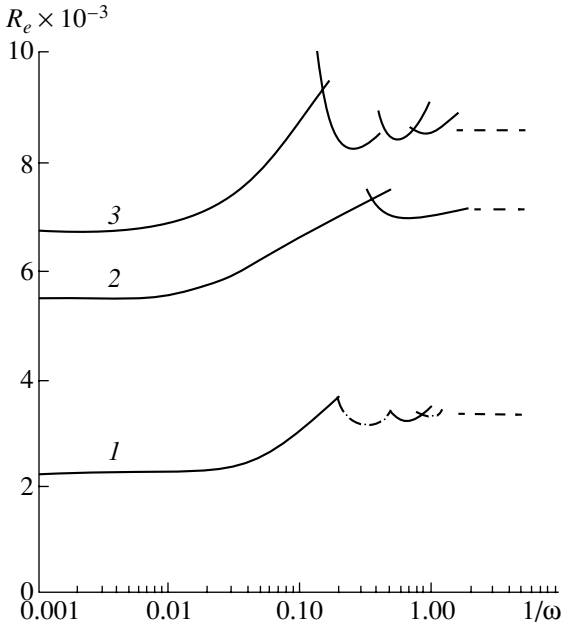

Fig. 1. Harmonic modulation. Boundaries of stability in the plane (R_e, $1/\omega$) for $P = 1$: (*1*) modulated field ($\eta_1 = 1$), $\mathrm{Ra} = 1000$; (*2*) alternating field ($\eta_1 = 0$), $\mathrm{Ra} = 500$; (*3*) alternating field ($\eta_1 = 0$), $\mathrm{Ra} = 1000$.

of $\omega = 1.56$ (at a critical value of the electrical Rayleigh number $R_e = 6931$). Similarly to the case of a constant electric field, a growth of the Rayleigh number [2] leads to an increase in the instability thresholds. Simultaneously, the parametric instability excitation effects become more pronounced and the number of instability regions increases. The resonance frequencies increase with Ra. In the modulated field ($\eta_1 = 1$), the instability thresholds for both high-frequency and parametric modes are lower than those in the alternating field ($\eta_1 = 0$).

As for the limiting case of low frequencies, it should be noted that the zero-order approximation in ω is represented by a family of quasi-static fields. The boundary of stability is determined from the integral relationship

$$\int_0^{2\pi} \lambda_r(R_e, \eta_1 + \eta_2 f(\tau))d\tau = 0, \tag{4}$$

where λ_r is the real part of a complex decrement of the most dangerous mode in the problem concerning the stability of a dielectric liquid in a constant transverse field of a horizontal plane capacitor [2]. The decrement λ is also determined using the Galerkin method. The instability boundaries in the low-frequency limit ($\omega \longrightarrow 0$) are represented by dashed horizontal lines.

The alternating field with a triangular profile, as well as that modulated by a harmonic law with $\eta_1 = 1$, leads to alternation of the regions of synchronous and

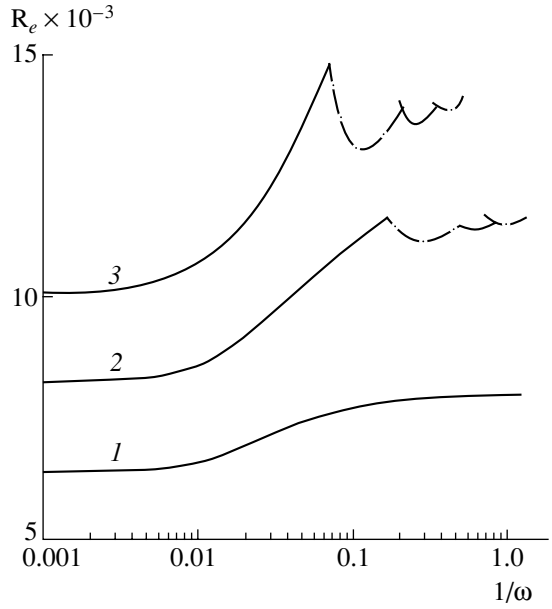

Fig. 2. Triangular modulation. Boundaries of stability in the plane (R_e, 1/ω) for P = 1 and Ra = 0 (*1*), 500 (*2*), and 1000 (*3*).

subharmonic response to the external field variations (Fig. 2). The boundary of stability R_e in the case of triangular modulation lies above the boundary corresponding to a harmonic modulation. This is related to the fact that the onset of convection in the alternating field is determined by the parameter $R_{\text{eff}} = R_e\langle f(\omega t)^2\rangle$, where $\langle f(\omega t)^2\rangle = 1/2$ and 1/3 for the harmonic and triangular modulation, respectively.

Acknowledgments. This study was supported by the Russian Foundation for Basic Research, project no. 00-01-00515.

REFERENCES

1. M. J. Gross and J. E. Porter, Nature **212**, 1343 (1966).
2. R. J. Turnbull and J. R. Melcher, Phys. Fluids **12** (6), 1160 (1969).
3. S. R. Kosvintsev and M. G. Velarde, in *Proceedings of the International Workshop on Electrical Conduction, Convection and Breakdown in Fluids, Sevilla, 1998*, p. 109.
4. G. Z. Gershuni, I. O. Keller, and B. L. Smorodin, Dokl. Akad. Nauk **348** (2), 194 (1996) [Phys. Dokl. **41**, 211 (1996)].
5. B. L. Smorodin and V. S. Shavkunov, Pis'ma Zh. Tekh. Fiz. **22** (3), 1 (1996) [Tech. Phys. Lett. **22**, 91 (1996)].
6. B. L. Smorodin and M. G. Velarde, J. Electrost. **48** (3-4), 261 (2000).
7. S. A. Zhdanov, S. R. Kosvintsev, and I. Yu. Makarikhin, Zh. Éksp. Teor. Fiz. **117** (2), 398 (2000) [JETP **90**, 352 (2000)].
8. G. Z. Gershuni and E. M. Zhukhovitsky, *Convective Stability of Incompressible Fluids* (Nauka, Moscow, 1972).

Translated by P. Pozdeev

Technical Physics Letters, Vol. 27, No. 12, 2001, pp. 1065–1066. Translated from Pis'ma v Zhurnal Tekhnicheskoĭ Fiziki, Vol. 27, No. 24, 2001, pp. 85–89.

Some Features of the Energy Dissipation in the Course of Plastic Deformation of Iron and Niobium

O. P. Maksimkin and M. N. Gusev

Institute of Nuclear Physics, Almaty, Kazakhstan

e-mail: root@iae.nnc.kz

Received July 2, 2001

Abstract—Experimental data on the heat evolution in the course of plastic deformation of technical-purity niobium and iron are reported. Dependence of the dissipated heat Q on the relative deformation ε of Nb and Fe samples deformed in a microcalorimetric cell was traced. The $Q(\varepsilon)$ curve exhibits regions corresponding to a virtually constant rate of the dissipative process ($dQ/d\varepsilon \approx$ const). It is suggested that these regions reflect regular changes in the dislocation substructure and a multistage character of the plastic deformation process in both iron and niobium. *© 2001 MAIK "Nauka/Interperiodica".*

Introduction. In recent years, a deformed metal crystal has frequently been considered as a nonequilibrium self-organizing system and the plastic flow is described in terms of the dissipative structure evolution during deformation in various scales [1, 2]. However, the number of experimental investigations of the laws of dissipative processes accompanying the plastic deformation is still very restricted.

Using the results of calorimetric measurements, we have obtained quantitative estimates of the heat dissipated in bcc metals and the energy stored in these metals in the course of deformation.

Experimental. The flat plates of technical-purity iron and niobium (with dimensions of the working part $10 \times 3.5 \times 0.3$ mm) were annealed for 1 h at 1220 K (Fe) and 1470 K (Nb). Then the samples were deformed by uniaxial tension at a rate of 8.3×10^{-4} s^{-1} at 293 K inside a microcalorimeter cell. This procedure was performed in a setup combining a microtesting machine and a differential Calvet calorimeter, which was specially designed for studying thermal effects accompanying the process of plastic deformation [3]. Upon processing of the simultaneously measured stress–strain diagrams (plotted in the coordinates of force F versus elongation Δl) and DSC thermograms (plotted as the heat evolution rate dQ/dt versus time t), we determined the mechanical characteristics (yield stress σ_y, ultimate strength σ_u, proportional elongation ε_p, and relative elongation at break ε_b) and the energy parameters (deformation work $A = \int F\,dl$, dissipated heat $Q = \int \partial Q/\partial t dt$, and latent energy $E_s = A - Q$). Using special data processing programs, we took into account the thermal inertia of the calorimeter, restored "true" thermograms, and eventually determined the quantities A, Q, and E_s as functions of the relative tensile deformation ε [4].

Results and discussion. Figure 1 shows a typical stress–strain diagram and the plots of energy parameters versus relative deformation; the values of mechanical and integral energy parameters $A(\varepsilon)$, $Q(\varepsilon)$, and $E_s(\varepsilon)$ at break are given in the table. As can be seen from Fig. 1, the ability of materials studied to absorb the energy delivered from outside significantly decreases, while the growth rate (slope) of Q increases.

An analysis of the dissipated heat as a function of the relative deformation (Fig. 2) shows that the $Q(\varepsilon)$ curve displays several regions in which the rate of

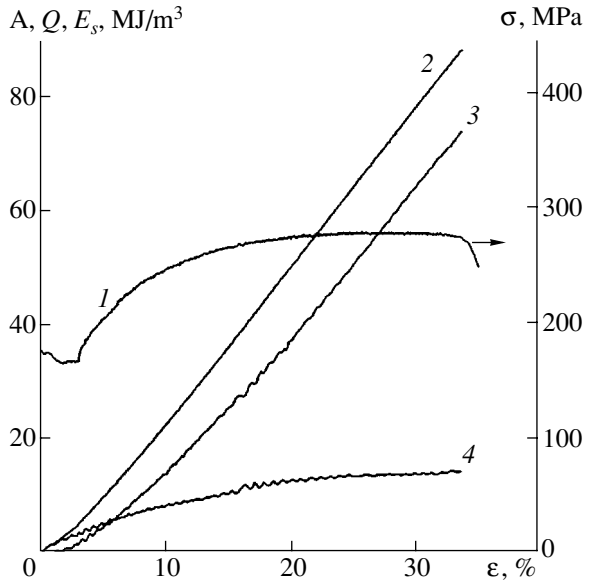

Fig. 1. The experimental plots of (*1*) stress σ and (*2–4*) integral energy parameters A, Q, and E_s, respectively, versus relative deformation ε for armco iron.

1063-7850/01/2712-1065$21.00 © 2001 MAIK "Nauka/Interperiodica"

Mechanical and energy characteristics of niobium and armco iron

Metal, grain size	σ_y, MPa	σ_u, MPa	ε_p, %	ε_b, %	A, MJ/m^3	Q, MJ/m^3	E_s, MJ/m^3
Nb, 3 μm	370	455	15	22	90	68	22
Fe, 20 μm	165	270	31	35	85	71	14

increase in the heat evolution (i.e., slope) is nearly constant $(dQ/d\varepsilon)_i$. This fact suggests that the experimentally measured $Q(\varepsilon)$ curves may provide information on the evolution of the defect structure in the course of crystal deformation and on the stages of plastic deformation.

Indeed, according to [1, 5, 6], an increase in the relative deformation is accompanied by modification of the dislocation structure of a metal. This leads to an increase in the dislocation density and to a change in the mechanism and magnitude of deformation-induced strengthening. In particular, going from deformation stage to another corresponds to a change in the dislocation mean free path L [5]; within the limits of one stage, $L \approx$ const. It was suggested [6] that L is related to the intensity of energy dissipation by an expression of the type $L^{-1} = (dQ \cdot b)/(d\varepsilon \cdot 2E)$, where E is the dislocation tensile stress energy and b is the Burgers vector. This relationship is probably the main reason for the appearance of nearly linear regions in the $Q(\varepsilon)$ curves.

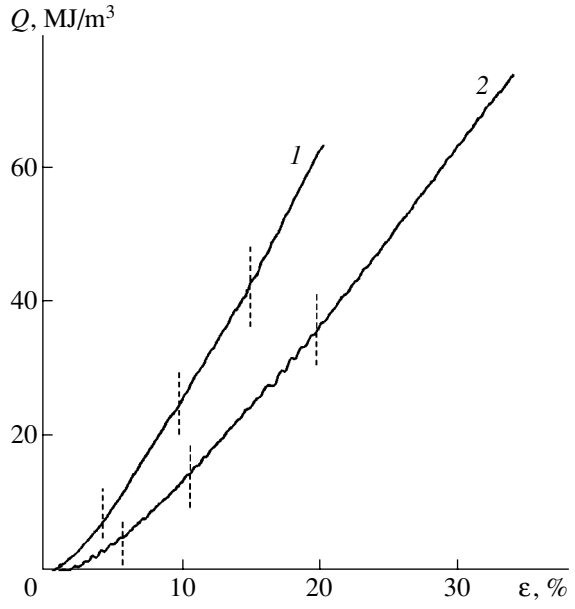

Fig. 2. The plots of dissipated heat Q versus relative deformation for (*1*) niobium and (*2*) armco iron. Dash bars indicate the regions corresponding to different stages of plastic flow in the metals studied.

It would be logical to relate these linear regions to evolution of the dislocation structure and a multistage character of the plastic deformation development in bcc metals. In our case, the first linear region observed in the $Q(\varepsilon)$ curve corresponds to the formation and propagation of the first Lüder's deformation band, while the subsequent regions correspond to stages determined as described in [5].

Conclusion. A new approach has been developed for studying the multistage character of plastic deformation in metals, which is based on the experimental measurement of characteristics of the dissipative processes in deformed samples. Using this method, a multistage character is revealed in the plastic flow of armco iron and niobium.

REFERENCES

1. V. E. Panin, V. I. Danilov, L. B. Zuev, *et al.*, *Structural Levels of Plastic Deformation and Fracture*, Ed. by V. E. Panin (Nauka, Novosibirsk, 1990).
2. V. E. Panin, A. D. Korotaev, P. V. Makarov, *et al.*, Izv. Vyssh. Uchebn. Zaved., Fiz., No. 7, 8 (1998).
3. O. P. Maksimkin, Preprint FTI NAN RK 94-02 (Almaty, 1994).
4. I. V. Astaf'ev and O. P. Maksimkin, Zavod. Lab., No. 1, 44 (1994).
5. V. I. Trefilov, *Strain Hardening and Fracture of Polycrystalline Metals* (Metallurgiya, Moscow, 1989).
6. V. V. Rybin, *Large Plastic Deformations and Fracture of Metals* (Metallurgiya, Moscow, 1986).

Translated by P. Pozdeev

Technical Physics Letters, Vol. 27, No. 12, 2001, pp. 1067–1068. Translated from Pis'ma v Zhurnal Tekhnicheskoĭ Fiziki, Vol. 27, No. 24, 2001, pp. 90–94.

Laser Radiation Confinement at 1.06 μm in Compensated Gallium Arsenide

A. G. Kalintsev, O. P. Mikheeva, and A. I. Sidorov

Institute of Laser Physics, St. Petersburg, Russia

Received June 18, 2001

Abstract—Experimental data on the YAG:Nd laser radiation (λ = 1.06 μm) confinement by self-defocusing in compensated GaAs are reported. It is demonstrated that low-threshold confinement at an energy threshold below 10 pJ is possible for a 10 ns laser pulse width. © *2001 MAIK "Nauka/Interperiodica".*

The phenomenon of laser radiation confinement due to self-defocusing under two-photon absorption conditions in semiconductors is described in much detail in [1–3], where it was shown that the energy threshold of confinement in the picosecond interval of the laser pulse durations can fall between 10 and 100 nJ. As the laser pulse duration increases, the confinement threshold tends to grow, since the rate of nonequilibrium carrier accumulation in the region of laser action decreases as a result of diffusion and recombination. Below, we will demonstrate that the effect of self-defocusing under the conditions of one-photon absorption on impurities in a semiconductor allows very low energy thresholds (below 10 pJ) to be obtained for the confinement of nanosecond laser pulses.

The experiments were performed on the samples of (i) compensated GaAs (thickness, d = 2.2 mm; bandgap width, E_g = 1.45 eV; resistivity, ρ = 20 MΩ cm; dopant concentration, $N \approx 10^{14}$ cm^{-3}) without antireflection coatings and (ii) compensated GaAs (thickness, d = 5 mm; resistivity, ρ = 1 MΩ cm; dopant concentration, $N \approx 10^{16}$ cm^{-3}) with antireflection coatings. A special feature of the compensated GaAs is the presence of deep impurity levels in the forbidden band, which serve as traps for the charge carriers. The ionization energies of such impurities are ΔE = 0.6–0.7 eV [4]. The source of radiation was a single-mode YAG:Nd laser (λ = 1.06 μm) with a laser pulse base width of 10 ns, a nearly Gaussian beam intensity profile with and a beam diameter at half height of 6 mm. The optical confinement scheme comprised two glass lenses, a semiconductor plate placed in the common focal plane of both lenses, and an output diaphragm (Fig. 1).

Figure 1 shows plots of the radiation energy at the confinement system output E_2 versus the input energy E_1 for a system with the following parameters: focal distances of both lenses, $F_1 = F_2$ = 10 cm; second lens to diaphragm distance, L = 40 cm; diaphragm window diameter, 6 mm; semiconductor, GaAs with ρ = 20 MΩ cm. As can be seen, the curves of E_2 versus E_1 exhibit three characteristic regions: low-threshold confinement at $E_3 \approx$ 40 nJ; intermediate confinement at $E_3 \approx$ 5 μJ; and confinement at $E_3 \approx$ 300 μJ.

A reason for the appearance of the low-threshold confinement is the emission of nonequilibrium charge carriers from deep impurity levels in the semiconductor. A growth of the carrier concentration in the region of laser action leads to the formation of a negative dynamic lens, which results in the radiation defocusing. This is a one-photon process, which accounts for the very low confinement threshold. For E_1 > 700 nJ, the E_2 versus E_1 plot is almost linear which is related to the saturation of absorption on the impurity levels. The intermediate confinement region with $E_3 \approx$ 5 μJ is related to the generation of nonequilibrium charge carriers upon two-photon interband absorption. The confinement effect due to this process was described in detail [1–3] for picosecond laser pulses. At E_1 > 15 μJ, the two-photon confinement efficiency decreases as a result of the compensating influence of the positive thermal lens. The third confinement region with $E_3 \approx$ 300 μJ is associated with three processes: (i) radiation self-focusing on the positive thermal lens, which is pos-

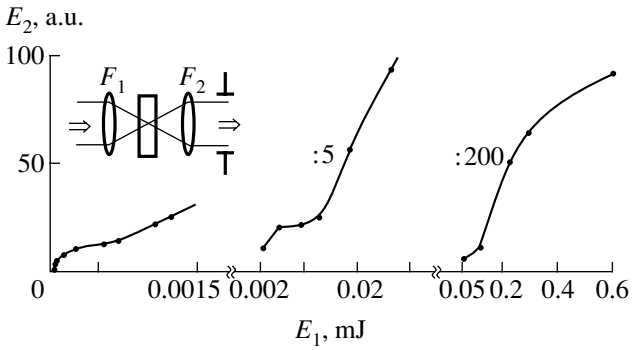

Fig. 1. The plots of energy output versus input illustrating the pulsed laser radiation confinement in doped GaAs for $F_1 = F_2$ = 10 cm, L = 40 cm, and ρ = 20 MΩ cm. The inset shows the optical scheme.

1063-7850/01/2712-1067$21.00

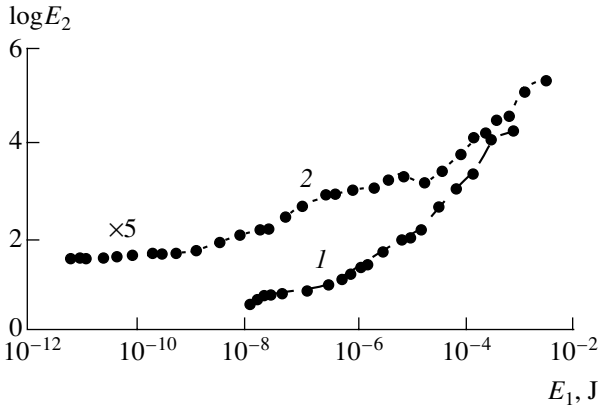

Fig. 2. The plots of energy output versus input for two schemes of laser radiation confinement in doped GaAs: F_1 = 6 mm; F_2 = 4 mm; L = 5 cm; ρ = 20 (*1*), 1 MΩ cm (*2*); d = 2.2 (*1*), 5 mm (*2*).

sible because $F_2 < L$; (ii) two-photon absorption; and (iii) absorption on the nonequilibrium charge carriers. Figure 2 presents the total E_2 versus E_1 plot (curve *1*) in the logarithmic scale.

The GaAs sample with ρ = 1 MΩ cm was studied in a system with F_1 = 6 mm, F_2 = 4 mm, and L = 5 cm. The E_2 versus E_1 plot for this sample is depicted in Fig. 2 (curve *2*). As can be seen, the low-threshold confinement region on this case extends from 5 pJ to ~1 nJ. In this region, the energy threshold could not be accurately determined because of insufficient sensitivity of the photodetector. The region of confinement related to the two-photon absorption ranges from $E_1 \sim 3$ nJ up to 50 nJ. As the input energy increases by a factor of 10^4 (5 pJ to 50 nJ), the output energy exhibits a 30-fold growth. For $E_1 > 100$ nJ, the E_2 versus E_1 plot reveals another four confinement regions in this optical scheme. One of the possible reasons for the appearance of these features is the complicated dynamics of a thick thermal lens. Formed at a high laser radiation intensity, the lens contains a region of self-defocusing related to one- and two-photon absorption and another region of self-defocusing related to the thermal effects. An additional contribution to the confinement can be due to the two-step processes of nonequilibrium carrier injection from valence to conduction band via free impurity levels. The presence of such free impurity levels is explained by the high intensity of radiation in the zone of laser action.

Thus, we have demonstrated that the effect of radiation defocusing under the conditions of absorption on impurity levels allows the energy threshold of the laser radiation confinement to be significantly reduced in comparison to that corresponding to the two-photon absorption. This effect can be used both for controlling the laser pulse amplitude and for protecting photodetectors from overloading.

Acknowledgments. This study was supported by the International Scientific-Technological Center, Grant no. 1454.

REFERENCES

1. T. E. Boggess, S. C. Moss, I. W. Boyd, *et al.*, Opt. Lett. **9** (7), 291 (1984).
2. J. A. Hermann, J. Opt. Soc. Am. B **1** (5), 729 (1984).
3. E. W. van Stryland, Y. Y. Wu, D. J. Hagan, *et al.*, J. Opt. Soc. Am. B **5** (9), 1980 (1988).
4. *Gallium Arsenide. Production and Properties*, Ed. by F. P. Kasamanly and D. N. Nasledov (Nauka, Moscow, 1973).

Translated by P. Pozdeev

Technical Physics Letters, Vol. 27, No. 12, 2001, pp. 981–983. Translated from Pis'ma v Zhurnal Tekhnicheskoĭ Fiziki, Vol. 27, No. 23, 2001, pp. 1–8.

Mechanical Instability of a Porous Material

S. P. Buyakova[a], V. I. Maslovskiĭ[b], D. S. Nikitin[b], and S. N. Kul'kov[b]

[a] *Institute of Strength Physics and Materials Science, Siberian Division, Russian Academy of Sciences, Tomsk, 634055 Russia*

[b] *Tomsk State University, Tomsk, 634050 Russia*

Received June 1, 2001

Abstract—The deformation behavior of a ceramic material based on $ZrO_2(Y_2O_3)$, yttrium partly stabilized tetragonal zirconia (YTZ), exhibits certain features related to a variety of the porous structure morphologies. In particular, the phenomenon of mechanical instability was observed in the YTZ rod and plate structures formed by ceramic synthesis. *© 2001 MAIK "Nauka/Interperiodica".*

The synthesis of porous materials possessing a preset combination of properties requires detailed knowledge of the relationship between these properties and structural features of each particular material. This is especially valid for the ceramic materials, where the presence of porosity may lead to a catastrophic loss of strength as a result of the limited possibility of relaxation of the stress concentrators upon loading. Indeed, the structure of ceramic materials makes the motion of dislocations virtually impossible.

Previously [1], we have studied the deformation behavior of a ceramic material based on $ZrO_2(Y_2O_3)$, yttrium partly stabilized tetragonal zirconia (YTZ), in a range of porosity from 10 to 65% and a mean pore size comparable with the average grain size. It was established that the YTZ based ceramic material features, besides elastic macrodeformation and microdamage accumulation in the form of microcracking, the phenomenon of a local material transfer into the pore space. However, an analysis of the deformation patterns did not reveal all the features in behavior of the porous ceramics. Moreover, the question as to how the mechanical behavior of the material is related to the pore space geometry remained unclear.

This study was devoted to the influence of various porosity morphologies on the mechanical behavior of YTZ ceramics under active compression loading conditions.

The experiments were performed on YTZ (ZrO_2 stabilized by 3 mol % Y_2O_3) ceramic samples with a porosity η ranging from 10 to 60% and a mean pore size either comparable with or markedly (by several orders of magnitude) exceeding the average grain size. The samples were prepared by methods of powder metallurgy, involving pressing followed by sintering of the ultradisperse ceramic powder in a temperature range from 1200 to 1600°C. This process ensured the obtaining of samples with a mean pore size comparable with the average grain size. The samples with greater pores were prepared by adding readily burning pore-forming particles (rosin, paraffin) to the initial powder.

The ceramic samples were mechanically tested on a Instron Model 1185 testing machine operating at a constant loading rate of 3×10^{-4} s^{-1}. The samples were characterized by the standard load–deformation (stress–strain) curves, from which the ultimate strength and relative deformation of the material were determined.

Irrespective of the relationship between the mean pore size and the average grain size in the ceramic, an increase in the relative pore volume in the material structure led to the development of multiple damage in the course of deformation: the higher the material porosity, the greater the damage level. This process was manifested in the deformation diagrams by sharp drops in the stress as a result of microcracking. The growth of microcracks stops on the pores, after which the material restores the ability to elastic deformation. As the porosity increases, the region of microcracking manifestations shifts toward greater deformations and becomes more extended. The deformation diagrams of the ceramic samples with a porosity above 20% exhibit a downward convexity, which is absolutely unusual for the sintered materials and can be considered (as in [1]) as evidence of a local material transfer in the course of deformation.

The deformation diagrams are traditionally described in terms of the power dependence of the type $Y = bX^k$. The exponent k depends on whether pressing or plastic shaping is the principal process in a given material. For the pure elastic deformation $k = 1$, the plastic deformation is characterized by $k < 1$, while the pressing process corresponds to $k > 1$. In order to determine the k value, the experimental data should be replotted in the logarithmic coordinates ($\ln\sigma$ versus $\ln\varepsilon$), after which the exponent is determined as the slope of the straight line.

1063-7850/01/2712-0981$21.00

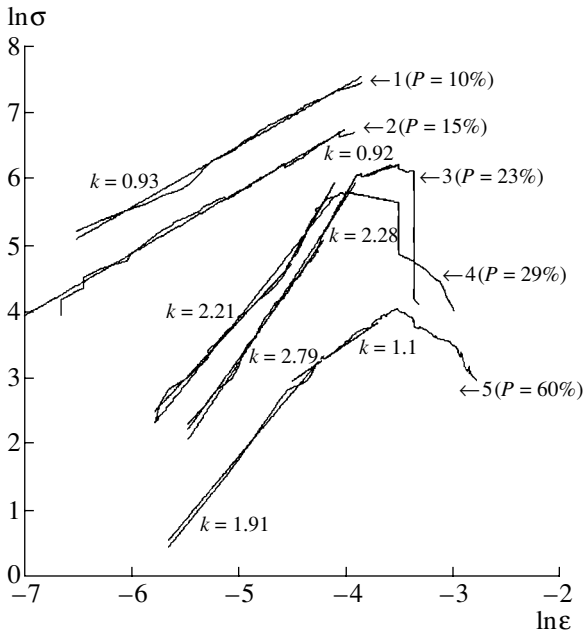

Fig. 1. Deformation (stress–strain) diagrams of the YTZ based ceramics plotted in the logarithmic coordinates (values in parentheses indicate the sample porosity; k is the exponent in the deformation equation).

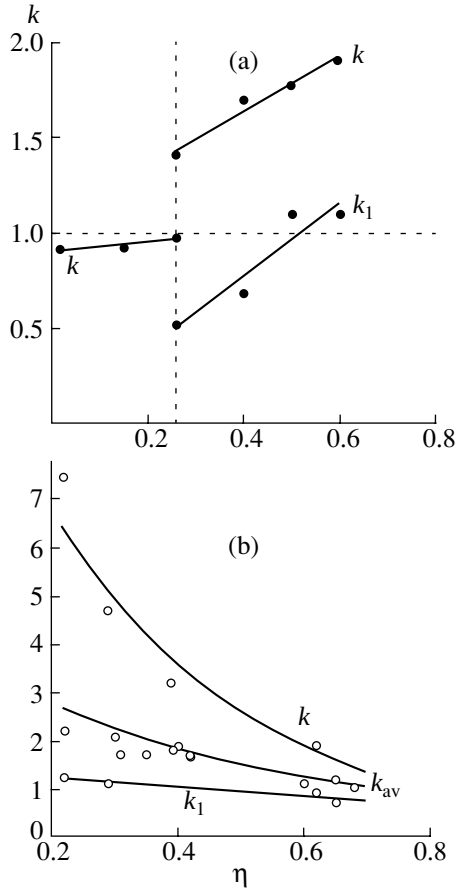

Fig. 2. Plots of the exponent k in the deformation equation versus the relative porosity for the YTZ based ceramics with (a) $d_1 \cong d_2$ and (b) $d_1 \ll d_2$ (d_1 is the mean pore size, d_2 is the average grain size).

The logarithmic deformation diagrams presented in Fig. 1 show that the behavior of ceramics with η above ~20% is described by several straight segments with different slopes and, hence, is characterized by several k values. Moreover, the higher the material porosity, the greater the number of such linear portions distinguishable in the diagram.

Figure 2a summarizes the exponents k in the deformation equation determined from the slopes of compression diagrams for all samples with a mean pore size comparable with the average grain size. As can be seen from these k versus η (porosity) plots, the experimental data fit well to the three straight lines and there exists a certain critical porosity value at which the character of deformation of a porous material sharply changes. Above this critical value, a second exponent appears which is significantly greater than that in the initial material. This behavior most probably reflects a change in the pore distribution, corresponding to a transition from isolated pores to a continuous pore system. As a result, the material essentially represents a combination of two subsystems deforming differently in response to the external load.

The materials with coarse pores are characterized by a sharply different behavior of k as a function of the porosity η: the smaller the porosity, the greater (on the average) the exponent. As can be seen from Fig. 2b, the k value exponentially decreases with increasing η. The top curve in Fig. 2b was obtained by approximating the values of exponents corresponding to the initial segments of deformation diagrams measured on the samples of various porosity. The bottom curve was obtained by approximating the data for all subsequent segments of the diagrams. The intermediate curve was constructed by approximating the average exponents determined for each diagram. Although the k values determined from the measured data exhibit a considerable scatter in the k–η coordinates, which reflects the random character of microfracture in the porous materials studied, the points on the whole fit quite satisfactorily to the approximating curves.

The metallographic examination of the surface of deformed samples unloaded before reaching the level of microdamage accumulation showed no evidence of the local material transfer related to the pressing deformation. Moreover, the deformation curves measured in this stage are reversible, which is indicative of the purely elastic character of the deformation. The superimposition of the photographs of the ceramic structure obtained before compression and upon unloading after the relative deformation of 1.5% (this corresponds to the region of downward convexity in the diagrams) exhibited perfect coincidence of the images.

Since no local material transfer into the pore space was observed in these samples, we may conclude that no pressing effect takes place and the deformation is purely elastic, reflecting the elastic interaction of elementary volumes in the porous structure. However, the

fact that the k values as high as 8 were obtained for the samples capable of compressing without any evidence of the residual deformation is absolutely unexpected.

The above results characterize the response to uniaxial loading of a sample representing a deformable system obtained as a result of the pressing–sintering technological process. This system comprises a great number of particles possessing random shapes and bound more or less strongly to the neighbors. The presence of some structural features in this system accounts for the observed character of the σ versus ε curve measured in experiment, which is significantly different from the diagrams typical of an isotropic elastic material. The presence of these structural features suggests that the observed behavior can be analyzed in terms of the possible mechanisms of deformation of the structural elements forming the ceramic samples employed in the tests. These mechanisms include, in particular, the one based on the known solution of the Hertz problem concerning the contact of two homogeneous bodies [2, 3]. Expanding this solution [2] to the case of contacting bodies of an arbitrary shape and introducing effective stresses, we obtain

$$\sigma \approx AE\varepsilon^{3/2}, \tag{1}$$

where A is a constant depending on the packing density and relative dimensions of contacting grains.

A system of grains possessing a linear or platelike shape or having weak contacts with the neighbors along lines or planes may exhibit a bifurcation transition into an adjacent equilibrium state, which would be accompanied by a reversible bending disappearing after removal of the initiating factor. Such structures, admitting a model representation in the form of a rod, can exist in high-porosity ceramics with a limited area of contact between grains. Owing to a small size of the grains and the insignificant size of the contact area formed upon sintering, the bending stresses arising as a result of the loss of stability do not exceed the ultimate strength of the ceramic material proper (which is virtually free of defects within the limits of the zirconium dioxide grain).

In order to estimate the deformation response of these structures after the loss of stability, let us consider the well-known problem of Euler's elastic [4]. Not repeating the initial assumptions made in [4], we will only recall that the angle of rotation of a pivot-supported rod after the loss of stability is determined from the relationship

$$\Phi = \int_0^{\pi/2} \frac{d\varphi}{\sqrt{1 - m^2\sin^2\varphi}} = \frac{kl}{2}; \quad \left(\sin\frac{\Theta_0}{2} = m, \quad k = \sqrt{\frac{P}{EJ}} \right), \tag{2}$$

where P is the force acting upon the rod, E is the shear modulus, and J is the moment of inertia of a transverse cross section with the length l.

Restricting the consideration to the case of small m (i.e., of the forces only slightly exceeding the critical values), expanding the integrand into series, and taking into account that the displacement of a mobile end of the rod is twice that of the middle [4], we arrive at an expression for the relative deformation of the rod in the supercritical region:

$$\Delta\varepsilon = 1 - \frac{2}{kl}(2\varepsilon - \Phi),$$
$$\varepsilon = \int_0^{\pi/2} \sqrt{1 - m^2}\sin\varphi d\varphi. \tag{3}$$

Accomplishing the necessary transformations, we obtain

$$\frac{\Delta\bar{P}}{P_c} = \frac{\Delta\varepsilon}{2}, \quad \text{where} \quad \Delta P = P - P_c, \quad P_c = \frac{\pi^2 EJ}{l^2} \tag{4}$$

or

$$\frac{\Delta P}{S} = \Delta\sigma = \frac{P_c}{2S}\Delta\varepsilon = \frac{\sigma_c}{2}\Delta\varepsilon, \tag{5}$$

where $\Delta\varepsilon$ is an additional deformation related to the supercritical bending and S is the area of the rod cross section. Relationships (5) can be also written as

$$\Delta\sigma = E\frac{\varepsilon_c}{2}\Delta\varepsilon, \tag{6}$$

showing that, after the loss of stability, deformations caused by the supercritical loading are linear functions of the stress increment but their order is $(2/\varepsilon_c)$ times greater as that according to the Hooke's law.

According to the above estimates, the rod structures formed upon sintering of the porous material can be expected to exhibit (even after the loss of stability) a considerable macrodeformation as structural elements in the elastic region, which agrees with the experimental observations.

REFERENCES

1. S. P. Buyakova, Han Wei, Li Dunmy, *et al.*, Pis'ma Zh. Tekh. Fiz. **25** (17), 44 (1999) [Tech. Phys. Lett. **25**, 695 (1999)].
2. L. D. Landau and E. M. Lifshitz, *Course of Theoretical Physics*, Vol. 7: *Theory of Elasticity* (Nauka, Moscow, 1987; Pergamon, New York, 1986).
3. Yu. A. Amen-Zade, *Theory of Elasticity* (Vysshaya Shkola, Moscow, 1971).
4. Yu. N. Rabotnov, *Mechanics of Deformable Solids* (Nauka, Moscow, 1979).

Translated by P. Pozdeev

Technical Physics Letters, Vol. 27, No. 12, 2001, pp. 984–986. Translated from Pis'ma v Zhurnal Tekhnicheskoĭ Fiziki, Vol. 27, No. 23, 2001, pp. 9–15.

Organic Impurity Preconcentration by a Multimembrane Inlet System of a Mass Spectrometer

V. T. Kogan and O. S. Victorova

Ioffe Physicotechnical Institute, Russian Academy of Sciences, St. Petersburg, 194021 Russia

e-mail: viktor.kogan@pop.ioffe.rssi.ru

Received June 21, 2001

Abstract—Using an inlet system comprising a series of membranes sequentially operating in a nonstationary flow regime, it is possible to increase the concentration of an organic impurity in a sample immediately before introduction into a mass spectrometer. The degree of preconcentration calculated in the approximation of a small response time of the membranes is proportional to $(k_j/k_m)^N$, where k_j and k_m are the membrane permeabilities for the impurity and matrix, respectively, and N is the number of membranes. For a butane admixture in air, the calculated relative effect for an inlet using two membranes instead of one is ~40, while the experimental verification using 0.1-mm-thick poly(dimethylsiloxane) membranes showed an increase in the degree of preconcentration by a factor of ~14. It is possible to approach the theoretical value by decreasing the time of impurity diffusion through the membrane at the expense of reduced membrane thickness. It is expected that multimembrane inlet systems will be especially effective in environmental monitoring, where a high sensitivity of the analysis is required with respect to toxic organic substances possessing k_j/k_m ratios much greater as compared to that of butane. © *2001 MAIK "Nauka/Interperiodica".*

Introduction. The permeability of a membrane material employed in the inlet system of a mass spectrometer may differ by several orders of magnitude for various chemical components of a mixed sample, which allows certain substances to be selectively admitted to the spectrometer [1, 2]. Using this property, it is possible, for example, to increase the sensitivity of analysis with respect to organic impurities in an organic matrix by using a membrane made of poly(dimethylsiloxane). Combining the simplicity of a membrane inlet design and the possibility of automated sample introduction into the vacuum system of a mass spectrometer allows requirements to the vacuum system of the spectrometer to be significantly reduced, which is especially important for portable instruments [3].

In comparing the properties of nonporous membranes, it is important to take into account, besides the aforementioned selective permeability in the quasistatic introduction regime, the time of response to a change in the concentration of the corresponding component in the sample mixture. This dynamic characteristic is described in terms of a time interval (τ) required for the flow intensity buildup (usually from 10 to 90% of the maximum stationary flow level) in the membrane following a jump in the partial pressure or concentration at the membrane entrance [4].

An allowance for the dynamic parameters is important for any spectrometer with a sample introduction systems involving membranes. For example, the membrane thickness in a single-membrane inlet is frequently selected so as to meet the requirement of low inertia (fast response) of the system, which allows the instrument to be used for a direct (real-time) monitoring of biochemical and technological processes [5–7] or continuous ecological control [5, 8, 9].

When the sample composition can be determined by discrete (more inertial) analyses, the efficiency can be increased, at the expense of increased system inertia, by using multistage inlets [10, 11]. However, even such systems require the dynamic properties of membranes to be taken into account for increasing the sensitivity of analysis.

System design and parameters. Figure 1 shows a schematic diagram of the inlet system designed for discrete mass-spectrometric analysis. The inlet comprises a gate valve and a sequence of membranes S_i ($i = 1, \ldots, N$) spaced by intermediate volumes V_i. This design allows processes of the sample diffusion in the membrane material and the intermediate volume filling to be separated in time. The multistage system parameters should be selected so as to obey the condition $t_{ss}/\tau \gg 1$, where t_{ss} is the time for establishing a steady-state mixture flow through the whole inlet system.

After a jumplike increase in the sample pressure at the inlet input, the system is capable of preconcentrating a jth component in the total gas flow, provided that the membrane permeability k_j for this component is higher than that k_m for the carrier gas (matrix). Additional requirements consist in ensuring homogeneity of the mixture composition in the initial sample and intermediate volumes. The former is provided by the sample flow conditions prior to entering the inlet and the latter,

1063-7850/01/2712-0984$21.00

by a low pressure maintained in the intermediate volumes. Special valves ensure the restoration of vacuum in the inlet after each measurement cycle.

Evidently, the conditions necessary for the effective preconcentration of a sample in the inlet are as follows: (i) $k_j \gg k_m$; (ii) mass-spectrometric analysis is performed within the time interval between supplying a sample to the inlet input and the time instant $t \ll t_{ss}$ (for a component with maximum permeability); (iii) $\tau \ll t$.

To analyze the proposed method of sample preconcentration, let us consider the simplest inlet system design with like membranes (made of the same material and possessing the same area S and thickness d) spaced by equal intermediate volumes V. Under the conditions formulated above, a change in the partial pressure $P_{j,n}$ of the jth component in the nth cell (including the two neighboring membranes and the intermediate volume between these membranes), from the moment of sample supply to the system input to a time instant t, can be described (we assume that $P_{j,n-1} \gg P_{j,n+1}$) by the equation

$$\partial P_{j,n}/\partial t \cong k_j S/V(P_{j,n-1} - 2P_{j,n}). \quad (1)$$

A solution to this equation can be presented in the following form:

$$P_{j,n} = k_j S/V\left(\int P_{j,n-1}\exp(2k_j St/V)dt + C\right) \times \exp(-2k_j St/V), \quad (2)$$

where C is an integration constant.

In the sample mixture supplied to the inlet input, occurring at the atmospheric pressure, the partial component pressure id P_{0j}; the pressure at the inlet output (the mass spectrometer input) is zero. For $t \ll V/(2k_jS)$ (i.e., long before attaining the steady-state regime), the time variation of the pressure in the nth cell is described by the relationship

$$P_{j,n} = k_j S/V\int P_{j,n-1}dt + C = P_{0,j}(k_j S/V)^n t^n/n! \quad (3)$$

Setting the ratio $k_j/k_m = M_j$ and taking into account that the flux I_j of the jth component at the inlet output is proportional to the partial pressure of this component at the input of the last membrane, we can solve the system of Eqs. (3) to determine the degree of enrichment (preconcentration) of the mixture with this component relative to the initial partial concentration ($P_{0,j}/P_{0,m}$):

$$(I_j/P_{0,j})/(I_m/P_{0,m}) \cong (M_j)^N. \quad (4)$$

Relationship (3) indicates that, at a time instant t after the sample mixture supply to the inlet input such that $\tau \ll t \ll t_{ss}$, the output flux of each component increases by the law t^n. The characteristic time scale of this growth depends on k_j (Fig. 2a), which allows a significant enrichment of the sample with components possessing large k_j to be provided (even for small difference between the corresponding permeabilities) by merely increasing the number of membranes N in the inlet system according to relationship (4).

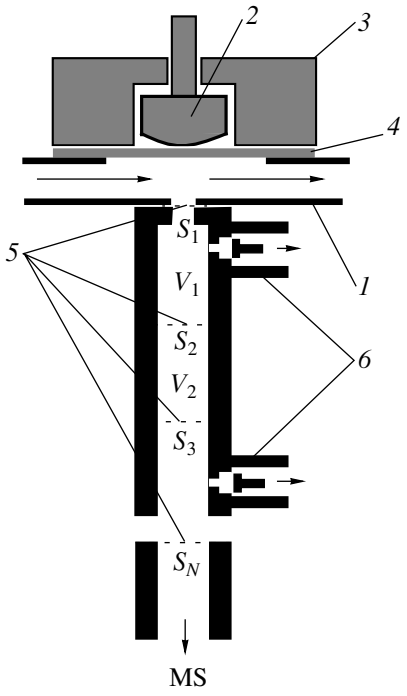

Fig. 1. Schematic diagram of a multimembrane inlet-preconcentrator: (*1*) flow of analyzed sample mixture; (*2*) gate valve; (*3*) case; (*4*) vacuum-tight sealing; (*5*) membranes; (*6*) valves; (MS) mass spectrometer.

It should be noted that the transition to a stationary flow regime leads to a decrease in the efficiency of sample preconcentration and analysis down to a level corresponding to a system employing a single membrane.

Experimental results and discussion. The measurements were performed with a portable mass spectrometer described elsewhere [12]. The inlet membranes were made of a sheet poly(dimethylsiloxane) with a thickness of $d = 100$ μm. The gas standards were prepared using a system of calibrated volumes. The test sample represented a mixture of *n*-butane (0.01%) with air. The selection of butane is explained, on the one hand, by a relatively high poly(dimethylsiloxane) permeability for this compound [3] and, on the other hand, by this component occurring in the gaseous state under normal conditions, which considerably simplifies the experiment.

The experiments were performed with an inlet system containing two membranes with $S = S_1 = S_2 = 0.78$ mm^2 and $V = 30$ mm^3. After a time period of $t = 3$ min (for the given inlet, $t_{ss} \cong 5$ min with butane) past the sample supply to the inlet input, the concentration of butane behind the second membrane increased 560 times (relative to nitrogen) as compared to the initial level. Using relationship (4) and taking into that the ratio of butane and nitrogen permeabilities for a single membrane is $M_b \cong 40$ [3], we might expect the mixture

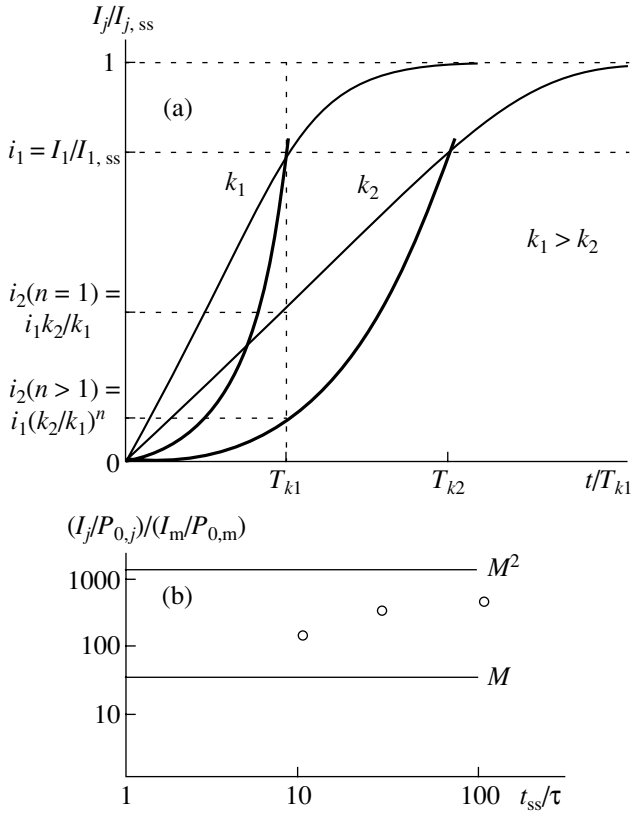

Fig. 2. (a) Buildup of the flows of components $j = 1$ and 2 at the inlet output for (thin solid curve) $n = 1$ ($N = 2$) and (thick solid curve) $n > 1$; (b) experimental plot of the preconcentration efficiency for butane in the air matrix versus the t_{ss}/τ ratio for a two-membrane (0.1-mm-thick poly(dimethylsiloxane) films) injector.

to be enriched with butane relative to nitrogen by a factor of $40^2 = 1600$. The difference between the calculated and experimental degrees of preconcentration is explained primarily by a significant difference in τ values for the carrier gas and impurity, with a non-strict obeying the conditions $\tau \ll t$ and $t \ll V(2k_jS)$.

Figure 2b shows a plot of the two-membrane inlet preconcentration efficiency for butane in the air matrix versus the t_{ss}/τ ratio. An attempt at reducing the time of analysis at a constant membrane thickness leads to a decrease in t_{ss} for butane and, hence, in the degree of preconcentration. In order to accelerate the analysis and retain the enrichment effect, it is necessary to use membranes of smaller thickness ($t \sim 1/d^2$).

Conclusion. An inlet system including several sequentially arranged membranes operating in a nonstationary sample flow regime can provide for a high sensitivity of the mass-spectrometric analysis of organic impurities in inorganic matrices. This technique may offer good prospects in the high-sensitivity analysis for aromatic and halogen-substituted hydrocarbons, heterocyclic, and some other organic compounds (with membrane permeabilities higher as compared to that of butane) encountered in solving a number of ecological and technological problems. Ensuring a significant reduction in the flow of a low-informative matrix component to the vacuum system of a mass spectrometer, such inlet systems are especially advantageous in portable instruments.

REFERENCES

1. A. J. Maden and M. J. Hayward, Anal. Chem. **68**, 1805 (1996).
2. M. A. LaPack, J. C. Tou, V. L. McGuffin, and C. G. Enke, J. Membr. Sci. **86**, 263 (1994).
3. V. T. Kogan, O. S. Viktorova, G. Yu. Gladkov, *et al.*, Prib. Tekh. Éksp., No. 1, 129 (2001).
4. R. A. Ketola, M. Ojala, H. Sorsa, *et al.*, Anal. Chim. Acta **349**, 359 (1997).
5. T. Kotiaho, F. R. Lauritsen, T. K. Choudhury, *et al.*, Anal. Chem. **63**, 875A (1991).
6. H. J. Degn, J. Microbiol. Methods **15**, 185 (1992).
7. F. R. Lauritsen and D. Lloyd, *Mass Spectrometry for the Characterization of Microorganisms*, Ed. by C. Fenselau (American Chemical Society, Washington, DC, 1994), ACS Symp. Ser. 541, pp. 91–106.
8. R. G. Cooks and T. Kotiaho, *Pollution Prevention in Industrial Processes*, Ed. by J. J. Breen and M. J. Dellarco (American Chemical Society, Washington, DC, 1994), ACS Symp. Ser. 508, pp. 126–154.
9. S. J. Bauer and R. G. Cooks, Am. Lab. (Shelton, Conn.) **25**, 36 (1993).
10. L. E. Dejarme, S. J. Bauer, R. G. Cooks, *et al.*, Rapid Commun. Mass Spectrom. **7**, 935 (1993).
11. M. E. Cisper, C. G. Gill, L. F. Townsend, and P. H. Hemberger, Anal. Chem. **67**, 1413 (1995).
12. V. T. Kogan, A. K. Pavlov, Yu. V. Chichagov, *et al.*, Field Anal. Chem. Technol. **1** (6), 331 (1997).

Translated by P. Pozdeev

Technical Physics Letters, Vol. 27, No. 12, 2001, pp. 987–990. Translated from Pis'ma v Zhurnal Tekhnicheskoĭ Fiziki, Vol. 27, No. 23, 2001, pp. 16–24.

Phase Coherence Diagnostics by One-Dimensional Time Series

N. B. Yanson[a], A. G. Balanov[a], V. S. Anishchenko[a,*], and P. W. E. MacClintock[b]

[a] *Saratov State University, Saratov, Russia*

** e-mail: wadim@chaos.ssu.runnet.ru*

[b] *Physics Department, Lancaster University, Lancaster, LA1 4YB, Great Britain*

Received May 10, 2001

Abstract—A new method, employing one-dimensional time series, is proposed for diagnostics of the presence or absence of phase synchronization between several interacting self-sustained oscillators. The procedure is based on introducing a polar coordinate system into the residence time mapping and studying the angle dynamics in this system. The method is verified by application to realizations reflecting the dynamics of two and three interacting processes in the presence of noise. © *2001 MAIK "Nauka/Interperiodica".*

Synchronization effects are frequently encountered in both nature and technology [1]. At present, it is clear that this fundamental phenomenon is of principal significance in many biological processes [2].

In the simplest case of two interacting self-sustained oscillators featuring periodic oscillations in the absence of noise, the synchronization (phase-locking) implies a phenomenon whereby the base oscillation frequencies (initially incommensurate) interact so as to become rationally interrelated; that is, they obey the ratio n/m, where m and n are integers [3, 4]. Then, the instantaneous phases $\varphi_{1,2}$ always satisfy the "phase-lock" condition $m\varphi_1 - n\varphi_2 = \text{const}$. Evidently, the presence or absence of synchronization in this ideal case can be readily checked by direct analysis of the spectrum of oscillations in one of the interacting systems.

The situation is significantly complicated in the presence of noise, because the noise fluctuations systematically violate the phase-lock condition and make only the so-called "effective" synchronization possible [5]. Under the violated phase-lock conditions (phase-break), the oscillation frequencies may fail to be rationally interrelated [6], which makes the phase coherence diagnostics by the spectrum ineffective. However, it is still possible to judge on the phase coherence by estimating the phase relationships between oscillations in the interacting systems.

The investigation of phase relationships for the phase coherence diagnostics offers a good approach for both periodic and chaotic oscillations [7], and even to stochastic systems [8, 9]. However, it is sometimes rather difficult to separate signals from various interacting subsystems. This is especially so when dealing with living systems, where it is frequently impossible to take the signals directly from the interacting subsystems of interest.

Below, we propose a method for diagnostics of the phase synchronization (or, otherwise, the absence of synchronization) in a system of coupled oscillators, using only one signal from this system. The method is based on an analysis of the mapping of times T_i of the signal residence to a certain threshold level.

Let us study first the simplest case of two interacting systems. Consider a quasi-harmonic (i.e., close to harmonic) self-sustained oscillator oscillating with an amplitude R and an intrinsic frequency ω_0 under the action of a weak harmonic signal with an amplitude r and a frequency Ω. Assuming that $r \ll R$, we can describe the resulting oscillations with a high precision as

$$x(t) = R\sin(\omega t) + r\sin(\Omega t). \qquad (1)$$

Here, the frequency ω will coincide with ω_0 in the absence of synchronization and can be shifted away from ω_0 if the phase locking takes place.

We determine the residence time T_i as a time interval between two sequential points at which the $x(t)$ signal changing in one direction intersects with the threshold level $x = 0$. In order to determine this, we have to find all the time instants t_i at which the signal intersects the zero level. Evidently, the transcendental equation $x(t) = 0$ may possess no analytical solution in the general case. However, taking into account that the amplitude of the first term significantly exceeds that of the second term, we may suggest that the true intersection points t_i will be close to the time instants $t_k^* = \pi k/\omega$ where $\sin(\omega t)$ takes zero values. Then, we can expand the right-hand part of Eq. (1) into Taylor's series with respect to t_k^* and neglect the nonlinear terms.

In order to find the time instants corresponding to the signal intersecting the level $x = 0$ only in one direction, we have to determine each next zero of the expansion

$$t_i \approx -\frac{r}{R\omega}\sin\frac{2\pi i\Omega}{\omega} + \frac{2\pi i}{\omega}. \qquad (2)$$

1063-7850/01/2712-0987$21.00

Using this expression, we readily determine the residence time T_i:

$$T_i = t_{i+1} - t_i = 2\frac{r}{R\omega}\cos(\Psi_i + \pi\xi)\sin\pi\xi + \frac{2\pi}{\omega}, \quad (3)$$

where $\xi = \Omega/\omega$ and $\Psi_i = 2\pi i\Omega/\omega$. Note that ξ has the sense of a rotation number, reflecting the number of system oscillations per one external oscillator action, and Ψ_i is the instantaneous phase of the external signal at the time instant $2\pi i/\omega$ (i.e, in a certain stroboscopic cross section).

Let us introduce a polar coordinate system in the rest time mapping $T_{i+1}(T_i)$, for which purpose the center is placed at the point $(2\pi/\omega, 2\pi/\omega)$. Then, the polar angles ϕ_i are related to the residence times by the formula

$$\phi_i = \arctan\left(\frac{T_{i+1} - \frac{2\pi}{\omega}}{T_i - \frac{2\pi}{\omega}}\right). \quad (4)$$

Let us consider the dynamics of ϕ_i angles. Using formula (3), we obtain a relationship

$$\tan\phi_i = \cos 2\pi\xi - \tan(\Psi_i + \pi\xi)\sin 2\pi\xi, \quad (5)$$

which indicates that the angle of rotation in the introduced polar coordinate system is directly related to the phase of the external action at the fixed time instants $2\pi i/\omega$, where the phase of intrinsic oscillations changes by 2π. This is essentially a definition of the so-called relative phase, which is frequently employed in the phase coherence diagnostics using two measured signals [10].

By the same token, we derive an expression for $\cot\phi_{i-1}$. Upon adding this to formula (5), we obtain a mapping for the instantaneous polar angles of the residence time mapping:

$$\phi_i = \arctan(2\cos 2\pi\xi - \cot\phi_{i-1}). \quad (6)$$

This mapping belongs to the homotropy class on circumference of the topological degree 1, which are traditionally used in the descriptions of dynamics of the phase difference between interacting oscillators. The main characteristic of such mappings is the rotation number ν characterizing the ratio of the principal time scales of the interacting oscillators. For the above mapping, this quantity is calculated as

$$\nu_\phi = \frac{1}{2\pi}\lim_{i\to\infty}\frac{\phi_0 - \phi_i}{i} = \xi.$$

Thus, the rotation number for mapping (6) exactly equals the ratio of frequencies of the interacting oscillators or the rotation number of the system studied.

Now let us consider the case of a quasi-harmonic system under the action of n harmonic signals characterized by the frequencies Ω_i and amplitudes A_i ($i = 1, 2, \ldots, n$). We will assume as before that the external signal amplitudes are much smaller as compared to the amplitude of oscillations in the self-sustained oscillator studied: $A_i \ll R$ ($i = 1, 2, \ldots, n$). In this case, the oscillations $x(t)$ can be presented in the following form:

$$x(t) = R\sin\omega t + \sum_{j=1}^{n} A_j \sin\Omega_j t, \quad A_j \ll R. \quad (7)$$

We denote $\Omega_j/\omega = \xi_j$ and $\beta_j = (A_j/A_1)(\sin\pi\xi_j/\sin\pi\xi_1)$ and put $\beta_1 = 1$. Then, repeating transformations used to derive expression (6), we obtain a mapping for the residence time angles in the case of an arbitrary number of interacting processes:

$$\phi_i = \arctan\left(2\cos 2\pi\xi_1 - \cot\phi_{i-1} + 2\frac{\sum_{j=2}^{n}\beta_j\cos(2\pi i\xi_j + \pi\xi_j)(\cos 2\pi\xi_j - \cos 2\pi\xi_1)}{\sum_{j=1}^{n}\beta_j\cos(2\pi i\xi_j + \pi\xi_j)}\right). \quad (8)$$

This expression describes the dynamics of the mapping angles of residence times for the quasi-periodic oscillations characterized by n independent frequencies. These oscillations correspond to an N-dimensional attractor in the phase space of the initial system.

In this study, we will consider the cases of $n = 1$ and 2 for the van der Pol generator under a periodic or quasi-periodic action in the presence of noise.

In order to verify the proposed method in the case of nonstationary oscillations, let us consider the dynamics of a nonautonomous van der Pol generator with the intrinsic frequency subject to slow fluctuations

$$\dot{x} = y; \quad \dot{y} = \epsilon(1 - x^2)y - \omega^2 x + C\sin\Omega t;$$
$$\omega = \omega_0 + \frac{D_\eta}{\tau}\eta(t); \quad \dot{\eta} = -\frac{\eta}{\tau} + \mu(t), \quad (9)$$

where $\epsilon = 0.1$, $\omega_0 = 1$, $C = 1$, $\Omega = 0.333$, $\mu(t)$ is a Gaussian white noise ($\langle\mu(t)\rangle = 0$, $\langle\mu(t)^2\rangle = 1$), and $\eta(t)$ is a "colored" noise with the intensity D_η and the correlation time $\tau = 200$.

In the absence of slow fluctuations, $D_\eta = 0$ and the nonautonomous system exhibits a 1 : 3 synchronism, with three intrinsic oscillations of the generator per one oscillation of the external signal. The systems obey the phase-lock condition $\Phi_0(t) - 3\Phi_f(t) = \text{const}$, where $\Phi_0(t)$ is the instantaneous phase of the generator and $\Phi_f(t)$ is the phase of the external action.

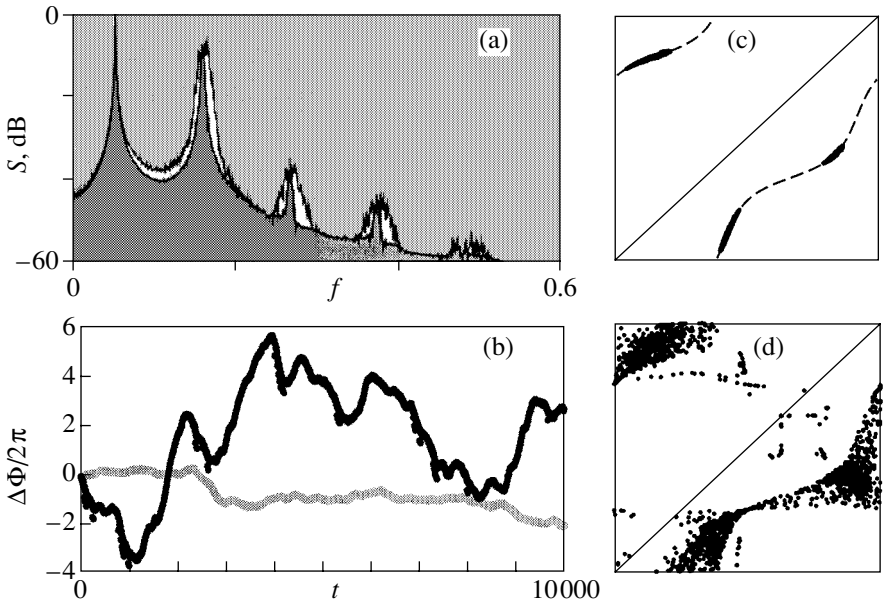

Fig. 1. Schematic diagrams illustrating the dynamics of interaction in system (9) for two values of the noise intensity: (a) oscillation power spectra calculated using time series of system (9); (b) phase difference between the external action and the system (9) response; (c, d) maps of the residence time angles.

As the intensity D_η increases, the synchronization regime changes to the so-called "effective synchronization," whereby the phase-lock condition is satisfied for finite but rather long time periods (usually greater than 10^2–10^3 characteristic oscillation periods). A further increase in the intensity of fluctuations breaks the synchronization.

Figure 1a presents the spectra of oscillations corresponding to the aforementioned regimes: the shadowed and open spectra refer to $D_\eta = 0.1$ and $D_\eta = 0.7$, respectively. As can be seen, the two spectra are qualitatively much alike; moreover, the ratios of the peak frequencies corresponding to the intrinsic and external oscillations are also very close (2.96 with an effective synchronization versus 3.05 in the absence of such synchronization). Thus, the spectrum cannot be used for reliably establishing the phase coherency of oscillations in this system.

However, a reliable information on the presence or absence of phase synchronization can be gained from an analysis of the time variation of the phase difference between intrinsic and external oscillations. Figure 1b shows the pattern of time variation of the phase difference for the oscillation $\Phi_0(t) - 3\Phi_f(t)$ for $D_\eta = 0.1$ (grey) and $D_\eta = 0.7$ (black). As can be seen, the length of a phase-lock "plateau" in the former case exceeds 10^3 characteristic periods of intrinsic oscillations of the van der Pol generator. From this, we infer that an effective phase locking regime takes place. In the second case, the curve exhibits virtually no regions indicative of the phase locking.

Let us apply the method described above. For this purpose, we fix the cross section $x = 0$ and determine the residence times for the phase trajectory returning to this plane for each value of the fluctuation intensity. Upon introducing the polar coordinate system into the residence time mapping and obtaining a sequence of the residence time angles, we plot the corresponding map. Figures 1c and 1d show the maps of the residence time angles for $D_\eta = 0.1$ and 0.7, respectively. In the former case, the plot clearly shows three groups of points belonging to the same one-dimensional curves, which is evidence of the 1 : 3 synchronism. On the contrary, the map of Fig. 1d is chaotic and reveals no clear structure, which can be classified as the absence of phase locking. This example shows that the proposed method can be effective even in the case of nonstationary oscillations.

Now, we will illustrate application of the proposed method to the study of phase dynamics win the case of three independent processes. Consider a self-sustained oscillator under the action of two harmonic external signals in the presence of noise:

$$\begin{aligned} \dot{x} &= y; \\ \dot{y} &= \epsilon(1-x^2)y - \omega_0^2 x + C_1 \sin\Omega_1 t \\ &\quad + C_2 \sin\Omega_2 t + \sqrt{D}\mu(t). \end{aligned} \tag{10}$$

These expressions describe a non-autonomous van der Pol generator operating under the action of a quasiperiodic signals with the characteristic frequencies $\Omega_1 = 0.5$ and $\Omega_2 = 0.1$ and equal amplitudes $C_1 = 0.1$ and $C_2 = 0.1$; the parameter $D = 0.0001$ determines intensity of the additive white noise. The parameters

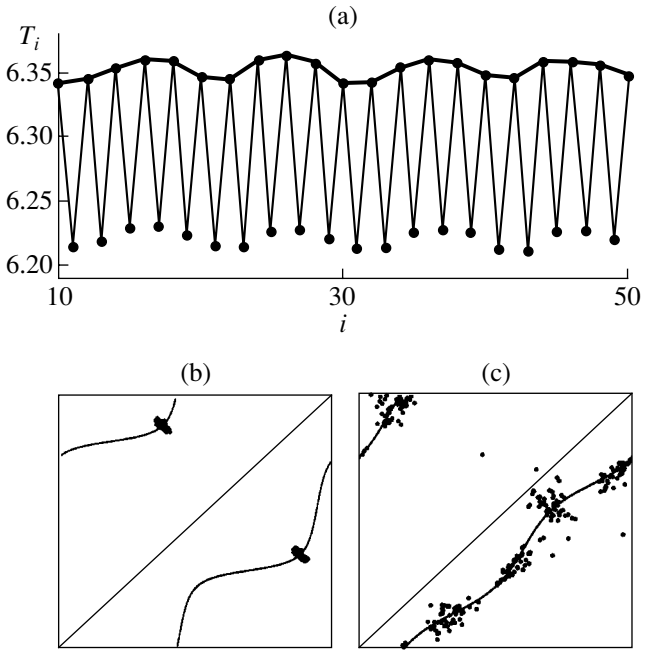

Fig. 2. Schematic diagrams illustrating the dynamics of interaction in system (10): (a) plot of the residence times; (b) map of the residence time angles; (c) map of the angles of the residence time maxima.

were selected so as to provide for a 1 : 2 synchronism between one external action and the self-sustained oscillator and a 1 : 5 synchronism between the two external factors.

Figure 2a shows a fragment of the sequence of residence times for the phase trajectory of system (10) returning to the plane $x = 0$. The corresponding map of the residence time angles is presented in Fig. 2b. As can be seen, all points in Fig. 2b are concentrated in two "clouds," which is evidence of the 1 : 2 synchronism between the generator and the high-frequency external action. This is also confirmed by the fact that the two clouds are lying exactly on the curve representing a successor function of the mapping (6) for $\xi = 1/2$. Thus, despite the fact that the system studied features the interaction of three oscillation processes, the proposed method successfully revealed the phase synchronization between two processes with maximum characteristic frequencies.

However, the map in Fig. 2b does not allow us to judge on the possible synchronization between the two high-frequency processes and the third one, characterized by the minimum frequency. In order to check for the presence or absence of phase locking between the latter process and the first (high-frequency) external action, we performed the following procedure. Using the sequence of residence times (Fig. 2a), we determined the local maxima (connected by an envelope curve) and introduced the corresponding polar angles as was previously done for the residence times. This procedure essentially excludes from the consideration one process, namely, that characterized by the maximum frequency; in this case, the intrinsic oscillations of the van der Pol generator. Figure 2c shows the map of the angles determined by this procedure. Apparently, the points of this map also fit to a one dimensional curve that can be described with a good accuracy by the analytical formula (6). The number of point clouds is indicative of the 1 : 5 synchronism between the two external actions. Thus, the proposed method allowed us to estimate the phase locking in each pair of the interacting processes. As for the study of phase locking in the case of a still greater number of interacting processes, we believe that a useful approach is offered by the procedure of determining local maxima. However, no detailed analysis of this question was performed within the framework of the present study.

Thus, we have proposed a method for estimating the phase synchronization of several interacting processes using only a one-dimensional time series. A theory for the method was developed for the case of a weak interaction and it was demonstrated that the method works well in the case of nonstationary and noisy data obtained by numerical modeling. We believe that this method can useful in a number of practical applications, especially in the case when it is impossible to extract signals simultaneously from all interacting self-sustained oscillators.

Acknowledgments. This study was supported by the US Civilian Research and Development Foundation (CRDF grant no. REC 006) and by grants from the Engineering and Physical Sciences Research Council (UK) and the Medical Research Council (UK).

REFERENCES

1. I. I. Blekhman, *Synchronization in Nature and Engineering* (Nauka, Moscow, 1981).
2. L. Glass and M. C. Mackey, *From Clocks to Chaos: the Rhythms of Life* (Princeton Univ. Press, Princeton, 1988; Mir, Moscow, 1991).
3. B. van der Pol, Radio Rev. **1**, 701 (1920).
4. A. A. Andronov and A. A. Vitt, in *Collection of the Works of A. A. Andronov* (Akad. Nauk SSSR, Moscow, 1956).
5. A. N. Malakhov, *Fluctuations in Self-Sustained Oscillator Systems* (Nauka, Moscow, 1968).
6. R. L. Stratonovich, *Selected Problems of the Fluctuation Theory in Radio Engineering* (Sov. Radio, Moscow, 1961).
7. M. G. Rosenblum, A. S. Pikovsky, and J. Kurths, Phys. Rev. Lett. **76**, 1804 (1996).
8. A. Neiman, A. Silchenko, V. S. Anishchenko, and L. Schimansky-Geier, Phys. Rev. E **58**, 7118 (1998).
9. V. S. Anishchenko, T. E. Vadivasova, and V. V. Astakhov, *Nonlinear Dynamics of Chaotic and Stochastic Systems* (Saratovsk. Univ., Saratov, 1999).
10. C. Schäfer, M. G. Rosenblum, J. Kurths, and H.-H. Abel, Nature **392**, 239 (1998).

Translated by P. Pozdeev

Technical Physics Letters, Vol. 27, No. 12, 2001, pp. 991–993. Translated from Pis'ma v Zhurnal Tekhnicheskoĭ Fiziki, Vol. 27, No. 23, 2001, pp. 25–30.

Spatially Periodic Electron Beams Formed by a Magnetron Gun System with Secondary-Emission Cathodes

N. I. Aizatskii, A. N. Dovbnya, V. V. Zakutin, N. G. Reshetnyak, V. P. Romas'ko, Yu. Ya. Volkolupov, and M. A. Krasnogolovets

"Uskoritel" Research Complex, Kharkov Physicotechnical Institute, National Scientific Center, Kharkov, Ukraine

Received May 21, 2001

Abstract—The process of electron beam generation was studied in a magnetron gun system with secondary-emission cathodes and periodically arranged metal rod anodes. © *2001 MAIK "Nauka/Interperiodica".*

Introduction. Magnetron injector guns with cold metal secondary-emission cathodes are of interest as electron sources for electron accelerators and high-power microwave devices. These electron sources are characterized by high current densities (50–70 A/cm^2) and long lifetimes (estimated at ~10^5 h). The guns have a relatively simple design, comprising a cylindrical cathode and a tubular anode exposed to a magnetic field.

The results of investigations [1–4] showed that an electron beam generated by such a gun has a tubular shape with an internal diameter equal to that of the cathode and an outer diameter determined by the magnetic field and the anode configuration. The anode geometry affects the electric field distribution at the cathode, determines conditions of the secondary emission and the electron beam generation, and influences the beam profile and outer diameter. In a coaxial system with cylindrical anode, the electron beam has a tubular profile, while a small asymmetry renders the beam cross section crescent-shaped with a break in the region of a maximum distance between cathode and anode.

In magnetron gun systems [5], the use of cylindrical anodes does not allow the distance between beams to be reduced below the anode diameter so as to obtain a structure of closely spaced beams at the gun system output. This disadvantage can be removed by placing anodes at the points of intersection of a system of mutually perpendicular lines (the sites of a square lattice) and cathodes—at the points of intersection of the diagonals connecting the anode sites. In this case, the electric field is inhomogeneously distributed in the anode–cathode gaps. The process of secondary electron multiplication and beam formation in such systems were not studied. Below, we report on the results of investigation of the electron beam generation in a magnetron gun system with cold metal secondary-emission cathodes and periodically arranged metal rod anodes.

System description. Figure 1 shows a schematic diagram of the anode and cathode arrangement. As can be seen, the anodes are placed in a horizontal plane at the points of intersection of a system of mutually perpendicular axes x and y (forming a square lattice) and the cathodes are arranged at the points of intersection of the diagonals connecting the anode sites. As a result, we obtain a periodic system of electron guns, the number of which can be increased either in one direction (so as to obtain a beam with an almost linear cross section) or in both directions (to form any desired configuration in the xy plane). Thus, the complex gun essentially comprises a system of cells which can be arranged so as to generate a beam with a preset configuration. In studying the process of beam formation in the gun with such

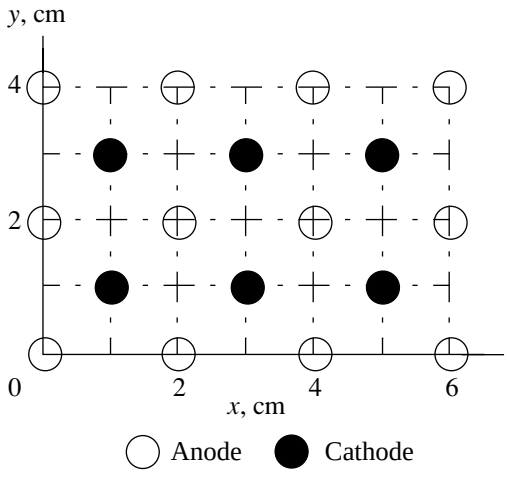

Fig. 1. Schematic diagram of a spatially periodic magnetron gun system with metal rod anodes and secondary-emission cathodes.

1063-7850/01/2712-0991$21.00 © 2001 MAIK "Nauka/Interperiodica"

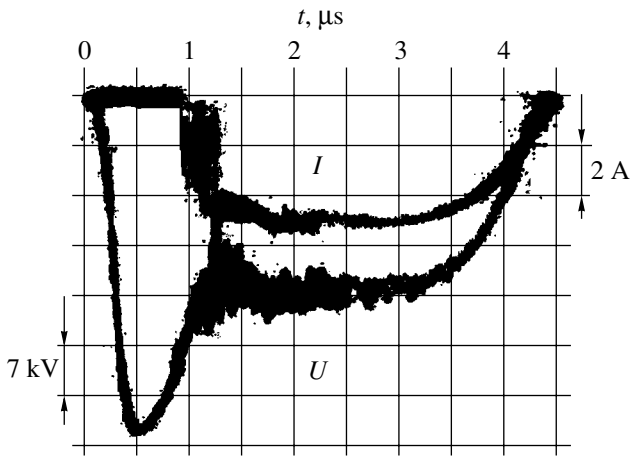

Fig. 2. Typical oscillograms of the pulsed cathode voltage *U* and the corresponding electron beam current pulse *I*.

a geometry, where the electric field distribution significantly differs from that in a coaxial system, we will assume that the electric field is at the cathode surface is sufficiently homogeneous to provide for the secondary electron multiplication and beam generation.

In the first step, the experiments were performed with a gun representing a single cell. The cell contained an anode section comprising four 5-mm metal rods forming a square with a 20-mm distance between centers. The cathode was placed at the center of the square, so that the anode–cathode spacing was ~9.5 mm. We have studied the guns with a cathode diameter of 2, 5, or 16 mm and a length of 120 mm.

In the second step, we studied a gun system comprising four cells of the type descried above, with both cathodes and anodes having a diameter of 5 mm.

The experiments with these guns were conducted in a setup described previously [2]. The magnetron gun was powered from a modulator unit forming voltage pulses with an amplitude of up to 100 kV, a pulse duration of ~5 μs, and a repetition rate of 50 Hz. The rod anodes were grounded, and the voltage pulses of negative polarity were applied to the cathode. The secondary electron emission process was initiated at the trailing edge (0.6 μs long) of an overshoot specially formed on the cathode voltage pulse.

The magnetron gun was placed into a vacuum chamber evacuated to a residual pressure of ~10^{-6} Torr. A magnetic field necessary for the beam generation and transport was generated by a solenoid. In the course of the investigation, we measured the cathode voltage, the electron beam current (with the aid of a Faraday cup), and the beam spot size (by "prints" obtained on an aluminum or molybdenum foil).

Experimental results. In the first step, we studied the electron beam generation conditions and measured the beam parameters in a single cell with the cathode diameters 2, 5, and 16 mm. The experiments confirmed the secondary electron multiplication and beam generation. First, the beam current measured with a Faraday cup was studied as a function of the magnetic field strength at a constant voltage pulse amplitude U_c of 40 kV applied to a cathode with a diameter of 5 mm. It was found that the beam current increases with the magnetic field strength *H*, reaching 12 A for $H \sim$ 2500 Oe. The beam current buildup time was 5–15 ns, depending on the magnetic field strength. At a voltage pulse amplitude of 28 kV and $H \sim 1600$ Oe, the beam current was 5.3 A. Analogous dependences were also obtained for other cathode voltages. Figure 2 shows typical oscillograms of the pulsed cathode voltage *U* and the corresponding electron beam current pulse *I*.

The total beam current print obtained on a metal foil at a large magnetic field strength showed a ring trace with an outer diameter of ~7 mm and an inner diameter of ~5 mm in the central part. The beam generated at a small magnetic field strength, under which conditions the secondary electrons could escape into the space between rods (in the direction perpendicular to the beam) formed a halo trace with a diameter of ~15 mm.

In the case of a 2-mm cathode, the system also operated in the regime of secondary electron emission and beam generation. At a cathode voltage pulse amplitude of ~26 kV and a magnetic field strength of 3000 Oe, the total beam current measured by the Faraday cup was 2.6 A. At a distance of 80 mm from the gun output, the beam print had the shape of a ring with the outer and inner diameters of ~6 and ~3 mm, respectively.

The experiments with a 16-mm cathode showed a small beam current in the Faraday cup (0.1–0.2 A for $U_c = 40$ kV and $H = 1300$ Oe). As the magnetic field strength increases, the secondary electron emission process breaks, after which no current is measured in the Faraday cup. This is explained by the fact that the conditions necessary for the secondary electron multiplication and beam generation are not obeyed in a system of closely spaced (~4 mm) electrodes featuring strongly inhomogeneous electric field distribution.

The results of experiments with a gun containing four electrode cells showed evidence of the secondary electron multiplication and beam generation in each cell of this system. The total beam current measured with a Faraday cup was approximately four times the value for a single cell. For example, the beam current measured at $U_c \sim 28$ kV and $H \sim 2200$ Oe was ~ 22 A.

In some regimes, we observed high-frequency (300 MHz and above) oscillations on top of the beam current pulse, which resulted in an ~15–25% modulation of the current pulse intensity. We attribute these oscillations to interaction of the electron beam with a

periodic resonance structure formed by the metal rod anodes.

Conclusion. A magnetron gun system with rod anodes, featuring an inhomogeneous electron field, can provide for an effective secondary electron multiplication and a spatially periodic beam generation. In a system comprising four electrode cells, a total beam current of ~22 A was reached, which is about four times the value observed for a single cell. The total output beam current pulse power was ~600 kW. Such beams can be used in multibeam microwave devices. A further increase in the number of gun cells, which is only limited by the volume occupied by the magnetic field, allows spatially developed high-intensity electron beams to be obtained for various applications.

REFERENCES

1. J. F. Skowron, Proc. IEEE **61** (3), 69 (1973).
2. Yu. A. Volkolupov, A. N. Dovbnya, V. V. Zakutin, *et al.*, Zh. Tekh. Fiz. **71** (2), 98 (2001) [Tech. Phys. **46**, 227 (2001)].
3. Y. M. Saveljev, W. Sibbett, and D. M. Purkes, Phys. Plasmas **4** (7), 2319 (1997).
4. A. V. Agafonov, V. P. Tarakanov, and V. M. Fedorov, Vopr. At. Nauki Tekh., Ser. Yad. Fiz. Issled. **1** (2–3), 134 (1997).
5. V. V. Zakutin, A. N. Dovbnya, N. G. Reshetnyak, *et al.*, Zh. Tekh. Fiz. **71** (3), 78 (2001) [Tech. Phys. **46**, 348 (2001)].

Translated by P. Pozdeev

Technical Physics Letters, Vol. 27, No. 12, 2001, pp. 994–998. Translated from Pis'ma v Zhurnal Tekhnicheskoĭ Fiziki, Vol. 27, No. 23, 2001, pp. 31–40.

Anomalies in the Ultrasound Reflection from a Solid–Dissipative Medium Interface

D. A. Kostyuk and Yu. A. Kuzavko*

Brest State University, Brest, Belarus

** e-mail: kuzavko@newmail.ru*

Received April 23, 2001

Abstract—The reflection of longitudinal acoustic waves from the interface between a solid and a strongly dissipative medium was theoretically studied. It is shown that the reflection coefficient and the reflected signal phase significantly depend on the coefficient of ultrasound absorption in the dissipative medium. An algorithm for restoring the time variation of the dissipative medium viscosity during solidification is proposed, which is based on the results of measurements of the amplitude reflection coefficient for a pulsed ultrasonic signal. The reflection and transmission coefficients are determined for the ultrasound wave amplitude, velocity, pressure, and intensity. An expression is derived for the acoustic energy absorbed upon reflection from a dissipative medium. A frequency dependence of the amplitude and generalized phase of the signals reflected from and transmitted through the interface are restored from the results of spectral calculations. The theoretical results are confirmed by experimental data on the reflection of acoustic pulses from an organic glass–epoxy compound resin interface measured during solidification of the latter medium. According to these data, the reflection coefficient and the reflected acoustic pulse duration decreased upon solidification of the epoxy compound. © *2001 MAIK "Nauka/Interperiodica".*

Introduction. The reflection of continuous and pulsed acoustic signals from the boundaries between various media has been theoretically and experimentally studied in sufficient detail [1, 2]. However, to our knowledge, the reflection of an acoustic wave from the boundary of a medium characterized by a strong absorption of sound oscillations has not been investigated, although this case can be of interest both from the theoretical standpoint and in practical applications. Below, we will consider the reflection of a longitudinal acoustic wave from a flat interface between a solid and a strongly dissipative medium, for example, a viscous liquid.

Theory. Consider a harmonic longitudinal acoustic wave propagating without attenuation in a solid and incident onto an interface between this solid and a strongly dissipative medium (SDM). The wave is partly reflected from this interface, while the transmitted wave is sufficiently rapidly decaying in the SDM.

The wave equation for the longitudinal wave propagating in the SDM is as follows [1]:

$$\rho_2 \ddot{u}_x = c_2 u_{x,xx} + b_2 u_{x,xxt}, \quad (1)$$

where u_x is the longitudinal displacement component in the wave, c_2 is the elastic modulus, ρ_2 is the medium density, and b_2 is the dissipative loss parameter. The latter quantity is determined by the shear viscosity η, bulk viscosity ξ, and thermal conductivity χ coefficients according to the formula [1]

$$b_2 = \frac{4}{3}\eta + \xi + \chi(c_v^{-1} + c_p^{-1}), \quad (2)$$

where c_p and c_v are the heat capacities of the medium at constant pressure and volume, respectively.

The coefficient of sound absorption α is a single-valued function of the dissipative loss parameter b_2 and can be expressed as $\alpha = \omega^2 b_2/2\rho_2 s_{l2}^3$, where $\omega = 2\pi f$ is the cyclic frequency of the acoustic wave and s_l is the longitudinal sound velocity. Note that Eq. (1) with $b_2 = 0$ describes the acoustic oscillations in a solid with the corresponding material constants.

The solutions corresponding to the incident, reflected, and transmitted waves can be written in a standard form [2]:

$$\begin{aligned} u^{\mathrm{I}} &= u_{01}^{\mathrm{I}} \exp[i(k_1 x + \omega t)], \\ u^R &= u_{01}^R \exp[i(-k_1 x - \omega t)], \\ u^T &= u_{02}^T \exp[-\alpha x + i(k_2 x - \omega t)], \end{aligned} \quad (3)$$

where $k_1 = \omega/s_{l1}$ and $k_2 = \omega/s_{l2}$ are wavenumbers and t is the time.

The boundary conditions at $x = 0$ establish continuity of the elastic displacements and stresses (for a liquid

SDM, the stresses are replaced by the pressure) across the interface and are written as follows:

$$\begin{aligned} u_x^{\mathrm{I}} + u_x^R &= u_x^T, \\ c_1(u_{x,x}^{\mathrm{I}} + u_{x,x}^R) &= c_2 u_{x,x}^T + b_2 u_{x,xt}^T. \end{aligned} \tag{4}$$

The solutions (3) obey the wave equation (1) and, when substituted into (4), yield a system of linear equations determining the coefficients of reflection $R = u_{01}^R/u_{01}^{\mathrm{I}}$ and transmission $T = u_{02}^T/u_{01}^{\mathrm{I}}$ such that $T = 1 + R$. The reflection coefficient can be as written in the following form:

$$R_\omega = \frac{1-\tilde{\varepsilon}}{1+\tilde{\varepsilon}}, \tag{5}$$

where $\tilde{\varepsilon} = \varepsilon(1 - ix)^{1/2}$; $\varepsilon = z_2/z_1$; $x = \omega/\omega_c$; $z_1 = \rho s_{l1}$ and $z_2 = \rho s_{l2,0}$ are the acoustic impedances of the first and second media (in the absence of dissipation); $\omega_c = \rho_2 s_{l2,0}^2/b$ is an effective frequency characterizing the SDM; and $s_{l2,0}$ is the sound velocity (for $\omega = 0$).

It should be also recalled that $R_0 = (z_2 - z_1)/(z_2 + z_1)$ and $T_0 = 2z_2/(z_2 + z_1)$ represent the so-called amplitude coefficients of reflection and transmission of the acoustic wave (for $\omega \longrightarrow 0$) [3].

Using formula (5), we obtain the following relationship for the reflected signal phase:

$$\tan\Psi_\omega^R = -\frac{2\varepsilon(1+x^2)^{1/4}\sin\frac{\Psi}{2}}{1-\varepsilon^2(1+x^2)^{1/2}\cos\Psi}, \tag{6}$$

where $\Psi = -\arctan x$. Thus, relationships (5) and (6) indicate that reflection of an acoustic wave from SDM is accompanied by a change in both amplitude and phase of the incident wave. When the wave is reflected from a less dense acoustic medium ($z_2 < z_1$) and $\omega \ll \omega_c$, the signal phase is inverted ($\Psi^R = \pi$). In the vicinity of $\omega \sim \omega_c$, the reflection coefficient exhibits a minimum, while the phase shift of the reflected signal relative to the incident wave keeps increasing. For $\omega \gg \omega_c$, we obtain $R_\omega \longrightarrow 1$ and $\Psi^R \longrightarrow 2\pi$, which corresponds to the total reflection of the incident signal. In the opposite case of reflection from a denser medium, the reflected signal exhibits no phase inversion ($\omega \ll \omega_c$, $R_\omega \longrightarrow R_0$, $\Psi^R \longrightarrow 0$). By the same token, the case of $\omega \sim \omega_c$ corresponds to a minimum in the reflection R_ω and a maximum in the phase Ψ_ω^R. Finally, for $\omega \gg \omega_c$, $R_\omega \longrightarrow 1$ and $\Psi^R \longrightarrow 0$.

To complete the description, we also present expressions for the transmission coefficient T_ω and the phase Ψ_ω^T of the transmitted longitudinal acoustic wave:

$$T_\omega = \frac{2}{1+\tilde{\varepsilon}}, \tag{7}$$

$$\tan\Psi_\omega^T = \frac{\varepsilon(1+x^2)^{1/4}\sin\frac{\Psi}{2}}{1+\varepsilon(1+x^2)^{1/4}\cos\frac{\Psi}{2}}. \tag{8}$$

Figure 1 shows the frequency dependences of the amplitude reflection and transmission coefficients and the corresponding phases in the cases of reflections with inversion ($R_0 < 0$, organic glass–epoxy interface) and without inversion ($R_0 > 0$, aluminum–epoxyinterface). It was of interest to determine, besides the amplitude reflection coefficient R_ω, the coefficients of reflection for the waves of velocity $R_{\dot{u}} = \dot{u}^R/\dot{u}^{\mathrm{I}}$, pressure $R_p = p^R/p^{\mathrm{I}}$, and intensity $R_J = J^R/J^{\mathrm{I}}$. Since, according to (3), the differentiation with respect to time does not change conditions (4), $R_{\dot{u}} = R_u$. Taking into account a relationship between the pressure and velocity $p/\dot{u} = \pm z_1$ (where the upper and lower signs refer to the waves propagating along the x axis and in the opposite direction, respectively), we obtain $R_p = -R_u$. Therefore, the frequency dependences of the moduli of the amplitude reflection coefficient and the corresponding phase coincide with the curves for the moduli of the coefficient of reflection and the phase of the pressure wave.

Since the intensity and pressure of the wave in a nondissipative medium are related as $J_{\mathrm{I}} = p_{\mathrm{I}}^2/2z_1$ and $J_R = p_R^2/2z_1$, the reflection coefficient for the sound intensity can be expressed as $R_J = |R_\omega^2|$. Note that, by virtue of the energy conservation law, the transmission coefficient for the sound intensity in the SDM is $T_J = 1 - R_J$ (in contrast to the amplitude coefficient, for which $T = 1 + R$). All of the transmitted sound wave intensity T_J in the SDM is irreversibly converted into heat in the course of the longitudinal acoustic wave propagation in this medium. From the standpoint of practice, registration of the reflected signals is more informative than detection of the attenuated signals transmitted through a layer of the SDM. For this reason, we will mostly dwell on the wave reflection processes below.

A real pulsed acoustic signal can be represented as follows:

$$\begin{aligned} u_1^{\mathrm{I}}(x=0,t) &= u_{01}^{\mathrm{I}}\exp\left(-\Gamma\frac{|t|}{T}\right)\exp\left(i2\pi\frac{t}{T}\right) \\ &\times\left[\theta\left(t-\frac{\tau}{2}\right)-\theta\left(t+\frac{\tau}{2}\right)\right], \end{aligned} \tag{9}$$

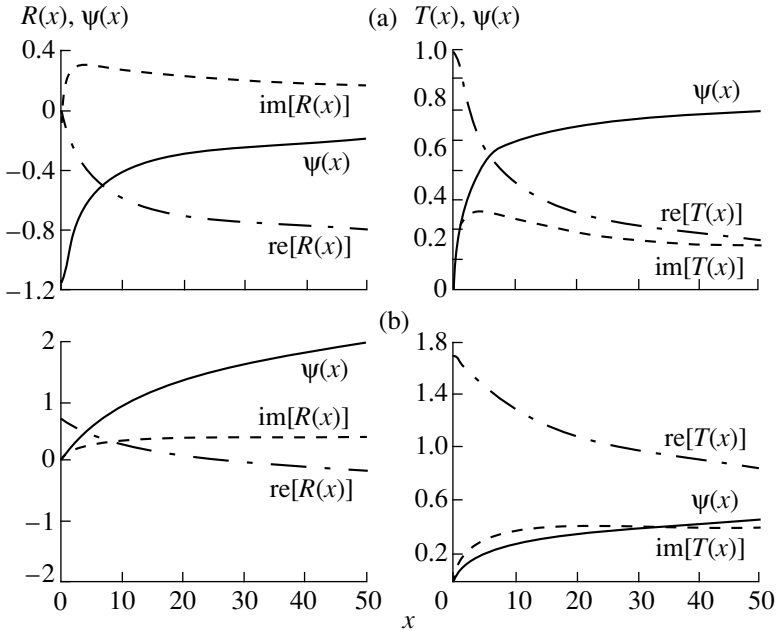

Fig. 1. Frequency dependences of the amplitude reflection and transmission coefficients and the corresponding phases calculated for different interfaces: (a) organic glass– epoxy ($z_1 = 3.1 \times 10^6$ kg/(m^2 s), $z_2 = 3.25 \times 10^6$ kg/(m^2 s), $\omega_c = 2\pi \times 10$ MHz); (b) aluminum–epoxy interface ($z_1 = 17.33 \times 10^6$ kg/(m^2 s)).

where Γ is a dimensionless parameter determining the envelope of the acoustic signal (this parameter is related to the quality factor Q of a piezoceramic ultrasonic transducer by the relationship $\Gamma = \pi/Q$), $T = 2\pi/\omega_0$, ω_0 is the frequency of the fundamental signal harmonic, $\tau = nT$ is the pulse duration, and n is an integer equal to the number of periods in the emitted pulsed signal.

Proceeding from the above relationships for R_ω and applying the direct and inverse Fourier transforms for the pulsed signal (9), we have numerically calculated the shape of a signal reflected from the organic glass–epoxy compound interface. The results of these calculations showed that the amplitude and phase of the reflected signal significantly depend on the fundamental harmonic frequency of the incident pulsed signal.

It was of interest to consider the peak-to-peak amplitude $D(\omega_c)$ and phase shift $\Delta\varphi(\omega_c)$ of the reflected pulse relative to the incident signal, from which we can quantitatively judge on the effective frequency and, hence, on the dissipative loss parameter b_2 determined by formula (2). For most SDMs, in which the contribution to the sound absorption due to the thermal conductivity effects is negligibly small in comparison to the viscosity effects, this circumstance provides a base for a sufficiently accurate determination of the viscosity characteristics. Figure 2 shows the aforementioned frequency dependences calculated for the organic glass–epoxy compound interface. As can be seen from these data, the phase measurements seem to be more promising as compared to the amplitude measurements, the more so if we take into account that the phase differences can be measured with an accuracy of 10^{-2} deg or even better.

Experiment. In order to verify the theoretically predicted dependence of the reflection coefficient on the ultrasound energy dissipation in a reflecting medium, we performed the following experiment. A piezoceramic ultrasonic transducer with a resonance frequency of 3.5 MHz, excited by the signal from a pulse generator, produced an acoustic pulse with a shape close to that considered in the above theory. The signals emitted by the transducer and reflected from a structure of the type described above were detected with the aid of a digital oscillograph measuring the signal amplitude and time characteristics.

Figure 3 shows a plot of the pulse reflection coefficient R measured in the course of curing of an epoxy compound prepared according to the standard from 10 g epoxy and 1.2 g hardener. When mixed in this proportion, the epoxy molecules attract the curing agent to form a solid structure as a result of the chemical reaction. As is known from the theory of phase transitions, a substance at the transition point always exhibits anomalous variation of one or several physical parameters. In our case, the system showed a minimum in the amplitude coefficient of reflection of a pulsed acoustic signal. This point corresponds to a phase transition, whereby all hardener molecules formed chemical bonds with the epoxy molecules, which is followed by

stabilization of the spatial lattice thus formed. If the components are taken in a different ratio, there appears an excess of bonds corresponding to unreacted epoxy or hardener [6]. The phase transformation is a spontaneous process, representing a structural transition of the first order. The reliable realization of this process over the whole volume only requires that the compound components would be thoroughly stirred.

It should be noted that the acoustic impedances of the liquid and solid phases of an epoxy compound cannot be significantly different. In the course of curing, the temperature of the solidifying mixture increased by no more than 10°C above the room temperature; nor did we observe any significant variations in the sample volume. Therefore, these factors can explain neither a 2.5-fold decrease in the reflection coefficient nor a change in the reflected acoustic pulse duration τ from 3 to 2 μs. On the other hand, we must note that the character of the theoretical results is significantly different from the nature of experimental data.

In the above theory, the reflection coefficient was studied as a function of the frequency ω_0 of the fundamental harmonic of the emitted acoustic signal at a constant value of the effective frequency ω_c, that is, at a constant coefficient of ultrasound damping in the dissipative medium. In the experiment, we measured the time variation of the reflection coefficient in the course of solidification of the epoxy compound. Thus, the reflection coefficient was studied as a function of the time-dependent coefficient of ultrasound damping in the dissipative medium, while the fundamental harmonic frequency ω_0 remained constant (the piezoceramic ultrasonic transducer is a resonance device incapable of the frequency tuning). Obviously, the viscosity of the dissipative medium and, hence, the ultrasound damping in this medium reached maximum at the phase transition point (upon the epoxy solidification); these characteristics are quantitatively unknown and can hardly be measured experimentally.

Thus, the theoretical curves of the reflection coefficient R_ω were plotted against $x = \omega/\omega_c$, whereas in experiment this parameter initially increased as the system approached the phase transition point and then gradually decreased. According to the theoretical curves in Fig. 1, an increase in the x value is accompanied by a decrease in both the reflection coefficient R_ω and in the reflected pulse duration τ. Thus, the experimental data qualitatively agree with the theoretical predictions. In order to quantitatively check this correlation, it is necessary to experimentally measure the variation of the ultrasound damping during solidification of the epoxy compound. Once the initial and final acoustic parameters of the epoxy compound in the course of curing are known, we may solve the inverse problem and restore, using the obtained experimental data, the time variation of the dissipative loss parameter during this process.

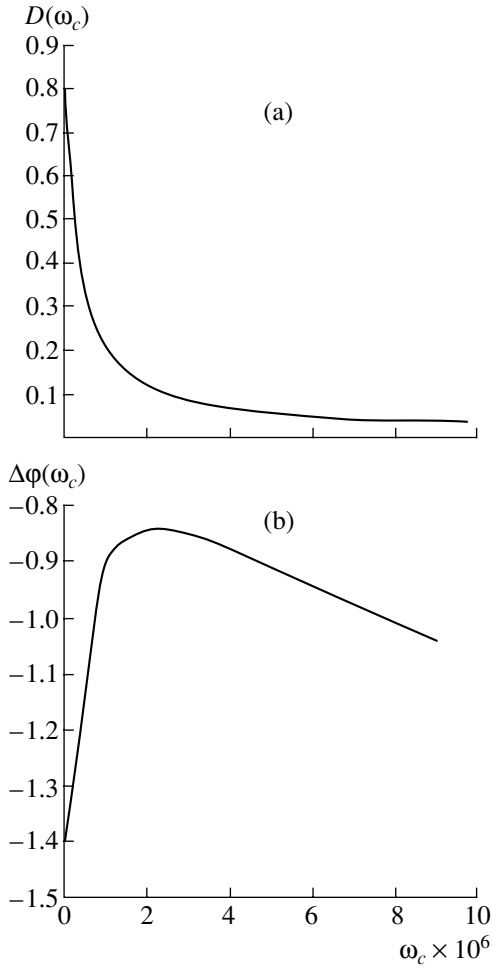

Fig. 2. Frequency dependences (a) of the peak-to-peak amplitude $D(\omega_c)$ and (b) phase shift $\Delta\varphi(\omega_c)$ of the reflected pulse relative to the incident signal.

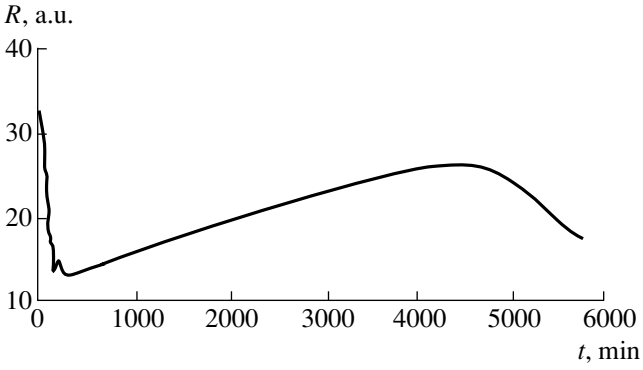

Fig. 3. Experimental time variation of the acoustic pulse reflection coefficient R measured in the course of solidification of an epoxy compound.

Conclusion. We may conclude that the state of a reflecting dissipative medium significantly affects the

reflection coefficient and the reflected signal phase for both continuous and pulsed acoustic signals. Since the phase measurements are characterized by a higher accuracy as compared to the amplitude measurements, the former can be used to judge on the sound absorption in strongly dissipative media and to determine the viscosity of liquids.

In the modern electronics and machine building, an important role belongs to continuous monitoring of the technological process for obtaining optimum working properties of the products. The fabrication of solid state electronic devices almost always involves a change in the fine structure of substances or their components in the course of physicochemical transformations involved in the technological processes such as molecular and laser beam epitaxy; electro- and photolithography; electrochemical, plasma, and vacuum deposition; and soldering. In most cases, these processes are accompanied by a strong local heating and the corresponding changes in the phase, state, or chemical composition of some regions of materials which, under these conditions, appear as strongly dissipative media. Therefore the acoustic measurements offer a means of continuous monitoring and, hence, flexible control of the technological process, ensuring the required product characteristics at a reduced material and energy consumption and increasing working life and performance.

REFERENCES

1. M. B. Vinogradova, O. V. Rudenko, and A. P. Sukhorukov, *Theory of Waves* (Nauka, Moscow, 1990).
2. E. Dieulesaint and D. Royer, *Elastic Waves in Solids* (Wiley, New York, 1981; Nauka, Moscow, 1982).
3. L. F. Lependin, *Acoustics* (Vysshaya Shkola, Moscow, 1978).
4. D. A. Kostyuk and Yu. A. Kuzavko, Vestn. Brestsk. Univ., No. 4, 56 (2000).
5. D. A. Kostiuk and Yu. A. Kuzavko, in *Proceedings of International Conference on Neural Networks and Artificial Intelligence, Brest, 1999*, p. 183.
6. D. A. Kardashov and A. P. Petrova, *Polymeric Glues* (Khimiya, Moscow, 1983).

Translated by P. Pozdeev

Technical Physics Letters, Vol. 27, No. 12, 2001, pp. 999–1002. Translated from Pis'ma v Zhurnal Tekhnicheskoĭ Fiziki, Vol. 27, No. 23, 2001, pp. 41–48.

The Effective Stopping of Relativistic Structural Heavy Ions Colliding with Atoms

V. I. Matveev

Pomorskiĭ State University, Arkhangelsk, Russia

e-mail: matveev.victor@pomorsu.ru

Received June 13, 2001

Abstract—A nonperturbative method is developed for calculating the energy losses upon collisions of relativistic structural large-Z ions with atoms. By structural ions are implied those containing partly occupied electron shells. Usually possessing a large charge, such projectiles (e.g., fully or partly stripped uranium ions) are frequently employed in the experiments on modern heavy-particle accelerators. *© 2001 MAIK "Nauka/Interperiodica".*

As is known, inelastic processes accompanying the collisions of relativistic ions possessing sufficiently large charges with atoms cannot be described [1, 2] within the framework of the perturbation theory even for very large interaction energies. Nonperturbative approaches were developed, for example, in [3–7] (sudden perturbation approximation), [8–10] (eikonal approximation and its modifications), [11] (calculations based on a numerical solution of the time-dependent Dirac equation), and [12, 13] (exact solution of the Dirac equation in an ultrarelativistic limit). A nonperturbative approach based on the Glauber approximation generalized to the case of inelastic collisions of relativistic ions with atoms was recently proposed in [14–16]. A consistent nonperturbative theory describing the energy losses of fully stripped relativistic heavy ions interacting with free electrons was developed in [17].

However, experiments frequently involve partly stripped ions; moreover, such ions may possess an equilibrium charge (smaller than that of a fully stripped ion) established as a result of recharge and electron losses in the course of the ion motion in a medium. In calculations of the ion stopping, the field of a screened ion is usually described as a field of the corresponding point charge. However, it is basically clear that ions behave as fully stripped unscreened charges during collisions described by small impact parameters or large transferred momenta; the same ions behave as screened charges in the interactions involving large impact parameters or small transferred momenta. In other words, it seems expedient [5, 18, 19] to consider the decelerated ion as an extended structural particle with dimensions on the order of the size of electron shells occupied by electrons corresponding to stationary ion charge, rather than as a point charge.

Such effects were considered (see, e.g., [5, 18, 19]) within the framework of the perturbation theory, the applicability of which requires obeying the inequality $Z/v \ll 1$, where Z is the charge of the projectile and v is the relative velocity of colliding particles (here and below, we use the atomic units $\hbar = m_e = e = 1$). For consistently taking into account the electron "coat" of a heavy relativistic ion, a nonperturbative consideration is necessary, the more so that recent experiments (see, e.g., [20–23] and references therein) involved energy losses of ions possessing very large charges for which the region of applicability of the Born approximation is, strictly speaking, not reached [1] even for $v \approx c$ (c is the speed of light), so that $Z/v \sim 1$.

Below, we present a nonperturbative theory describing the energy losses upon collisions between relativistic structural large-Z ions with atoms. Using this approach, a simple formula for the effective ion stopping is obtained.

For simplicity, let us first consider the collision of a relativistic large-Z with hydrogen atom. As was shown in [8], the whole interval $0 < b < \infty$ of possible values of the impact parameter b can be divided into three regions:

$$(A)\ 0 < b < b_1, \quad (B)\ b_1 < b < b_0, \quad (C)\ b_0 < b < \infty, \tag{1}$$

which correspond to small, medium, and large impact parameters. The boundaries of these regions are determined by the quantities

$$b_1 \leq 1, \quad b_0 \approx v\gamma; \quad \gamma = 1/\sqrt{1-\beta^2}, \quad \beta = v/c.$$

Now we will calculate the effective stopping κ [24] in each of the three regions (1) and determine the total effective stopping by adding these contributions. The exact boundary values are insignificant, since κ depends on b_1 and b_0 in each region by a logarithmic law; this provides for a correct matching of the contri-

butions from adjacent regions and makes the final expression independent of the matching parameters b_1 and b_0.

(A) Small impact parameters: $0 < b < b_1$. In the case of small impact parameters or large transferred momenta, we may consider [25] the atomic electrons as free and resting before the scattering event and describe the ion as a fully stripped unscreened charge Z. Under these conditions, we can use the results of Lindhard and Sorensen [17]. According to the results of numerical calculations for $\gamma \sim 10$ and the ion charge $Z \le 92$, the energy losses can be described by a frequently employed formula

$$\kappa(b < b_1) = \frac{4\pi Z^2}{v^2}\left(\ln(b_1\gamma v\eta) - \frac{1}{2}\beta^2 + \Delta L_{\text{Bloch}} + \Delta L_{\text{Mott}}\right), \quad (2)$$

where ΔL_{Bloch} and ΔL_{Mott} are the Bloch correction [26] and the Mott correction [27] (effectively differing from zero [17] only for small values of the impact parameters), and $\eta = 1.781$.

(B) Intermediate region: $b_1 < b < b_0$. Let us restrict the consideration to light (nonrelativistic) atoms. In this case, by analogy with [5, 18, 19], we may ignore the process of electron shell excitation in the projectile and describe the structural ion as an extended charge. Following [5, 18, 19, 28], we will assume that the nucleus of the impinging ion bears a charge Z, while N_i electrons are distributed around this nucleus with the radial density

$$\rho(r) = -\frac{N_i}{4\pi\lambda^3}\frac{\lambda}{r}e^{-r/\lambda}.$$

Here, λ is the screening parameter determined by the formula

$$\lambda = g\frac{\nu^{2/3}}{1-\nu/7}\frac{1}{Z^{1/3}}; \quad g = 0.3(3\pi^2/50)\Gamma(1/3) \approx 0.48,$$

where $\nu = N_i/Z$ is the relative number of electrons in the ion. The Coulomb interaction between an ion occurring at the point $\mathbf{R}$ and an atomic electron located at the point $\mathbf{r}$ is described by the potential

$$U(\mathbf{R}; \mathbf{r}) = -\frac{Z(1-\nu)}{|\mathbf{r}-\mathbf{R}|} - \frac{Z\nu}{|\mathbf{r}-\mathbf{R}|}\exp\left(-\frac{1}{\lambda}|\mathbf{r}-\mathbf{R}|\right),$$

where the ion coordinates are usually expressed through the impact parameter $\mathbf{b}$: $\mathbf{R} = (X, \mathbf{b})$.

In the eikonal approximation, the cross section for the transition of a hydrogen atom from state $|0\rangle$ into state $|n\rangle$ upon collision with a relativistic ion is as follows [8]:

$$\sigma_n = \int d^2b\left|\left\langle n\left|1 - \exp\left\{-\frac{i}{v}\int dX U(\mathbf{R}; \mathbf{r})\right\}\right|0\right\rangle\right|^2. \quad (3)$$

As can readily be checked [3], an atomic electron interacting with the ion in the region $b_1 < b < b_0$ acquires a momentum $\ll c$ and, hence, can be considered as nonrelativistic both before and after collision. For this reason, we can substitute a static Coulomb potential for U in formula (3), which allows the total effective stopping in the region under consideration ($b_1 < b < b_0$) with $b_1/\lambda \ll 1$, $b_0/\lambda \gg 1$ to be presented in the following form:

$$\kappa(b_1 < b < b_0) = 4\pi\frac{Z^2(1-\nu)^2}{v^2}\ln b_0 + 4\pi\frac{Z^2}{v^2}\ln\left[\frac{1}{b_1}\left(\frac{2\lambda}{\eta}\right)^{\nu(2-\nu)}\right], \quad (4)$$

where $\eta = \exp B = 1.781$ ($B = 0.5772$ is the Euler constant).

(C) Large impact parameters: $b_0 < b < \infty$. In this range of impact parameters, interaction of the projectile with an atom can be described within the framework of the perturbation theory. The atom is considered as occurring in the field of a screened ion possessing an effective charge $Z^* = Z(1-\nu)$. The effective stopping is [8]

$$\kappa(b > b_0) = 4\pi\frac{(Z^*)^2}{v^2}\left\{\ln\frac{2v}{\eta I b_0\sqrt{1-\beta^2}} - \frac{\beta^2}{2}\right\}, \quad (5)$$

where I is the "mean" atomic energy introduced as in [25].

Now we can determine the total stopping by adding the contribution from three regions,

$$\kappa = \kappa(b < b_1) + \kappa(b_1 < b < b_0) + \kappa(b > b_0),$$

which yields

$$\kappa = \frac{4\pi Z^2(1-\nu)^2}{v^2}\left(\ln\frac{2v}{\eta I\sqrt{1-\beta^2}} - \frac{\beta^2}{2}\right) + \frac{4\pi Z^2}{v^2}\left(\ln\frac{v\eta}{\sqrt{1-\beta^2}} - \frac{\beta^2}{2} + \ln\left[\left(\frac{2\lambda}{\eta}\right)^{\nu(2-\nu)}\right] + \Delta L_{\text{Bloch}} + \Delta L_{\text{Mott}}\right). \quad (6)$$

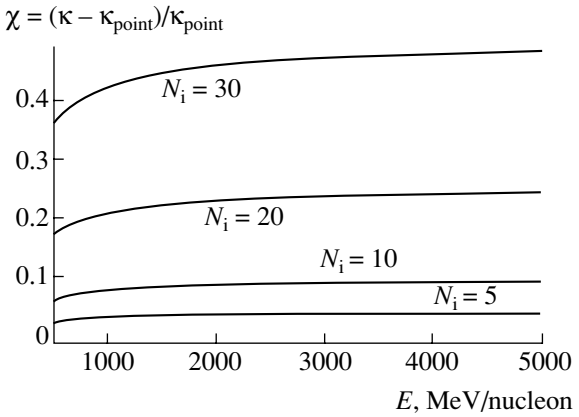

Fig. 1. Plots of the relative correction χ versus energy for incident ions with a charge $Z = 92$ and various numbers of screening electrons $N_i = 5$, 10, 20, and 30.

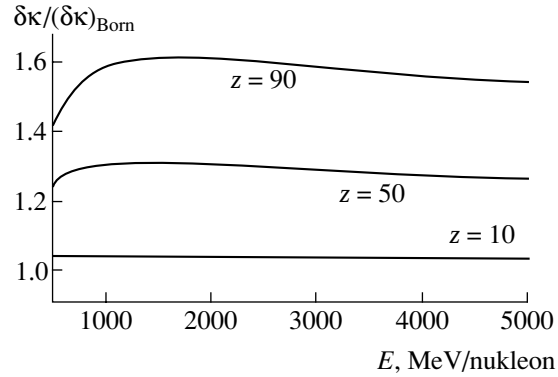

Fig. 2. Plots of the ratio $\delta k/(\delta k)_{Born}$ versus energy for incident ions with various charges $Z = 10$, 50, 90 and the same relative number of screening electrons $\nu = 0.2$.

This formula can be generalized so as to include the collisions of relativistic structural heavy ions with complex atoms by a standard procedure [24]. According to this, the right-hand part is multiplied by the number of atomic electrons N and the atomic characteristic I introduced in (5) is calculated for the complex atom under consideration. For comparison, the effective stopping [29] of a point nucleus with the charge Z^* can be expressed as

$$\kappa_{point} = 4\pi\frac{(Z^*)^2}{v^2} \times\left(\ln\frac{2v^2}{I(1-\beta^2)} - \beta^2 + \Delta L_{Bloch} + \Delta L_{Mott}\right). \quad (7)$$

In order to make a correction for the ion charge extension, we can introduce the difference $\delta\kappa = \kappa - \kappa_{point}$ and determine the relative correction as $\chi = (\kappa - \kappa_{point})/\kappa_{point}$. Behavior of this quantity is illustrated in Fig. 1. The need in using a nonperturbative method for the stopping calculation at large Z^* is illustrated in Fig. 2 by the quantity $\delta\kappa/(\delta\kappa)_{Born}$ representing the ratio of the above correction to the analogous value calculated in the Born approximation, that is, by formulas (6) and (7) with $\Delta L_{Bloch} = \Delta L_{Mott} = 0$.

Conclusions. An allowance for the ion charge extension leads to an increase in the effective ion stopping κ as compared to the value κ_{point} for a point nucleus with the same effective charge Z^*. By the order of magnitude, the ion energy loss can be estimated as $(\kappa - \kappa_{point})/\kappa_{point} \sim \nu$, where $\nu = N_i/Z$ is the relative number of electrons in shells of the ion. For example, the stopping of a uranium ion with 10 electrons in the bound states is about 10% greater as compared to the stopping of a fully stripped point nucleus with the same charge and mass.

Acknowledgments. This study was supported by the Ministry of Education of the Russian Federation and by the Russian Foundation for Basic Research.

REFERENCES

1. J. Eichler and W. E. Meyrhof, *Relativistic Atomic Collisions* (Academic, New York, 1995).
2. J. Eichler, Phys. Rep. **193**, 167 (1990).
3. V. I. Matveev and M. M. Musakhanov, Zh. Éksp. Teor. Fiz. **105**, 280 (1994) [JETP **78**, 149 (1994)].
4. G. L. Yudin, Zh. Éksp. Teor. Fiz. **80**, 1026 (1981) [Sov. Phys. JETP **53**, 523 (1981)].
5. G. L. Yudin, Zh. Tekh. Fiz. **55**, 9 (1985) [Sov. Phys. Tech. Phys. **30**, 4 (1985)].
6. J. Eichler, Phys. Rev. A **15**, 1856 (1977).
7. A. Salop and J. H. Eichler, J. Phys. B **12**, 257 (1979).
8. V. I. Matveev and S. G. Tolmanov, Zh. Éksp. Teor. Fiz. **107**, 1780 (1995).
9. D. S. F. Crothers and S. H. McCann, J. Phys. B **16**, 3229 (1983).
10. J. H. McGuire, Phys. Rev. A **26**, 143 (1982).
11. U. Becker, N. Grun, W. Scheid, and G. Soff, Phys. Rev. Lett. **56**, 2016 (1986).
12. A. J. Baltz, Phys. Rev. Lett. **78**, 1231 (1997).
13. A. J. Baltz, Phys. Rev. A **61**, 042701 (2000).
14. V. I. Matveev and Kh. Yu. Rakhimov, Zh. Éksp. Teor. Fiz. **114**, 1646 (1998) [JETP **87**, 891 (1998)].
15. V. I. Matveev, Kh. Yu. Rakhimov, and D. U. Matrasulov, J. Phys. B **32**, 3849 (1999).
16. V. I. Matveev and D. U. Matrasulov, J. Phys. B **33**, 2721 (2000).
17. J. Lindhard and A. Sorensen, Phys. Rev. A **53**, 2443 (1996).
18. G. Maynard, D. Gardes, M. Chabot, *et al.*, Nucl. Instrum. Methods Phys. Res. B **146** (1), 88 (1998).

19. G. Maynard, M. Chabot, and D. Gardes, Nucl. Instrum. Methods Phys. Res. B **164**/**165**, 139 (2000).
20. E. E. Zhurkin and S. D. Bogdanov, Nucl. Instrum. Methods Phys. Res. B **164**/**165**, 230 (2000).
21. H. Weick, H. Geissel, and C. Scheidenberger, Nucl. Instrum. Methods Phys. Res. B **164**/**165**, 168 (2000).
22. C. Scheidenberger and H. Geissel, Nucl. Instrum. Methods Phys. Res. B **135**, 25 (1998).
23. C. Scheidenberger, H. Geissel, H. H. Mikelsen, *et al.*, Phys. Rev. Lett. **77**, 3987 (1996).
24. L. D. Landau and E. M. Lifshitz, *Course of Theoretical Physics*, Vol. 3: *Quantum Mechanics: Non-Relativistic Theory* (Nauka, Moscow, 1989, 4th ed.; Pergamon, New York, 1977, 3rd ed.).
25. V. B. Berestetskii, E. M. Lifshitz, and L. P. Pitaevskii, *Quantum Electrodynamics* (Nauka, Moscow, 1989; Pergamon, Oxford, 1982).
26. F. Bloch, Ann. Phys. (Leipzig) **16**, 285 (1933).
27. N. F. Mott, Proc. R. Soc. London, Ser. A **124**, 425 (1929).
28. W. Brandt and M. Kitagawa, Phys. Rev. B **25**, 5631 (1982).
29. S. P. Ahlen, Rev. Mod. Phys. **52**, 121 (1980).

Translated by P. Pozdeev